Automated Segmentation and Analysis of High-Speed Video Phase-Detection Data for Boiling Heat Transfer Characterization Using U-Net Convolutional Neural Networks and Uncertainty Quantification

By

Chika Maduabuchi

Bachelor of Engineering
University of Nigeria Nsukka, 2020

Submitted to the Department of Nuclear Science and Engineering
in partial fulfillment of the requirements for the degree of

MASTER OF SCIENCE IN
NUCLEAR SCIENCE AND ENGINEERING

at the

MASSACHUSETTS INSTITUTE OF TECHNOLOGY

May 2024

Authored By:	Chika Maduabuchi Department of Nuclear Science and Engineering May 15, 2024
Certified by:	Matteo Bucci Department of Nuclear Science and Engineering Associate Professor, Thesis Supervisor
Accepted by:	Ju Li Department of Nuclear Science and Engineering Chair, Department Committee on Graduate Students

Automated Segmentation and Analysis of High-Speed Video Data for Boiling Heat Transfer Characterization Using U-Net Convolutional Neural Networks and Uncertainty Quantification

by

Chika Maduabuchi

Submitted to the Department of Nuclear Science and Engineering
on May 15, 2024, in partial fulfillment of the requirements for the degree of
Master of Science in Nuclear Science and Engineering

Abstract

Boiling heat transfer is a complex phenomenon used for cooling and heat management purposes in various industrial applications, such as nuclear reactors. Accurate characterization and understanding of boiling dynamics are essential for the design and optimization of heat transfer systems. High-speed video (HSV) imaging is a powerful tool for capturing the intricate details of boiling processes. However, the manual analysis of HSV data is time-consuming and prone to subjective interpretation. This thesis presents a novel approach for the automated segmentation and analysis of HSV phase-detection images using U-Net Convolutional Neural Networks (CNNs) and uncertainty quantification techniques. The proposed methodology involves the development of specialized U-Net CNN models for segmenting HSV data of boiling phenomena in different fluids, including liquid nitrogen, argon, FC-72, and high-pressure water, under various experimental conditions. The performance of the U-Net models is evaluated and compared with traditional adaptive thresholding techniques. The results demonstrate the superior accuracy and robustness of the U-Net models in identifying and delineating bubbles compared to manual segmentation, particularly in scenarios involving smaller bubbles and complex bubble topologies. To assess the reliability of the calculated boiling metrics, such as contact line density and dry area fraction, a comprehensive uncertainty quantification analysis is also conducted. The impact of discretization errors arising from the pixelation of bubbles is investigated using weighted average percentage relative errors and mean errors under both erosion and dilation conditions. The analysis reveals higher relative uncertainty in contact line density measurements than dry area fraction measurements across all fluids studied. The limitations of the U-Net models in generalizing to other HSV datasets are addressed, emphasizing the need for developing more sophisticated image segmentation models, such as foundation models, that are less sensitive to domain shifts. This is crucial for enabling autonomous experimentation and reducing the reliance on specialized models for each fluid and operating condition. Future research directions are outlined, including the investigation of advanced uncertainty quantification techniques, the development of real-time segmentation and analysis algorithms, the evaluation of uncertainty propagation in heat flux reconstruction, and the extension of the methodology to other multiphase flow phenomena. By

addressing these recommendations, the understanding, characterization, and modeling of boiling phenomena can be further enhanced, contributing to the advancement of boiling heat transfer research and the development of improved heat transfer models and correlations. Overall, this thesis presents a comprehensive approach for the automated segmentation and analysis of HSV phase-detection images using U-Net CNNs and uncertainty quantification techniques. The proposed methodology demonstrates significant potential for accurate and reliable characterization of boiling dynamics, paving the way for advanced boiling heat transfer research and the optimization of heat transfer systems in various industrial applications.

Thesis Supervisor: Matteo Bucci
Title: Associate Professor

Acknowledgments

First and foremost, I would like to express my deepest gratitude to my advisor, Prof. Matteo Bucci, for his unwavering support, guidance, and mentorship throughout my research journey. His invaluable insights, constructive feedback, and constant encouragement have been instrumental in shaping this thesis and my growth as a researcher. I am truly grateful for the opportunity to have worked under his supervision.

I also extend my sincere thanks to my thesis reader, Prof. Ericmoore Jossou, for his time, expertise, and valuable inputs. His thorough review and insightful comments have greatly contributed to improving the quality and clarity of this thesis.

I am incredibly thankful to my beloved wife, Marilyn, for her unconditional love, endless patience, and unwavering support throughout this challenging journey. Her constant encouragement, understanding, and belief in me have been my source of strength and motivation. I could not have accomplished this feat without her by my side.

I acknowledge the support and assistance provided by my colleagues and the staff at the Red Lab and MIT NSE. Their friendly discussions, technical help, and administrative support have made my research experience smooth and enjoyable.

I gratefully acknowledge the financial support provided by the MathWorks Fellowship, which has been crucial in enabling me to pursue my research and complete this thesis.

Lastly, I would like to thank my family and friends for their love, support, and understanding throughout my academic journey. Their constant encouragement and faith in me have been a driving force behind my success.

Table of Contents

List of Figures

List of Tables

Chapter 1

Introduction

Boiling heat transfer is a complex process integral to numerous engineering and industrial application, where it is used for cooling and heat management purposes. The efficiency of this process is often predicted using mechanistic models that partition total heat flux into discrete contributions. These contributions are mechanistically quantified through analytical descriptions of the heat transfer mechanisms involved in the boiling process, such as evaporation, quenching, and single-phase convection [1]. These partitioning terms are calculated based on fundamental boiling parameters, e.g., nucleation site density, bubble departure diameter and frequency, grow time and wait time, dry area fraction, and contact line density. Thus, the development and validation of these models rely on high resolution data obtained using advanced diagnostics and high-speed video imaging, e.g., infrared thermometry [2–4] and phase detection [5,6]. However, while these diagnostics allow imaging the boiling process with high temporal and spatial resolution, the processing of these images to obtain tractable data of the boiling parameters of interest can be very challenging and tedious. To alleviate this issue, in this thesis, we develop ad-hoc machine-learning tools to swiftly segment and analyze phase-detection images of boiling obtained with different fluids and operating conditions, with a focus on dry area fraction and contact line density.

1.1 Motivation

Measuring boiling parameters such as dry area fraction, bubble footprint size distribution, contact line density, and contact line size distributions on boiling surfaces is key to enhancing understanding, modeling and optimization of boiling heat transfer processes. Such measurements can be done using phase detection, which allows identifying which parts of a boiling surface are covered by vapor, liquid, or liquid microlayers [5]. However, existing

methodologies for processing phase detection images, primarily manual or semi-automated, need to be improved to deal with the large amount of data that can obtained from boiling experiments using phase detection. These methodologies are time-consuming and may be user dependent. Such inefficiencies underscore the urgent need for automated, high-throughput post-processing tools to handle this critical task.

1.2 Problem Statement

Machine learning offers a possible solution to overcoming these challenges, especially given its success in segmenting two-phase flow images [7,8]. However, phase detection images of boiling heat transfer pose unique challenges. Unlike back-lit or front-lit shadowgraphy images used in two-phase flows, phase detection images detail the bubble footprints on boiling surfaces, which may feature more complex shapes compared to two-phase flows. Figure 1.1 and Figure 1.2 show samples of two-phase flow shadowgraphy images and phase-detection images of the samples used in this study, respectively. In the phase-detection images, the grayscale can be used to distinguish between the liquid and vapor phases. Here, dark gray indicates liquid in contact with the surface, while light gray indicates vapor. Accurately detecting and measuring the footprint area and contact line of the vapor phase on the boiling surface remains a significant challenge.

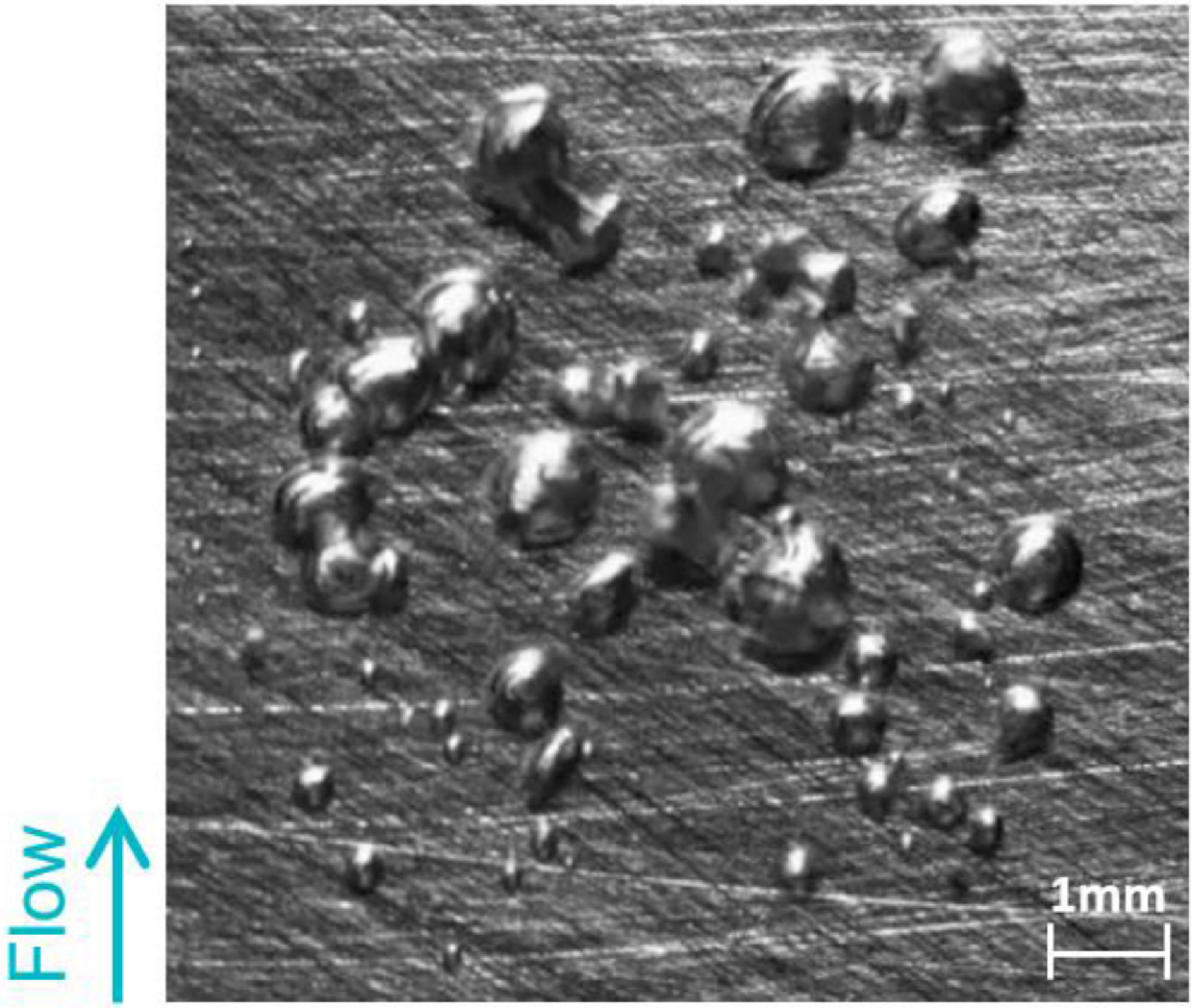

Figure 1.1 Sample of Front-Lit Shadowgraphy images from two-phase flow.

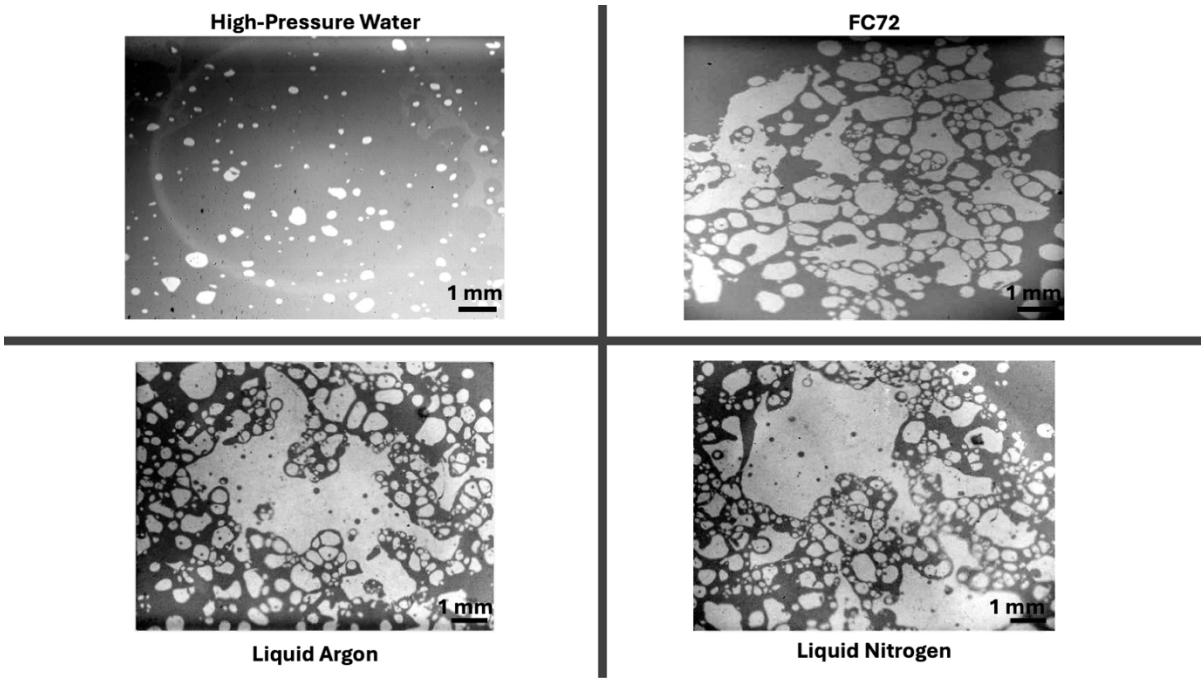

Figure 1.2 Sample Phase-Detection Images Used in this Study.

1.3 Contributions

This thesis contributes to enhancing the processing and analysis of phase detection images of the boiling process through several key innovations:

- The development of advanced U-Net Convolutional Neural Network (CNN) models capable of precisely segmenting phase detection images of various boiling fluids, including liquid nitrogen, liquid argon, FC-72, and high-pressure water.
- The creation of an open-source repository with tools for segmenting bubbles in phase-detection images that facilitates wider access and application of this technology.
- A comprehensive quantification of uncertainties associated with the segmentation process and the impact of image resolution on measurement.

1.4 Objectives

The primary objectives of this research are twofold:

1. To develop processing tools that enable autonomous experimentation, significantly reducing the manual efforts required and improving the reliability of the measurements.
2. To measure, with quantified uncertainties, critical parameters such as dry area fraction, bubble footprint size distribution, contact line density, and contact line size distributions.

1.5 Path to Accomplishment

The path to achieve these objectives involves the following steps:

1. **Understanding the State-of-the-Art**: A thorough survey of existing image segmentation tools, focusing on two-phase flow analysis. This includes evaluating the advantages and limitations of these tools, with a particular emphasis on various CNN architectures and their adaptation to two-phase flow segmentation.
2. **Methodology**: Detailed description of the steps involved in developing the U-Net CNN, including transfer learning and validation using established machine learning metrics and baseline comparisons with adaptive thresholding and manual annotation inspired by domain expertise.
3. **Case Studies**: Presentation of examples where the developed models have been applied to process images in various fluids, including liquid nitrogen, liquid argon, FC-72, and high-pressure water. This step will also cover the analysis of trends related to dry area fraction, contact line density, bubble footprint area distributions, and contact line distribution as functions of the operating heat flux.
4. **Quantification of Uncertainties**: An in-depth examination of the uncertainties involved in image segmentation and the resolution capabilities of the optical setup. This includes revisiting the results from the case studies with a focus on these uncertainties.

This chapter sets the stage for the comprehensive exploration of CNN model development for phase detection image segmentation in boiling surfaces, outlining the

motivation, objectives, and structured approach to achieving these goals. Subsequent chapters will delve deeper into this research's technical development, application, and implications.

Chapter 2

Methodology

This section systematically reviews the evolution of image segmentation techniques as applied to two-phase flow analysis, critically examining the historical progression from conventional image processing tools to the advent of sophisticated deep learning methods. It underscores the limitations of traditional algorithms when faced with complex flow patterns and varying fluid properties under different operating conditions. By comparing the effectiveness of these earlier tools, we illustrate the necessity for the high fidelity and adaptability that deep learning offers. Further, we delineate the role of transfer learning in refining the accuracy of convolutional neural networks to segment intricate two-phase flow structures, emphasizing the improved precision in identifying phase boundaries and characterizing flow features. This chapter culminates in a justification for the selected deep learning architecture tailored to the unique challenges of the specific fluids and thermal conditions pertinent to our investigation.

2.1 Image Processing Tools

Before incorporating deep learning methodologies, various image processing algorithms were utilized to track the phases in two-phase flow analysis [1,9–13]. As early as 2008, researchers, including Wenyin et al. [9], used enhanced Canny edge detection techniques for improved segmentation of gas-liquid interfaces in high-speed video (HSV) footage. Their method capitalized on a more comprehensive grasp of grayscale variations, incorporating Gaussian smoothing to refine edges and mitigate noise. Subsequent stages involving gradient non-maximum suppression and dual thresholding facilitated the extraction of distinct bubble contours, significantly advancing the analysis and classification of complex multi-phase flow patterns. Despite the ability of the processing tool to analyze and identify various flow regimes, there were challenges associated with overlapping bubble images, paving the way for further algorithmic enhancements to augment segmentation accuracy in complex scenarios.

Building upon earlier work, Paz et al., [10] contributed further with machine vision algorithms tailored for recognizing bubbles in subcooled boiling phenomena. Their algorithm, encapsulating both side and front views, as seen in Figure 2.3, enhances adaptability across diverse boiling scenarios. They streamlined the process through dynamic thresholding and edge detection, culminating in bubble outline and trajectory analyses. Yet, challenges persist, notably in setup calibration and algorithm parameterization, underscoring the need for precise adjustments to optimize the application of these algorithms in different experimental frameworks.

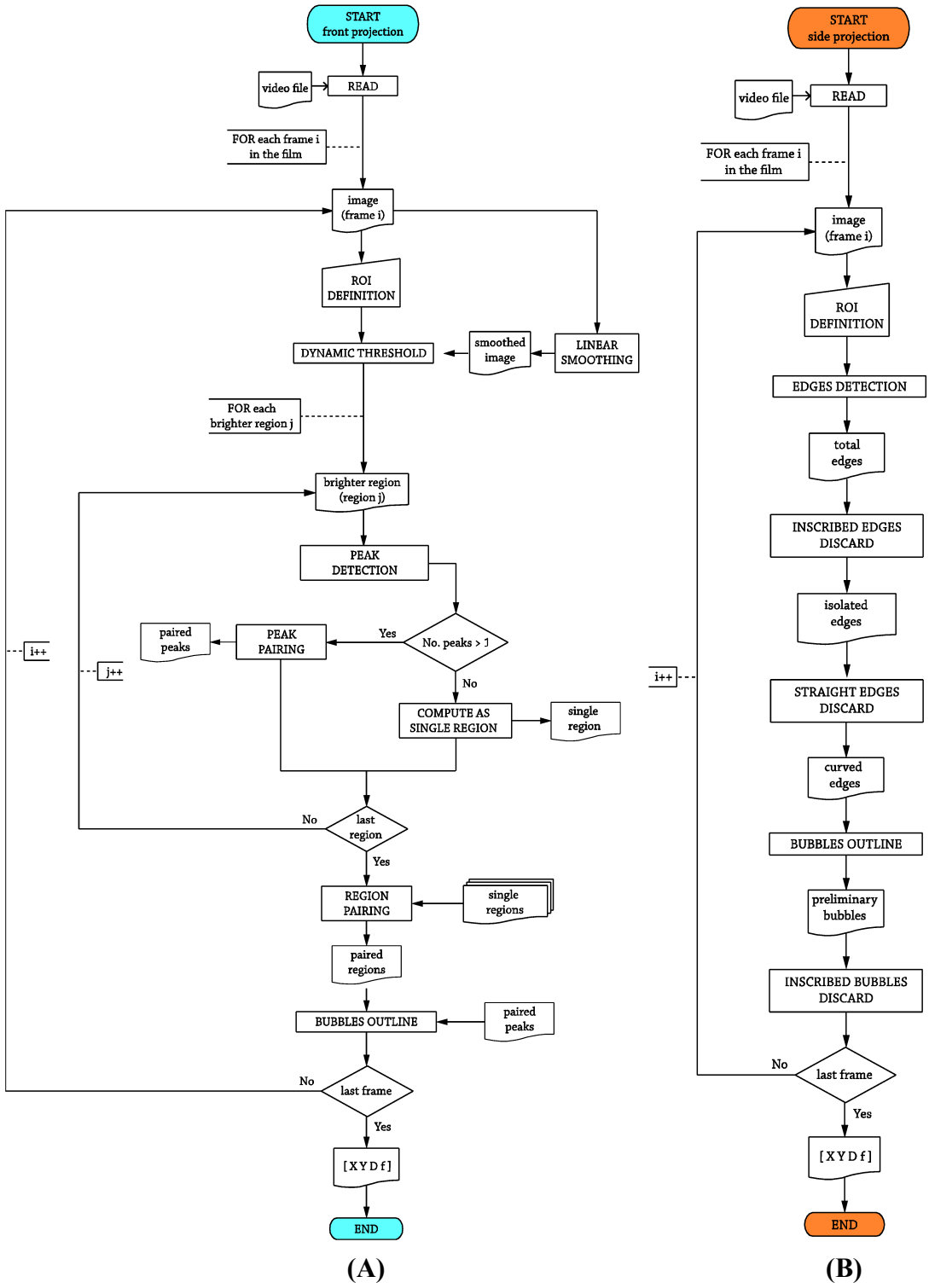

Figure 2.3 Flowchart of the two image processing algorithms (A) Front Projection (B) Side Projection [10].

Zhou and Niu [12] advanced bubble detection in two-phase flows with a multi-frame image processing algorithm. Their approach, leveraging binarization and predictor-corrector methods, adeptly handles overlapping bubble images, enhancing bubble size and velocity measurement accuracy. A flow map of the image processing algorithm is presented in Figure 2.4. Particularly effective in densely bubbled plumes, their method significantly improves recognition rates, showcasing its utility in experimental settings with high overlap rates. Despite its benefits in statistical analysis of bubble dynamics, limitations exist, especially in scenarios where there are overlapping bubbles, the algorithm fails to successfully distinct such bubbles but rather consider them as one as shown in Figure 2.2, underscoring the need for further refinement in diverse flow conditions.

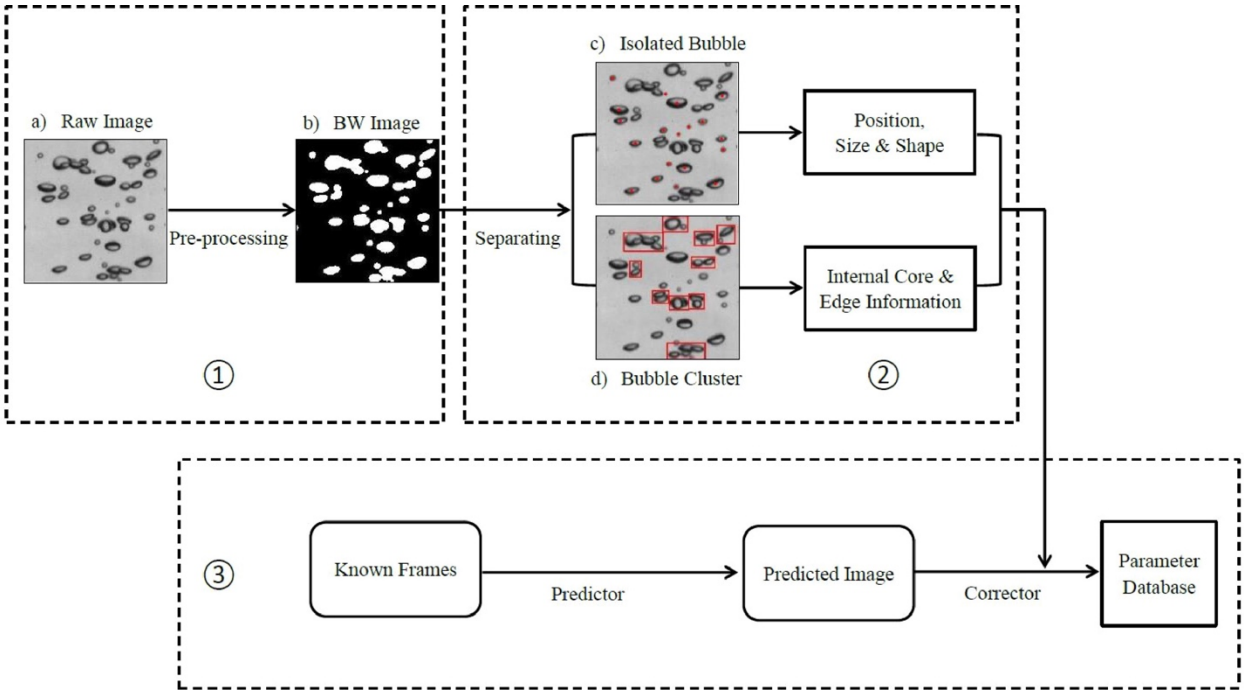

Figure 2.4 Predictor-Corrector Image Processing Algorithm Flow map [12].

Finally, Richenderfer et al., [1] developed an experimental methodology to measure key subcooled flow boiling parameters, including nucleation site density and bubble dynamics parameters, up to the critical heat flux (CHF) limit. Utilizing high-speed video and IR diagnostics alongside in-house image post-processing techniques comprising gray threshold filter and watershed segmentation, they provided detailed insights into wall heat flux

partitioning crucial for validating mechanistic boiling heat transfer and CHF models. The flowchart describing the image processing algorithm in detail is depicted in Figure 2.5. Their findings, particularly on microlayer evaporation's contribution to total heat flux, offer valuable data for developing and validating advanced mechanistic models for two-phase heat transfer systems. The authors noted that in high heat flux conditions, conventional thresholding filters would not give optimal bubble segmentation results.

This short review underscores the inherent challenges in employing standard image-processing approaches, such as adaptive thresholding, for analyzing bubble dynamics under diverse phase-flow conditions and heat fluxes. Despite concerted efforts to leverage HSV imaging for in-depth studies of bubble behavior, the absence of a universally applicable, quantitative analysis framework for different surface materials and variable lighting conditions is apparent. This gap has prompted the exploration of deep learning models as a potential solution to these complex, variable-dependent challenges in boiling research.

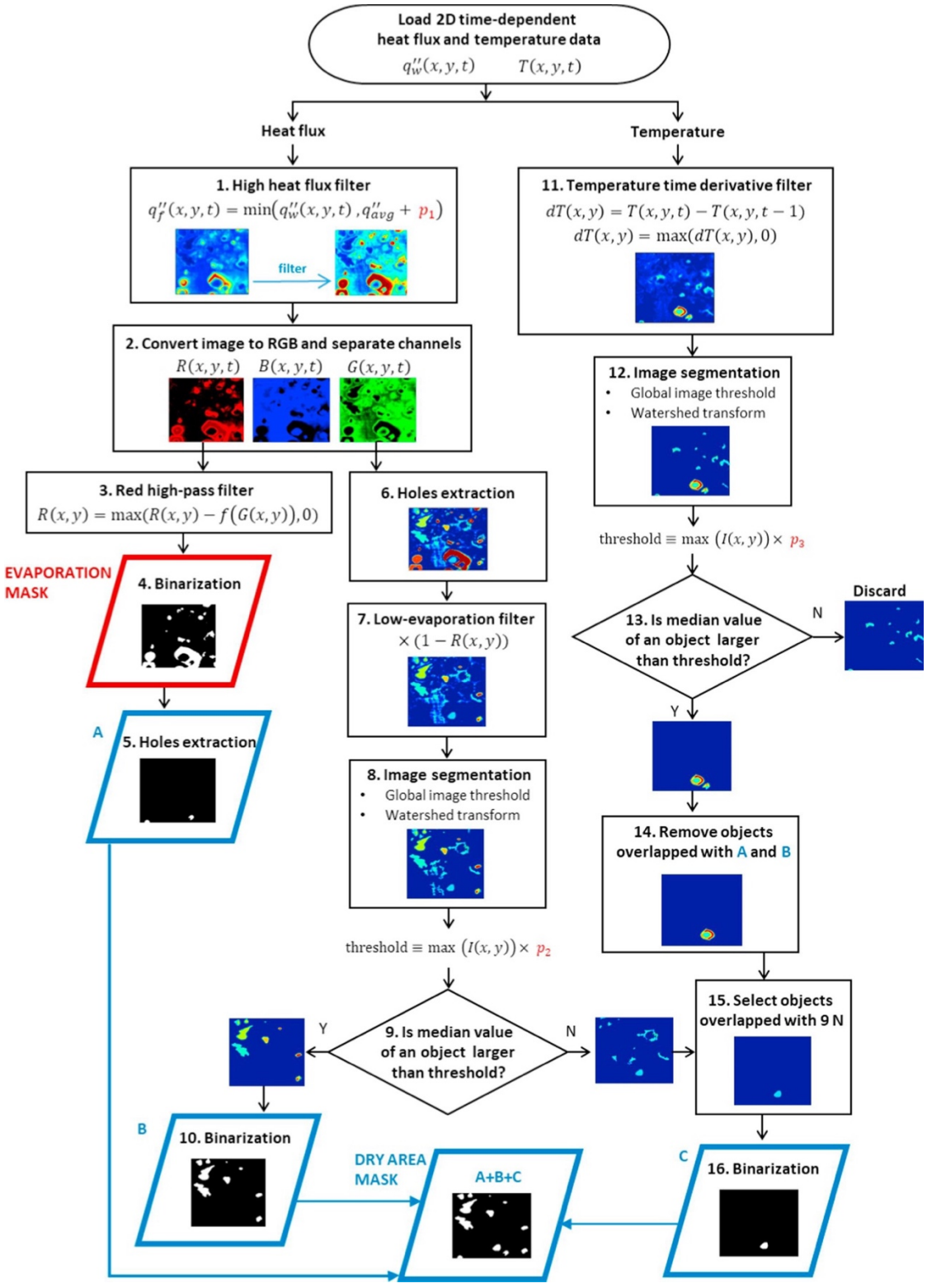

Figure 2.5 Flowchart of the algorithm detecting dry area regions and evaporation in HSV images [1].

2.2 Deep Learning Methods

Recent research has increasingly turned towards deep learning architectures to address the limitations inherent in traditional image-processing techniques for analyzing two-phase flow HSV images. This shift reflects a broader recognition of the need for more adaptable, sophisticated analytical methods to handle the complexities of flow visualization and dynamics across various conditions.

In two-phase flow research, efforts to detect objects like bubbles, droplets, and particles have integrated deep learning models with traditional image processing tools. Studies have combined object detection frameworks and convolutional neural networks (CNNs) to approximate the shapes and positions of objects in two-phase flows [14–16]. However, accurately capturing the precise shape of the gas-liquid interface remains a challenge due to the limitations of these models in handling the varied geometry of bubbles under different flow conditions. This motivated several studies to look for a universal model that automatically recognizes and extracts the shapes of the bubbles based on learned information from the frames [7,8,17–22]. This inspired Kim and Park [17] to develop a comprehensive Mask R-CNN model (ResNet 101 as the backbone and transfer learning from COCO weights) [23] that can automatically detect and extract detailed interface shapes (instance segmentation), addressing gaps in previous research by focusing on a broader range of bubble geometries and validating the model against new, unseen bubbly flow data. It was concluded that the average precision of the model was 0.981, while mask extraction time was reduced compared to regular image processing algorithms.

Soibam et al. [7] developed a bubble detection and segmentation deep learning model (YOLOv7) for tracking bubble dynamics within a heated vertical rectangular mini-channel in subcooled conditions, utilizing high-speed camera images as input. Faced with challenges such as noise and variable conditions in the raw images, the model employed transfer learning for efficient training on a limited dataset. Demonstrating 98% accuracy in bubble detection and robustness against various experimental setups, the model achieved a remarkable intersection over union (IoU) score of 88%, higher than that of traditional image processing algorithms

(71%), as seen in Figure 2.6. It successfully captures detailed bubble behaviors—coalescence, oscillation, collisions—enabling precise analysis of their spatial-temporal dynamics.

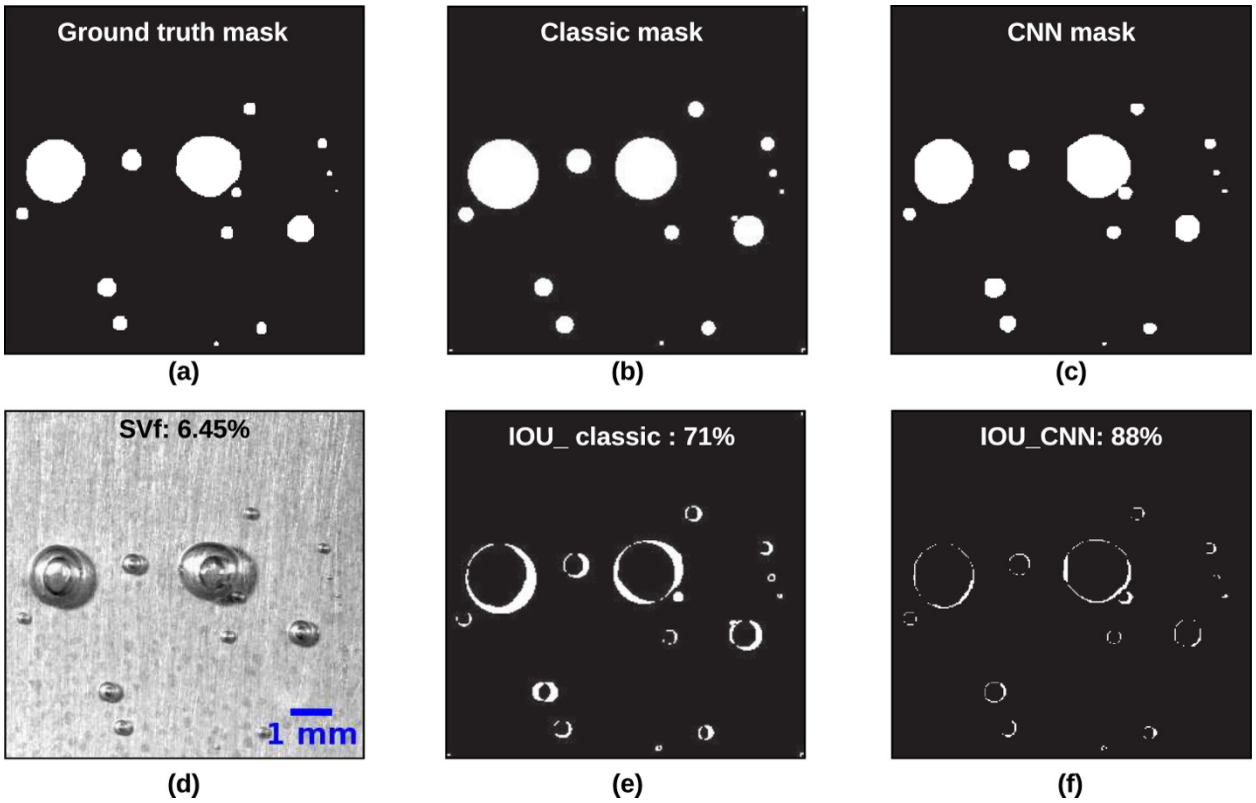

Figure 2.6 Mask Comparisons between Classical Image Processing Algorithms and CNNs (YOLOv7 model). SVF: Surface Void Fraction of Normal Image [7]

Seong et al., [18] introduced a data-driven methodology for analyzing bubble dynamics in subcooled flow conditions. They employed a U-Net-based CNN with transfer learning from biological cell images [24] for efficient bubble segmentation in HSV images. The U-Net CNN encoder-decoder architecture is depicted in Figure 2.7. Validated against 100 ground-truth images, the model demonstrates over 90% accuracy and precision. Additionally, the study proposes a novel criterion for identifying condensing bubbles through bubble displacement divergence, enabling the quantification of key boiling parameters. This approach, validated

against IR thermometry, offers a promising avenue for advancing the understanding of two-phase flow boiling heat transfer mechanisms.

Similarly, Ravichandran et al., [19] utilized 3D deep U-Net-based CNNs and high-resolution IR thermometry to identify and track dry patches on boiling surfaces. They achieved over 90% accuracy in mapping dry areas against ground-truth data up to 2 bars pressure, enabling automated detection for enhanced boiling heat transfer. The architecture of the 3D U-Net CNNs is portrayed in Figure 2.8. They leveraged transfer learning from models initially trained on biological cell images to enhance their segmentation process. They also compared the segmentation output of the U-Net CNN to that of other traditional architectures and found the predicted masks similar.

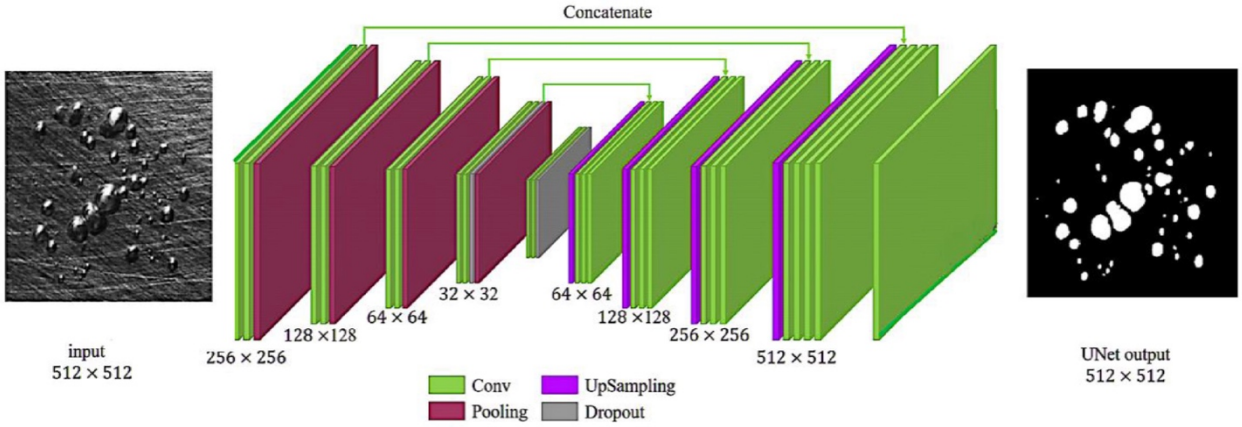

Figure 2.7 U-Net CNN with Encoder-Decoder Architecture [18]

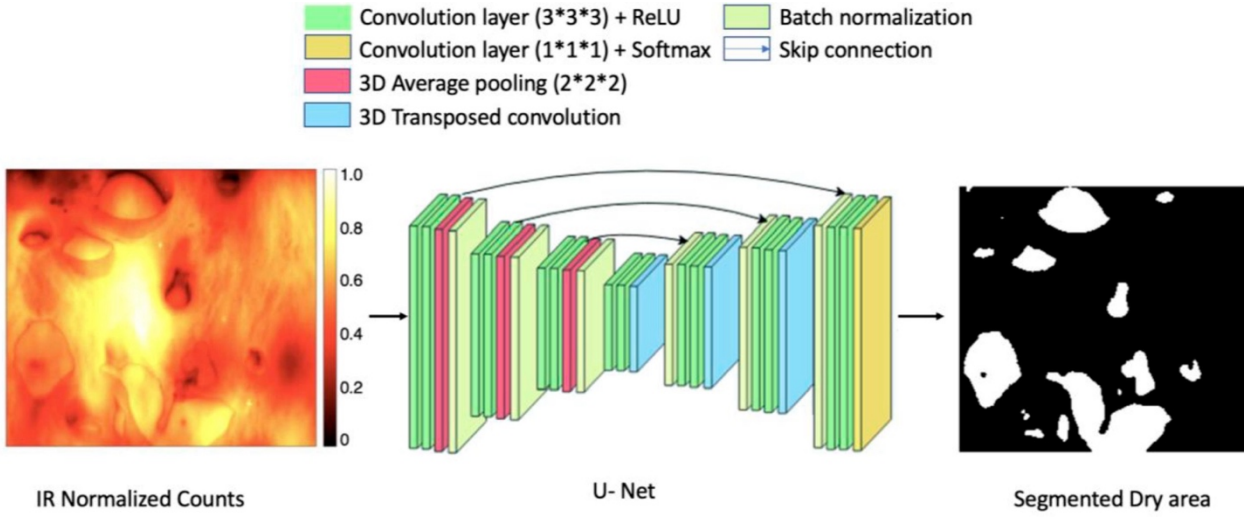

Figure 2.8 3D U-Net CNN used by Ref. [19] for segmenting dry patches from IR counts.

In exploring bubble nucleation within two-phase flows, Suh et al., [20] recently introduced Vision-Inspired Online Nuclei Tracking System (VISION-iT), an integrated framework designed for the automated extraction of multiple physical parameters associated with nucleation events from pool-boiling high-speed video (HSV) data. This innovative system encompasses image capture stages, instance segmentation via a specially developed Mask R-CNN model, and sophisticated post-processing techniques. Figure 2.9 depicts the utilization of the VISION-iT in analyzing phase-change heat transfer dynamics. Despite its promising capabilities, VISION-iT encounters a significant challenge in versatility; adapting it to alternative experimental setups necessitates extensive fine-tuning to accommodate new datasets effectively. This requirement for customization underscores a critical consideration for broader application across diverse research contexts.

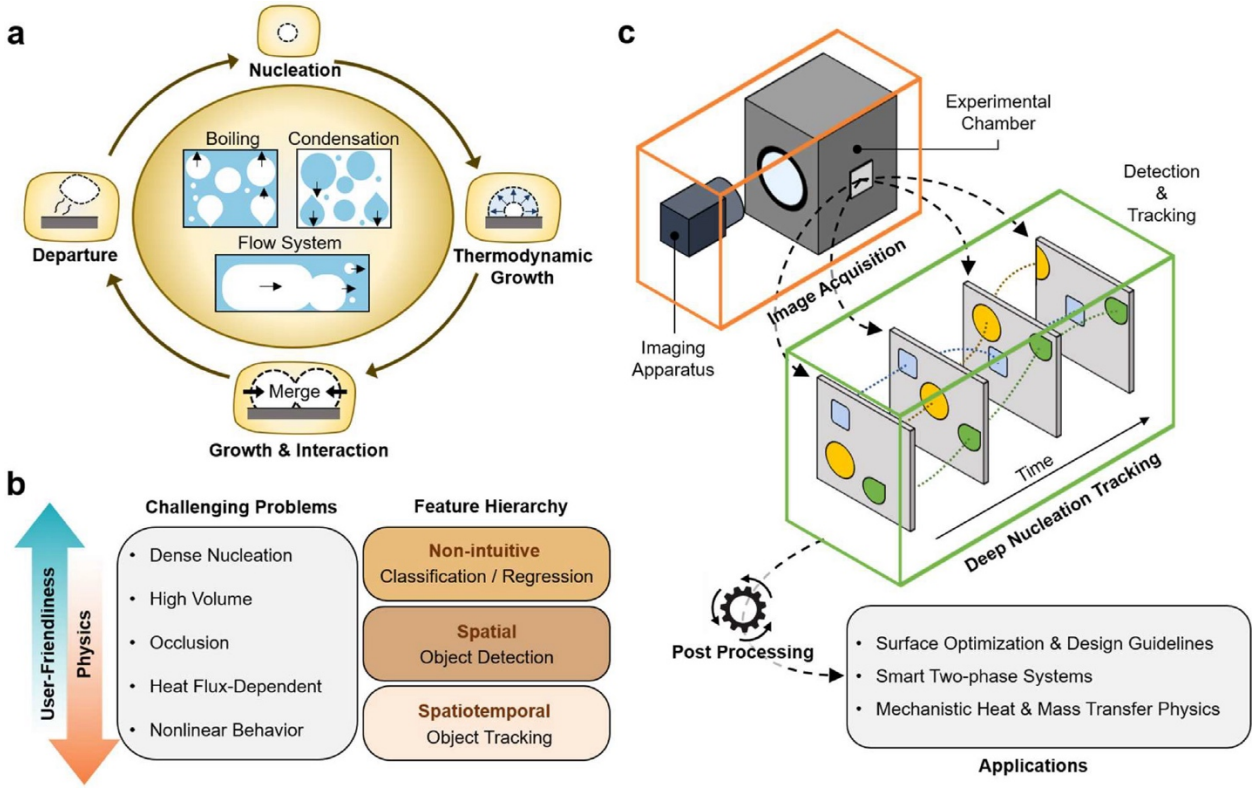

Figure 2.9 The Role of VISION-iT in Phase-Change Heat Transfer Analysis [20]: (a) The intricate cycle of nucleation, growth, interaction, and departure in phase-change processes, featuring intense nucleation activity with potentially hundreds of instances each second. (b) The landscape of AI-driven approaches for tackling the complexities of two-phase image analysis varies across a spectrum of feature complexities. Advanced spatio-temporal analysis

tools, positioned at the upper echelons of this spectrum, often present a challenge in user accessibility due to their multi-modular architecture. (c) Through VISION-iT, imagery data captured (highlighted by the orange frame) undergoes a series of sophisticated processes including object detection, tracking, and analysis (denoted by the green frame), culminating in the extraction of detailed physical parameters that provide a comprehensive insight into the mechanisms of two-phase heat and mass transfer.

Malakhov et al., [8] even compared the bubble detection and segmentation capabilities of the Mask R-CNN and U-Net CNN models on high-speed visualizations from the bottom side of a transparent heater while boiling water at diverse sub-atmospheric pressures. Their findings indicated that although the accuracy of bubble segmentation using the U-Net CNN was higher, the Mask R-CNN model provided better results, especially in high heat-flux scenarios where the bubbles tend to overlap and merge. A comparison between the segmentation provided by Mask R-CNN and U-Net CNN is provided in Figure 2.10. Despite the remarkable findings of this study, transfer learning was not used; instead, the models were trained from scratch, which might explain the reason for the lower accuracy provided by the U-Net compared to the actual results. If pre-trained information from similar domains was applied in the U-Net training to make it more efficient, better results would have been obtained in less training time.

Similarly, Chen et al. [21] implemented a customized approach by developing BIMSNet, a modified U-Net Convolutional Neural Network (CNN) architecture specifically designed for the semantic segmentation of bubbles in experimental shadowgraph images under diverse flow and lighting conditions. The architecture of BIMSNet closely mirrors that of the original U-Net, as illustrated in Figure 2.11. Upon training, BIMSNet achieved remarkable dice coefficients of 99.3% and 99.73% on the validation and test datasets, respectively. This performance surpasses conventional adaptive thresholding techniques, obviating the need for empirical determination of thresholding limits for image binarization in post-processing, thus demonstrating superior bubble detection and segmentation capabilities.

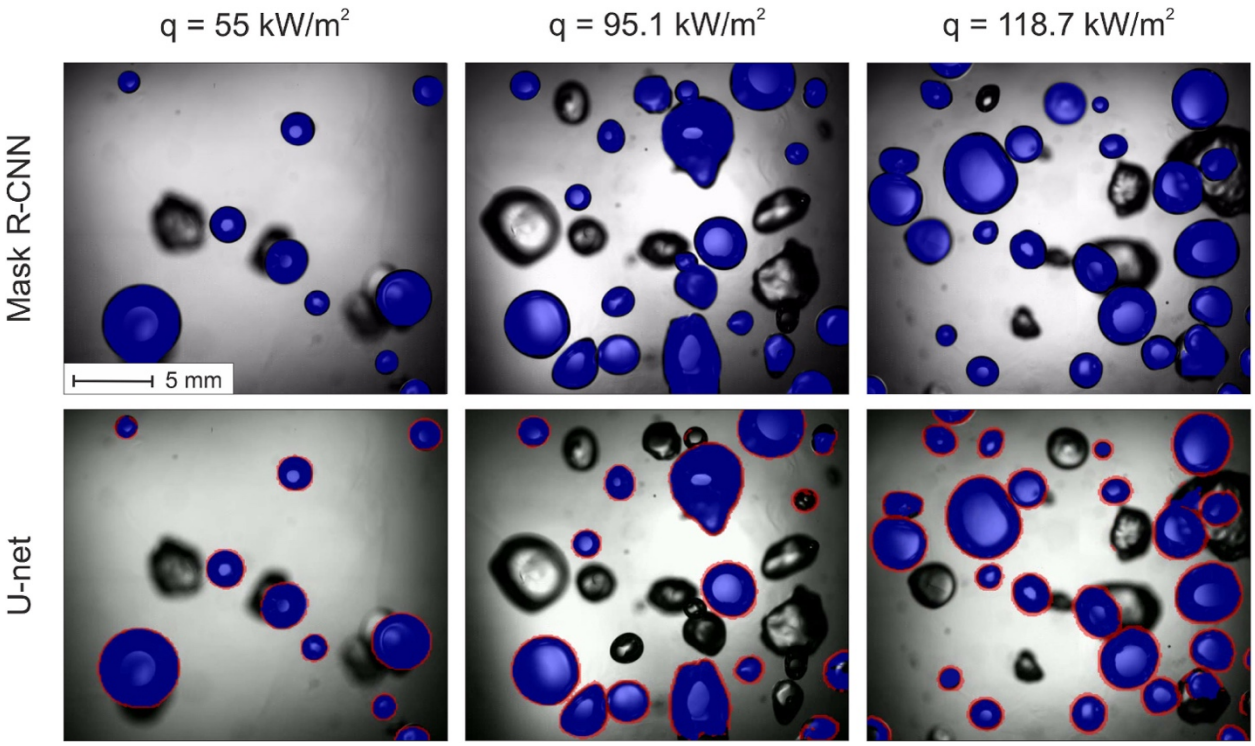

Figure 2.10 Image Segmentation Results by the CNN models) at various heat fluxes [8].

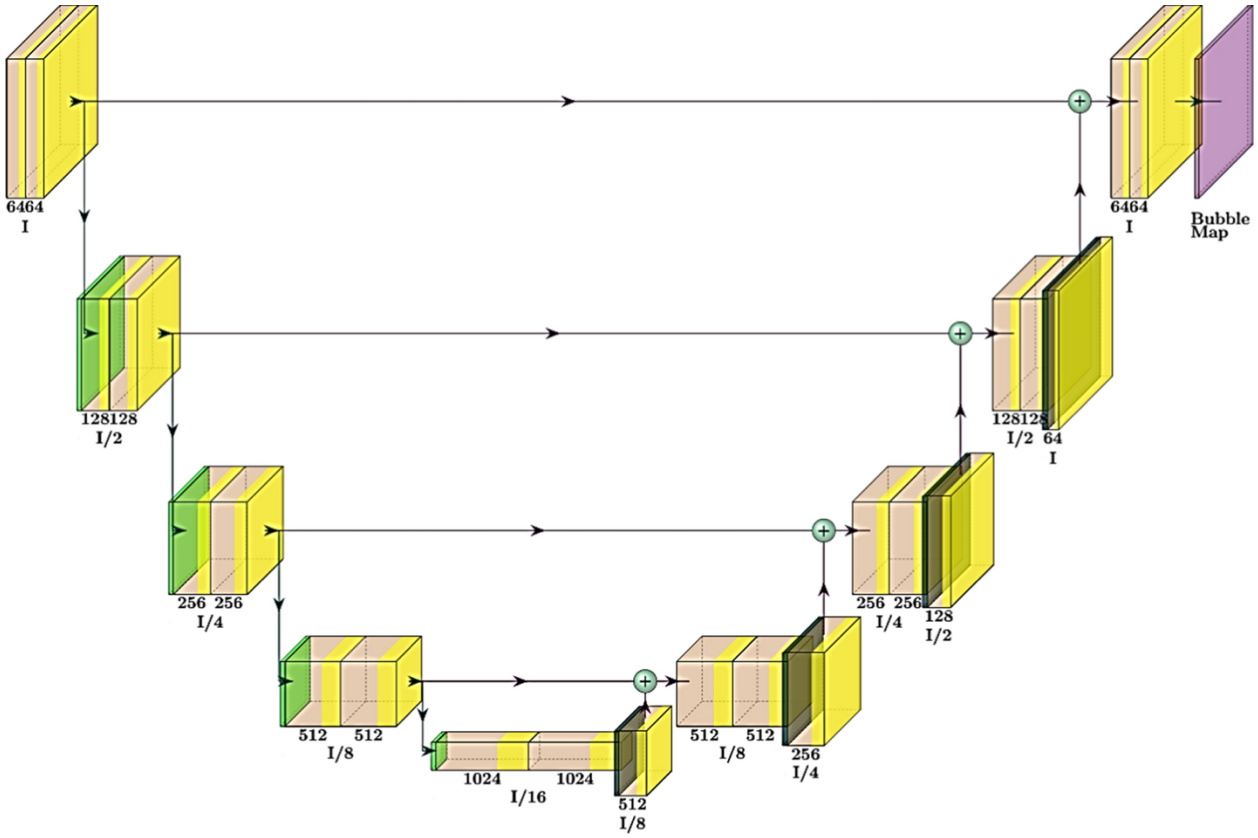

Figure 2.11 BIMSNet Architecture [21]

To ascertain critical boiling characteristics such as bubble departure diameter, departure frequency, and nucleation site density, Ahmed et al. [22] utilized Mask R-CNN models, initially trained on the COCO dataset, for the analysis of images derived from high-speed camera captures in two-phase flows. The experiments were conducted with R-134a as the working fluid under a heat flux of 18 kW/m^{-2}. While the segmentation of bubbles was effectively achieved, the precision in quantifying boiling parameters, including bubble departure diameters and nucleation site density, was compromised. This limitation was attributed to the challenges posed by the side-view experimental setup and the complexity of the applied machine learning algorithms.

The extensive review of existing literature underscores significant progress in developing deep learning models for the precise segmentation of bubbles in two-phase flows, demonstrating a marked superiority over traditional image processing methodologies reliant on adaptive thresholding. These conventional methods suffer from a lack of generalizability,

necessitating manual adjustments of filters for each specific experimental condition or flow scenario. The literature further reveals the effective implementation of transfer learning strategies within deep learning frameworks, particularly within Mask R-CNN (MS COCO) and U-Net CNN (biological cells) architectures, for segmentation of bubbles in high-speed video (HSV) images of two-phase flows. It is also noted that the source of pre-training in transfer learning plays a critical role in segmentation accuracy, with biological cell imagery often preferred due to its analogous domain characteristics to bubble dynamics.

However, there remains a notable gap in the application of transfer learning from biological cell models to phase-detection HSV imaging across a spectrum of fluids exhibiting complex bubble distributions and varied heat flux or operating conditions. Existing models fall short in their ability to segment bubbles from these intricate distributions with pixel-level accuracy. This thesis pioneers the use of transfer learning techniques to achieve precise bubble segmentation at the pixel level within complex phase-detection HSV images, spanning a diverse array of working fluids (such as liquid argon, nitrogen, high-pressure water, and FC72) and operational conditions. Our research proposes to advance this domain through the application of transfer learning, drawing insights from a domain closely related to bubble dynamics—biological cells. This approach is anticipated to facilitate more precise and effortless segmentation of bubble contours. Furthermore, our method leverages HSV data obtained from phase-detection videos at various heat flux conditions, offering a clearer distinction between liquid and bubble phases, thereby enhancing the accuracy of our measurements. The validity of the models is corroborated by comparing them with both ground-truth images, meticulously curated by domain experts and results obtained via adaptive thresholding. In a move towards enhancing accessibility and fostering further research, the sophisticated analytical tools developed in this work are made available as open-source resources, facilitating their adaptation to other two-phase flow scenarios.

Chapter 3

Methodology

This section details the methodology behind developing and applying Convolutional Neural Network (CNN) models for segmenting bubble footprints on a boiling surface, obtained using phase-detection. It includes steps from initial model development, incorporating transfer learning, to rigorous validation across different fluids such as liquid nitrogen, argon, FC-72, and high-pressure water. Our approach leverages existing deep learning architectures, adapting them to our specific task to surpass traditional image processing techniques in accuracy and efficiency. We outline the process of training these models, including data preparation, model adjustment, and the selection of metrics for evaluating performance. This section is designed to be clear and straightforward, providing enough detail for reproducing the results. We also explain how to use the developed models, offering guidance on deploying them for new datasets and ensuring that anyone interested can follow our steps to achieve similar results or extend our work. In short, this methodology aims to contribute to the broader field by offering a replicable model of research that others can adapt and build upon.

3.1Convolutional Neural Networks

The problem we address in this thesis is the accurate segmentation of bubbles in HSV phase-detection images, which is pivotal for extracting operating parameters like the bubble footprint size, contact line density, and dry area fraction on a boiling surface. Traditional image processing techniques, though widely used, often fall short when dealing with the complex and dynamic nature of bubble behavior, particularly under varying flow conditions and in different fluids [12,25,1]. These methods typically rely on fixed thresholding techniques, which lack the adaptability required to identify accurately and segment bubbles across a range of experimental settings, resulting in significant inaccuracies. The complexity of bubble segmentation is compounded by factors such as overlapping bubbles, variable lighting

conditions, and image noise, which traditional methods are ill-equipped to handle consistently. This leads to a gap in our ability to precisely analyze and understand the underlying physical processes in phase-detection images.

3.1.1 Network Architecture

The U-Net CNN architecture effectively segments complex images, such as those encountered in two-phase flow studies. Its design is tailored to capture intricate details and variations, making it exceptionally suited for bubble segmentation. The U-Net CNN was proposed in 2015 by Ronneberger et al., [26] for biomedical image segmentation purposes. The architecture of the U-Net CNN, as depicted in Figure 3.12, is distinctive for its symmetric shape, resembling the letter “U”. It consists of two main pathways: the contraction (downsampling) path and the expansion (upsampling) path. The contraction path is a typical convolutional network that captures the context in the image, enabling the model to understand the features present. This path consists of repeated application of two 3x3 convolutions (each followed by a rectified linear unit (ReLU) activation function) and a 2x2 max pooling operation with stride 2 for downsampling. At each downsampling step, the network doubles the number of feature channels.

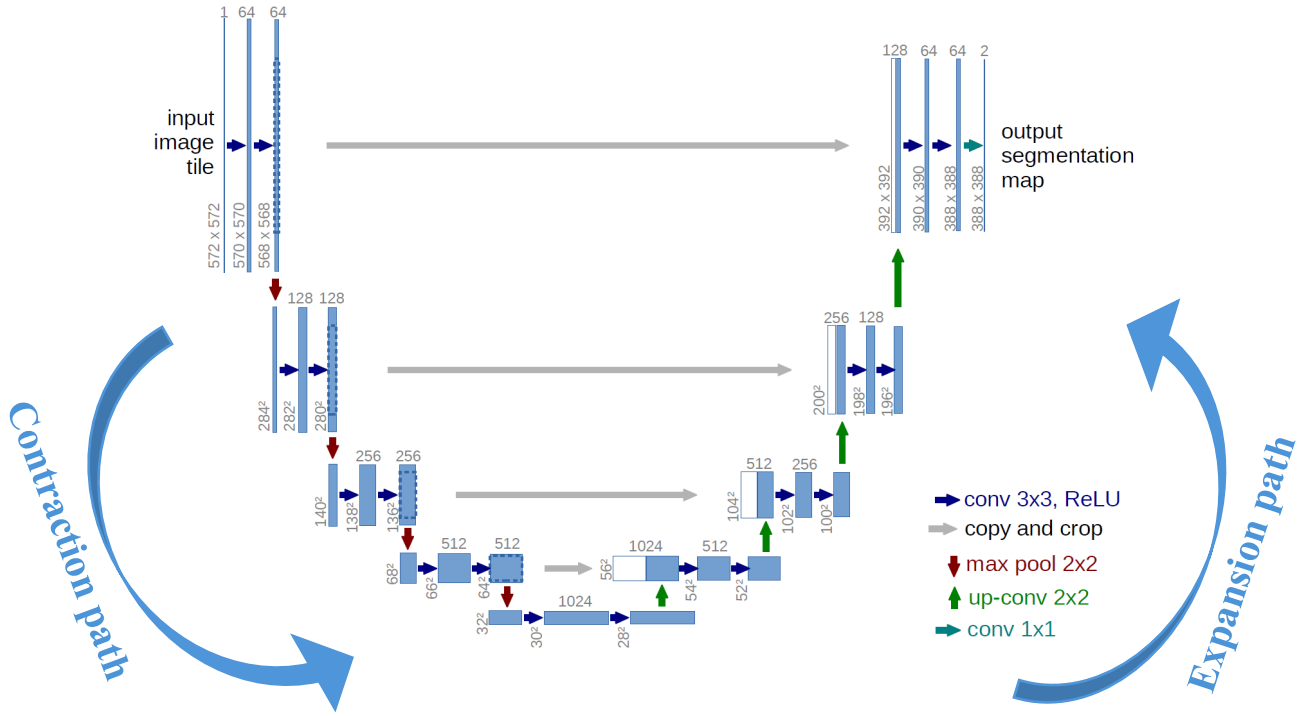

Figure 3.12 U-Net CNN Architecture [26].

The expansion path, on the other hand, enables precise localization, a crucial factor for accurate segmentation. This path includes a series of upsampling and convolution operations that progressively increase the resolution of the output maps. Specifically, it involves the up-convolution of the feature map followed by a 2×2 convolution ("up-convolution") that halves the number of feature channels, a concatenation with the correspondingly cropped feature map from the contraction path, and two 3×3 convolutions, each followed by a ReLU activation. This concatenation process from the contraction path to the expansion path is crucial for the U-Net architecture, as it allows the network to propagate context information to higher resolution layers, enabling precise localization.

The effectiveness of U-Net lies in its ability to learn spatial hierarchies of features through its deep, symmetrical architecture. At its core, U-Net leverages the concept of feature representation learning in deep convolutional networks, which can be mathematically described through the operations performed at each layer. The convolution operation applies

filters to input to create feature maps that summarize the presence of detected features. The operation can be mathematically represented as:

$$f_{ij}^{l} = \sigma\left(\sum_{m,n} w_{mn}^{l} \cdot x_{(i+m)(j+n)}^{l-1} + b^{l}\right) \quad (3.1)$$

where:

- f_{ij}^{l} is the feature at position (i, j) in the l^{th} layer,
- w_{mn}^{l} are the weights of the convolution filter in the l^{th} layer,
- $x_{(i+m)(j+n)}^{l-1}$ is the input from the previous layer at position $(i + m, j + n)$
- b^{l} is the bias term for the l^{th} layer,
- σ represents the activation function, typically ReLU for U-Net.

ReLU (Rectified Linear Unit) is used as the activation function in U-Net for introducing non-linearity:

$$\sigma(x) = \max(0, x) \quad (3.2)$$

Pooling operations reduce the spatial dimensions of the feature maps, effectively increasing the network's receptive field without increasing the computational cost. This is typically achieved through a max pooling operation defined as:

$$p(x) = \max_{i,j} \in N(x) x_{ij} \quad (3.3)$$

where $N(x)$ represents the neighborhood of pixels in the input feature map, x, over which the maximum is taken.

In the expansion path, the up-convolution operations use transposed convolution (or deconvolution) to increase the resolution of the feature maps. Mathematically, this can be described as the inverse of the convolution operation, aiming to distribute a single input value to multiple outputs to increase the spatial resolution of feature maps as follows:

$$g_{ij}^{l} = \sum_{m,n} w_{mn}^{l} \cdot h_{(i-m)(j-n)}^{l-1} \quad (3.4)$$

where g_{ij}^{l} is the output after applying the transposed convolution weights w_{mn}^{l} to the input $h_{(i-m)(j-n)}^{l-1}$.

The concatenation steps combine features from the downsampling path with the upsampled features, enriching the feature maps with both high-level contextual and low-level spatial information, which is essential for detailed segmentation.

The U-Net model is trained end-to-end on a set of training images with known segmentations (annotated samples), using a pixel-wise classification loss function, the cross-entropy loss for segmentation tasks. The cross-entropy loss is particularly effective for data with imbalanced classes, such as HSV phase-detection, where the region of interest occupies a small part of the image. The cross-entropy loss function is typically defined as:

$$L_{CE} = -\frac{1}{N}\sum_{i=1}^{N}[y_i \log(\hat{y}_i) + (1 - y_i)\log(1 - \hat{y}_i)] \quad (3.5)$$

where N is the number of pixels, y_i is the ground truth label, and $\hat{y}_i$ is the predicted probability that the given input belongs to class 1 (bubble).

For multi-class classification, where an instance can belong to one of many classes, the cross-entropy loss formula is extended to sum over all classes:

$$L_{CE} = -\sum_{c=1}^{C} y_c \log(\hat{y}_c) \quad (3.6)$$

where C is the number of classes, y_c is a binary indicator of whether class c is the correct classification for the observation, and $\hat{y}_c$ is the predicted probability that the observation belongs to class c.

The goal during training is to minimize this loss across all training examples, which effectively pushes the predicted probabilities closer to the actual labels, leading to a more accurate model.

3.1.2 Transfer Learning

Transfer learning is a powerful technique in deep learning that involves taking a pre-trained model and adapting it to a new, but related, problem. For U-Net CNNs, which are particularly adept at image segmentation tasks, transfer learning enables the model to leverage knowledge (weights and biases) learned from a vast amount of data on a different problem to enhance performance on specific tasks like bubble segmentation in two-phase flows. At its core, transfer learning modifies the U-Net architecture, which originally consists of a contracting path to capture context and a symmetric expanding path that enables precise localization. The process begins with a U-Net model pre-trained on a large dataset, potentially from a different domain. The essence of transfer learning lies in the ability of the CNN to retain and utilize the generic features (such as edges, shapes, and textures) learned during the pre-training phase and apply them to a new domain with minimal retraining.

The phases of transfer learning are described as follows:

1. **Feature Extraction Phase:** In the initial layers of the U-Net model, the convolution operations extract basic features from the input images. The operation in each convolutional layer, l, can be mathematically represented as:

$$F_l = \sigma(W_l \times X_l + B_l) \tag{3.7}$$

where F_l is the feature map produced by layer l, W_l represents the weights, X_l is the input to layer l, B_l is the bias, and σ denotes the ReLU activation function.

2. **Adaptation Layer:** During transfer learning, the deeper layers of the network, which are more task-specific, are fine-tuned for the new task. The adaptation can be represented as adjusting the weights W_l and biases B_l in these layers through backpropagation, minimizing a loss function L specific to the new task:

$$W_l', B_l' = argmin_{W_l, B_l} L(Y, \hat{Y}) \tag{3.8}$$

where Y is the true label, $\hat{Y}$ is the predicted label, and L denotes the loss function, which is the cross-entropy loss for segmentation.

3. **Fine-Tuning Process:** The fine-tuning adjusts the model to the specifics of the new task, optimizing the performance by updating the model parameters:

$$\Delta W_l = -\eta \frac{\partial L}{\partial W_l}, \Delta B_l = -\eta \frac{\partial L}{\partial B_l} \tag{3.9}$$

here, η represents the learning rate, and the partial derivatives represent the gradient of the loss function with respect to the weights and biases.

To implement transfer learning in U-Net, we follow these steps:

1. **Selection of a Pre-trained Model:** A U-Net model pre-trained on a substantial and pertinent dataset is crucial for effective transfer learning. The dataset utilized for pre-training plays a significant role in the success of this approach. For our project, we opted for a U-Net model initially trained on a comprehensive collection of biological cell imagery [24,26]. This decision was motivated by the similarity between the cellular structures in the pre-training dataset and the bubble features present in our own datasets.
2. **Feature Adaptation:** We froze the initial layers of the model to retain the generic features learned during pre-training. Only the deeper, task-specific layers are fine-tuned to adapt to the new segmentation task. This fine-tuning involved adjusting the learning rate within a specified range of 10^{-3} to 10^{-4} while also varying the number of

learning iterations based on the complexity of the target dataset. In all cases, a few frames are required to finetune the U-Net model. Five images are used, of which three are used for training, and two are used for validation. The use of few annotated samples for finetuning the models is beneficial. It is why transfer learning is adopted, as procuring these annotated frames is expensive and time-consuming. Additionally, our observations revealed that fewer iterations were sufficient in scenarios where the bubbles appeared significantly larger or smaller. This efficiency is attributed to the similarity between these bubble sizes and the cellular images on which the model was initially trained; hence, less learning was required. However, in cases where the dataset presented a mix of many small and large bubbles, achieving a higher accuracy level necessitated an increase in the number of iterations and a decrease in the learning rate since more learning is required for accurate segmentation.

4. **Loss Function Optimization:** While finetuning, we used the cross-entropy loss to monitor the progress of the training process and ensured that the loss was decreasing with each increase of iterations; hence, learning was taking place. Furthermore, we used numerous performance metrics typical in computer vision tasks like accuracy, precision, recall, specificity, F_1 score, intersection over union (IoU), and Matthews correlation coefficient (MCC), as defined in the next section.
5. **Iterative Fine-Tuning:** Through iterative training sessions, we adjust the model parameters in the task-specific layers, refining the model's ability to segment images accurately for the new task.

3.2 Data Acquisition

Our analysis leverages experimental high-speed video (HSV) recordings from boiling experiments involving liquid nitrogen, argon, FC-72, and high-pressure water. Specifically, we examined 18 phase-detection videos for liquid nitrogen, each comprising 2000 frames, under heat fluxes ranging from 27 kW/m^2 to 297 kW/m^2. Additionally, we analyzed constant heat flux HSV data for liquid argon (120 kW/m^2), nitrogen (120 kW/m^2), and FC-72 (170 kW/m^2), allocating 6000 frames for each fluid under baseline conditions. Our dataset also

includes two videos with 7,501 frames each for high-pressure flow boiling of water, also collected under constant heat flux conditions of 3000 kW/m^2 and 3400 kW/m^2, respectively. The initial phase involves carefully selecting frames from this vast dataset for training, validation, and testing. We employ a random selection script in the project repository to ensure a representative sample across various boiling conditions and bubble distributions. This randomness ensures our training set comprehensively captures the diversity of bubble behavior. We train different specialized models for the various fluids to ensure a high level of segmentation accuracy. Given the raw state of these recordings, which include noise and irrelevant background details, preliminary data processing is essential. Utilizing "crop" scripts from our repository, we refine the frames, eliminating extraneous information to focus on the relevant phenomena. This preprocessing step is illustrated with an example from the high-pressure water HSV dataset in Figure 3.13. We select at least 10 samples from the processed data to construct our training set. This selection is then divided into 4 samples for training, 1 for validation, and 5 for testing the model post-training. Subsequent sections will delve into the detailed processing of these frames, including annotation and preparation for our transfer learning pipeline.

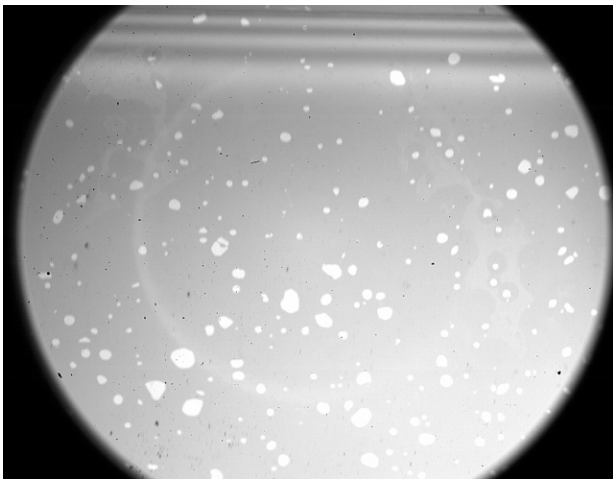

Figure 3.13 Raw Image

3.3 Data Annotation

Creating annotated samples from HSV recordings of boiling data is a demanding task. Domain experts often need to meticulously identify and delineate regions of interest (ROIs) around

numerous bubbles within complex frames. We introduce a method that leverages feature transfer to streamline this process, significantly simplifying the annotation task as depicted pictorially in

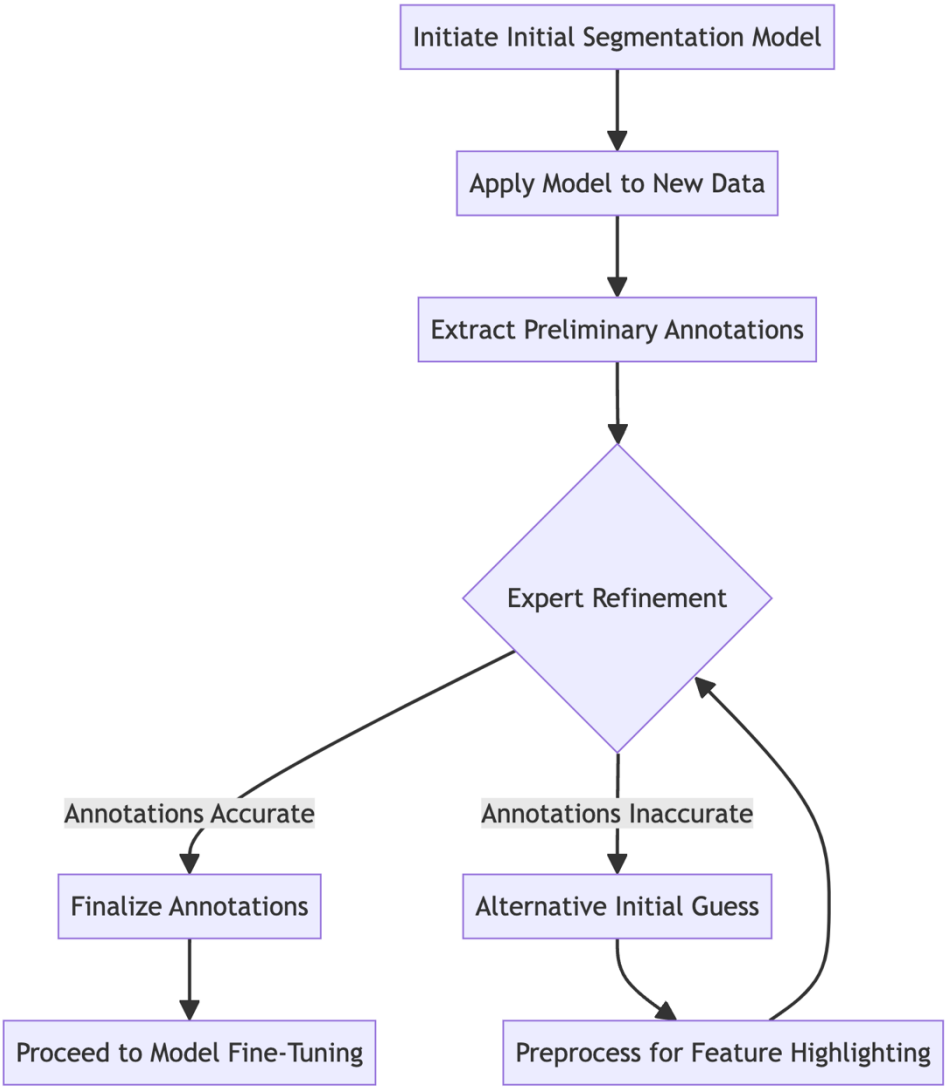

Figure 3.14.

This method begins by utilizing a previously successful model in bubble segmentation under different conditions to perform zero-shot segmentation on new HSV frames. Given that these frames are novel to the model, initial segmentation results might not meet high standards. However, this preliminary step is invaluable as it provides a basic outline of potential ROIs. We then employ the “mask” Fiji macro in the repository to refine these outlines, extracting ROI features from the initial segmentation and transferring them to our target HSV frames as

preliminary annotations. This process benefits greatly from subsequent refinement by domain experts, who can adjust and improve the quality of these annotations, ensuring accuracy and relevance. In situations where a directly applicable U-Net model is unavailable for initial segmentation, we can resort to basic image processing techniques to establish a foundational guess. While this initial pass may lack precision, it is an effective starting point, accelerating the annotation process by providing a rough baseline for expert refinement. This streamlined approach to generating annotations is summarized in Table 3.1.

Additionally, image normalization plays a crucial role in preparing the data for feature transfer. By employing the "process" script from our repository, we enhance the visibility of bubbles against the background. This preprocessing step involves subtracting the frame from a clear reference image and adjusting the contrast to accentuate relevant features, facilitating easier annotation and subsequent model training. With these annotated samples prepared, the next stage of our methodology focuses on finetuning the model through transfer learning. This approach speeds up the annotation process and offers substantial advantages over building a segmentation model from scratch, as detailed in the following section. Finally, to eliminate bias in the annotation phase, the effect of user experience on the data annotation was conducted by letting different domain experts independently annotate the same frames and compare them to the ground truth through visual inspection and quantitative boiling metrics. Through this innovative pipeline, we significantly reduce the time and effort required to generate high-quality training data for U-Net CNN models segmenting complex boiling phenomena.

Table 3.1 Enhanced Annotation Process via Feature Transfer

Step	Action
1	**Initiate Zero-shot Segmentation:** Load a pre-existing U-Net model trained on a different dataset for initial segmentation.
2	**Apply Model to New Data:** Use the model to segment new HSV boiling frames, acknowledging initial results may be imprecise.

3	**Extract Preliminary Annotations:** Utilize the "mask" Fiji macro to extract ROI features from the predicted mask and transfer them to the target HSV frames as initial annotations.
4	**Expert Refinement:** Domain experts review and refine the preliminary annotations, adjusting as necessary to ensure accuracy and completeness.
5	**Alternative Initial Guess (if needed):** If a suitable pre-trained model is not available, apply basic image processing techniques to create an initial guess for ROIs.
6	**Preprocess for Feature Highlighting:** Normalize images using the "process" script to enhance feature visibility, facilitating easier annotation.
7	**Finalize Annotations:** With expert adjustments, finalize the annotations for use in training or fine-tuning the segmentation model.
8	**Proceed to Model Fine-Tuning:** Utilize the annotated samples for fine-tuning the model via transfer learning, optimizing for the specific task of bubble segmentation in boiling data.

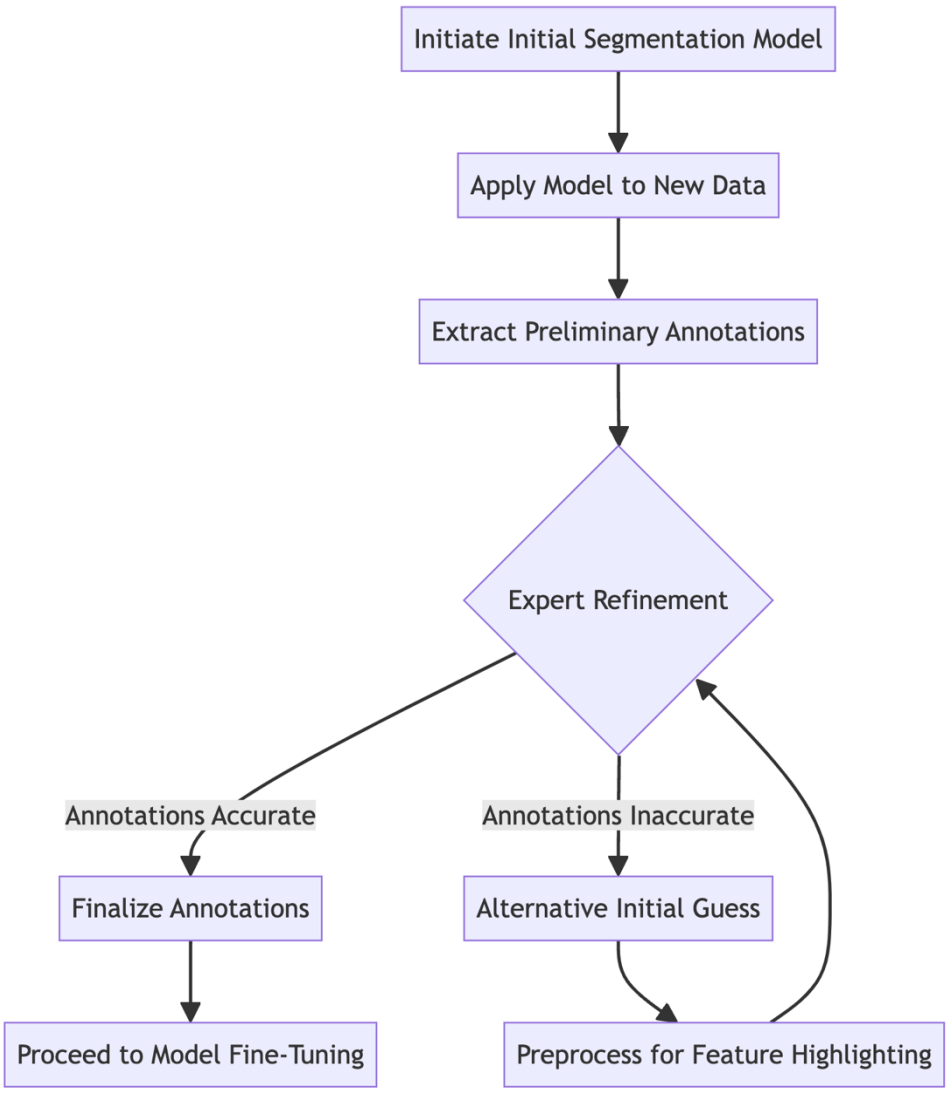

Figure 3.14 Feature Transfer to Facilitate Creating Annotations for Transfer Learning.

3.4 Validation and Metrics

Following the fine-tuning phase, assessing the machine learning model's efficacy is crucial by employing it to segment images it has not encountered during the training process. For this purpose, we selected 5 images outside the training dataset and subjected them to segmentation by the fine-tuned model. To establish accurate benchmarks, these validation images were accompanied by corresponding annotations crafted manually by experts within the relevant

field, providing the essential ground truths. These 5 validation images were chosen randomly to encompass the wide-ranging distributions observed within the HSV dataset.

The evaluation began with a visual inspection to compare the segmented images against the original camera images, focusing particularly on the alignment of bubble features between the two. This comparison helped identifying any discrepancies in perimeter alignment. In instances of misalignment, the process necessitates a return to the fine-tuning stage for adjustments. Conversely, when the visual assessment indicates a satisfactory alignment, we proceed to quantify the model's performance by calculating key metrics related to boiling dynamics and machine learning efficacy, using the manually annotated ground truths and the segmented outputs as reference points.

3.4.1 Boiling Performance Metrics

To evaluate the precision of segmentation facilitated by the U-Net model for boiling phenomena, we calculate and contrast key performance metrics, specifically dry area fraction and contact line density, against those derived from the ground truth images. Here, we delve into the definitions and computational methods for these metrics from a thermal-hydraulic perspective:

1. **Dry Area Fraction ($\boldsymbol{\theta_{dry}}$)** This metric represents the ratio of the surface area within the image that remains unexposed to liquid, i.e., the "dry" area. It is a critical parameter for understanding heat transfer efficiency and phase change dynamics in boiling processes. To compute this fraction, we first identify the pixels corresponding to dry areas (non-wet pixels) within the binary mask representation of the image. The dry area fraction is then calculated by deducting the ratio of wet pixels from one, essentially reflecting the proportion of the surface where the liquid is not present. θ_{dry} is calculated using Equation (3.10).

$$\theta_{dry} = 1 - \frac{Wet\ Pixels}{Total\ Pixels} \tag{3.10}$$

2. **Contact Line Density ($\boldsymbol{\rho_{cl}}$)**: This metric assesses the extent of the contact line per unit area within the image, where the contact line is the interface between liquid-covered and dry surfaces. This interface is pivotal in boiling heat transfer as it delineates the zones of intense evaporation and significantly influences thermal transport

effectiveness. The calculation involves inverting the binary mask to focus on the interfaces, applying a Euclidean distance transform to identify the boundary lengths, and adjusting for pixel scale to ensure accurate measurement. The density of the contact line is thus a measure of the boundary length normalized by the image area, providing insight into the surface characteristics relevant to boiling and evaporation. Equation (3.11) shows how to calculate ρ_{cl}.

$$\rho_{cl} = \frac{Contact\ Line\ Length}{Total\ Pixels} \tag{3.11}$$

We have provided the "bubblemetrics" function to handle this task in the repository [27]. Additionally, we have provided a detailed overview (Table 3.2) of how to compute these boiling metrics using the scripts in our repository. This algorithm assumes that the pixelization is perfect; however, we investigate the discretization error inherent in the pixelization due to the bubble radius and grid resolution using the "bubble_discretization" code in the repository [27]. This analysis is covered in Chapter 4.

Table 3.2 Algorithm for Calculating Dry Area Fraction and Contact Line Density

Step	Action	Description
1	Input binary mask **binaryMask**.	The binary mask represents the segmented image, where '1's denote dry pixels and '0's denote wet pixels.
2	Calculate **totalPixels**.	Count the total number of pixels in **binaryMask** using **numel(binaryMask)**.
3	Calculate **dryPixels**.	Sum all pixels in **binaryMask** that are equal to 1, indicating dry areas.
4	Calculate **dryAreaFraction**.	Compute **dryPixels / totalPixels** to find the proportion of the image that is dry.
5	Invert **binaryMask** to **invertedBinaryMask**.	Create an inverted mask where '0's become '1's and vice versa, focusing on wet areas and their boundaries.
6	Apply distance transform to **invertedBinaryMask**.	Use **bwdist(invertedBinaryMask)** to calculate the Euclidean distance to the nearest non-zero (dry) pixel.
7	Calculate **contactLineLength**.	Sum pixels in the distance transform result that have a value of 1, identifying the immediate contact line.
8	Calculate **contactLineDensity**.	Divide **contactLineLength** by **totalPixels** to find the contact line's extent per unit area.
9	Output **dryAreaFraction** and **contactLineDensity**.	Package the results into a structure or output them directly as the algorithm's result.

3.4.2 Machine Learning Metrics

The machine learning performance metrics provide another layer of validation to the quality of the segmentation outputs predicted by the U-Net CNN. The confusion matrix needs to be calculated first to calculate these metrics. The confusion matrix (Table 3.3) is evaluated by calculating the following:

Table 3.3 Confusion Matrix

TP	FP
FN	TN

- **True Positive (TP):** - This is the number of positive pixels (bubble pixels) in the segmented image that correctly match the positive pixels in the ground truth.
- **False Positive (FP):** - This is the number of positive pixels in the segmented image that do not match the positive pixels in the ground truth (i.e., wrongly identified).
- **False Negative (FN):** - This is the number of negative pixels (liquid pixels) in the segmented image that do not match the negative pixels in the ground truth.
- **True Negative (TN):** - This is the number of negative pixels in the segmented image that correctly match the negative pixels in the ground truth.

Then, the performance metrics are computed from the confusion matrix as:

1. **Accuracy $(\mathbf{0 \leq A \leq 1})$:** This measures the proportion of the total number of correct predictions. It's computed as:

$$A = \frac{(TP + TN)}{(TP + TN + FP + FN)} \tag{3.11}$$

2. **Precision $(\mathbf{0 \leq P \leq 1})$:** Precision measures the correct positive predictions made. It's computed as:

$$P = \frac{TP}{(TP+FP)} \tag{3.12}$$

3. **Recall $(\mathbf{0 \leq R \leq 1})$:** Recall (or Sensitivity or True Positive Rate) measures the number of actual positives that were correctly identified.

   It's computed as:

$$R = \frac{TP}{(TP+FN)} \tag{3.13}$$

4. **Specificity $(\mathbf{0 \leq S \leq 1})$**: (Specificity or True Negative rate) measures how well the model can correctly predict a true negative for each category.

   It is calculated as:

$$S = \frac{TN}{(TN+FP)} \tag{3.14}$$

5. **F_1 Score ($0 \leq F_1 \leq 1$):** The F_1 Score or Dice coefficient is the harmonic mean of Precision and Recall and gives a better measure when there are uneven class distributions (such as many negatives and fewer positives).
   It's computed as:
   $$F_1 = 2 \times \frac{P \times R}{P+R} = \frac{2 \times TP}{2TP+FP+FN} \quad (3.15)$$
6. **Intersection over Union ($0 \leq IoU \leq 1$):** IoU or Jaccard index measures the overlap between the segmented image and the ground truth. It's the area of overlap divided by the area of union of the two segments. It's computed as:
   $$IoU = \frac{TP}{TP+FP+FN} \quad (3.16)$$
7. **Matthews Correlation Coefficient ($-1 \leq MCC \leq 1$):** MCC is a measure of the quality of binary classifications. It considers all four values of the confusion matrix and is a balanced measure even if the classes are of different sizes. It is computed as:
   $$MCC = \frac{(TP \times TN) - (FP \times FN)}{\sqrt{(TP+FP) \times (TP+FN) \times (TN+FP) \times (TN+FN)}} \quad (3.17)$$

3.5 Uncertainty Quantification

In this subsection, we analyze binarized frames to address the precision of measuring key boiling dynamics, specifically contact line density and dry area fraction. Recognizing that pixel-based measurements inherently carry some degree of error, it's essential to quantify these uncertainties to enhance our understanding of the estimations made for the contact line and dry area. To systematically address potential errors, we utilize the "bubble_discretization" script, which employs "dilation" and "erosion" techniques to adjust for overestimations and underestimations, respectively. By varying the grid resolution and bubble radius across a set number of iterations, we compare the theoretical area and perimeter (assuming a perfect circular shape) against the discretized values calculated from the pixel data. The core of our analysis involves calculating the relative and mean errors between these theoretical and discretized measurements and correlating them with the bubble radius and grid resolution. Next, we extract real bubble dimensions (radius, area, and perimeter) from experimental data to further validate our approach. This validation allows us to adjust the error estimates based on actual measurements, ensuring a more accurate and reliable analysis. A distinctive aspect of our method is applying a weighted frequency analysis through a Python script

("weighted_average"), which assesses errors across various bubble sizes according to their occurrence frequency obtained using the "bubble_distribution" code. This technique provides an accurate perspective on error distribution, facilitating more precise uncertainty estimations for contact line and dry area measurements.

Table 3.4: Enhanced Bubble Discretization and Error Quantification

Input: Domain length L, NumSimulations, N_{values}, R_{values}

Output: Results with PRE and ME for area and perimeter

1. **Initialize simulation parameters**
2. **for** each N in N_{values} **do**
    a. **for** each R in R_{values} **do**
        i. Initialize $A_{theoretical}$, $P_{theoretical}$ for R
        ii. **for** k=1 **to** NumSimulations **do**
            1. Randomly position bubble within domain
            2. Calculate Dis, define bub ($Dis<R$)
            3. Compute A_{bub}, $Perb$ using pixel count
        iii. **end for**
        iv. Compute PRE and ME for area, perimeter
        v. Store errors in Results
    b. **end for**
3. **end for**
4. Load and process Results for visualization
5. Extract error matrices from Results
6. Visualize errors (Histograms, Surface plots)
7. Estimate errors for experimental data:
    a. Match experimental data with simulation parameters
    b. Read off errors for specific experimental conditions
8. Perform weighted frequency analysis on errors
9. Output refined error estimations

Table 3.4 provides a comprehensive algorithm detailing the steps in conducting the error quantification. The algorithm table outlines a process for simulating and analyzing the discretization of bubbles within a domain of length L. It involves running a specified number of simulations, given by "**NumSimulations**", over a range of grid resolutions and bubble radii, represented by "**N_values**" and "**R_values**", respectively. The aim is to calculate the area and perimeter of bubbles as they would appear on a discrete grid, comparing these results with their theoretical continuous counterparts. Within this context, "**A_theoretical**" and "**P_theoretical**" represent a bubble's expected area and perimeter with a known radius R, as determined by geometrical formulas. For each simulation iteration indexed by k, the algorithm places a bubble randomly within the domain. It calculates the distances from points on the grid to the bubble's center, referred to as "**Dis**". This distance defines which grid cells, or "**bub**", are inside the bubble. The algorithm then counts these cells to estimate the bubble's area ("**Abub**") and perimeter ("**Perb**").

Figure 3.15 shows how the points which belong to the discretized bubble are determined. From the plot, we present the outcomes of the discretization process for a simulated bubble superimposed with its theoretical counterpart across different grid resolutions, denoted by $\boldsymbol{N}$. As $\boldsymbol{N}$ increases, the numerical representation of the bubble, indicated by the filled purple area, converges towards the theoretical model, delineated by the blue outline. At lower resolutions ($\boldsymbol{N}$ **= 10, 20**), the pixelation is quite apparent, leading to a more polygonal shape rather than a smooth curve. This effect diminishes as $\boldsymbol{N}$ reaches 45, and further resolution improvement to $\boldsymbol{N}$ **= 100** yields a discretized bubble that closely approximates the smooth, circular theoretical model. This progression illustrates the impact of grid resolution on the accuracy of numerical simulations in representing continuous shapes within a discrete spatial domain. To ensure robust statistical significance, we repeated this computation 500 times for each pair, thus mitigating any anomalies caused by the bubble's random positioning.

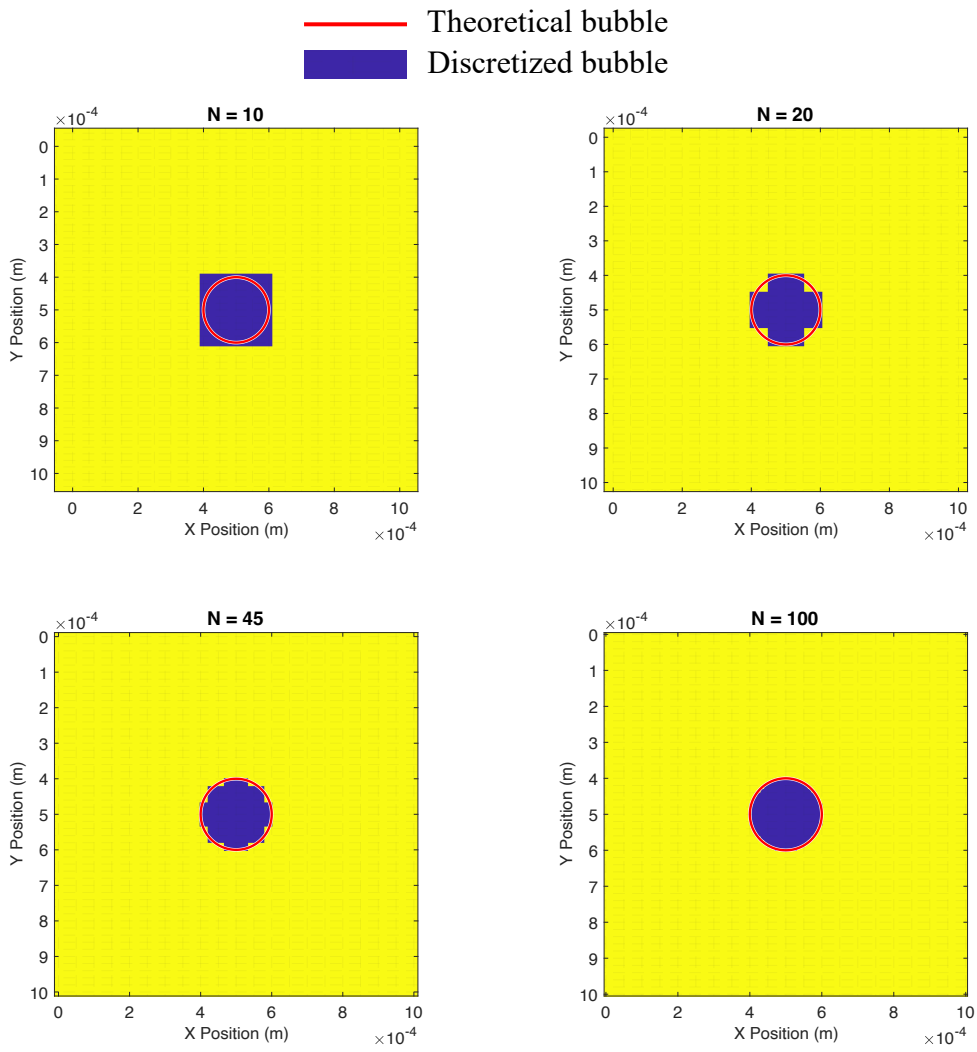

Figure 3.15 Theoretical and Discretized Bubble for a Fixed Bubble Radii (100 microns) and Varying Grid Resolution (N)

After running the specified number of simulations, the algorithm computes the Percentage Relative Error ("**PRE**") and Mean Error ("**ME**") for both the area and the perimeter to evaluate the accuracy of the discretization. The "**PRE**" measures the error relative to the size of the measured value, while the "**ME**" gives an average of the errors across all simulations. The results from this rigorous procedure provide a refined estimation of errors that can be expected when representing continuous shapes in a discrete space, which is crucial for applications in computer vision and related fields. The subsequent sections present the

results obtained from the segmentation study for the diverse fluids at various operating conditions and the uncertainty quantification results.

Chapter 4

Case Studies

This chapter is focused on presenting the results of the segmentation of HSV frames in boiling experiments. The fluids considered are liquid nitrogen (at 16 distinct heat fluxes with 2000 frames per heat flux), liquid argon, nitrogen, and FC-72 (at constant operating conditions with 6000 frames per fluid). We also consider high-pressure water as a working fluid to demonstrate the model's efficacy on water bubbles. All these data were collected by The Red Lab members. The first results focus on the liquid nitrogen experimental data at various heat fluxes, offering insights on how the segmentation and thresholding methods perform on the data. After that, the effects of different user perspectives on selecting the ground truth images used to validate the U-Net segmentation masks is presented and discussed. Subsequently, we show the comparisons between the U-Net CNN segmentation and the adaptive thresholding techniques on other use cases.

4.1Liquid Nitrogen at Varying Heat Fluxes

This section discusses various aspects of the binarization of the liquid nitrogen HSV phase detection images using U-Net CNN and thresholding techniques. It starts with boiling metrics evaluation (e.g., contact line density and dry area fraction) for the various HSV images recorded at different heat fluxes. Thereafter, the data categorization which breaks down the HSV data into various categories based on bubble topology similarity as well as specialized models that accurately handle each data are presented. After that a 3D histogram analysis of the data is presented which shows the bivariate distribution of bubble size and the frequency of occurrence for the different videos from both techniques. Then, perimeter visualization as well as a bubble size distribution analysis are presented to further show the reason for the observed trends in the results obtained from both methods.

4.1.1 Boiling Metrics

The liquid nitrogen HSV data was recorded in saturated (i.e., 93.5 K at 70 psia) pool boiling conditions. Figure 4.16 shows how the contact line density and dry area fraction of liquid nitrogen fluid changes as the mean heat flux increases. It compares two different methods: segmentation using the U-Net CNN and adaptive thresholding. The adaptive thresholding algorithm was implemented by Chavagnat et al. and was used in their work [28,29]. Both methods show that as the mean heat flux goes up, so does the contact line density and the dry area fraction. In simple terms, when we apply more heat, the density of the contact line— which is the edge or boundary where a liquid might meet a surface— as well as the dry area fraction—which is the surface area covered by vapor gets higher.

The blue line represents the U-Net CNN segmentation method, and the red line represents the thresholding method. Both lines follow a similar trend, but there are some differences. It is observed that the segmentation method gives a slightly higher density and dry fraction than the thresholding, especially as we apply more heat. Most importantly, at steps 8-9 (corresponding to heat fluxes of 140.5 and 158 kW/m^2, respectively), a significant deviation between methods is observed and after that, the changes keep getting more prominent. This may be because the segmentation technique is picking more bubbles than the thresholding method. Furthermore, it may be that there is an increase of smaller bubbles from video 8-9 in the plot and that the thresholding technique does not capture these small bubbles in video 9 while the segmentation does well in capturing them due to its higher sensitivity during the tuning process. Subsequent results will seek to show these different regimes and investigate the reasons for these differences between the two techniques.

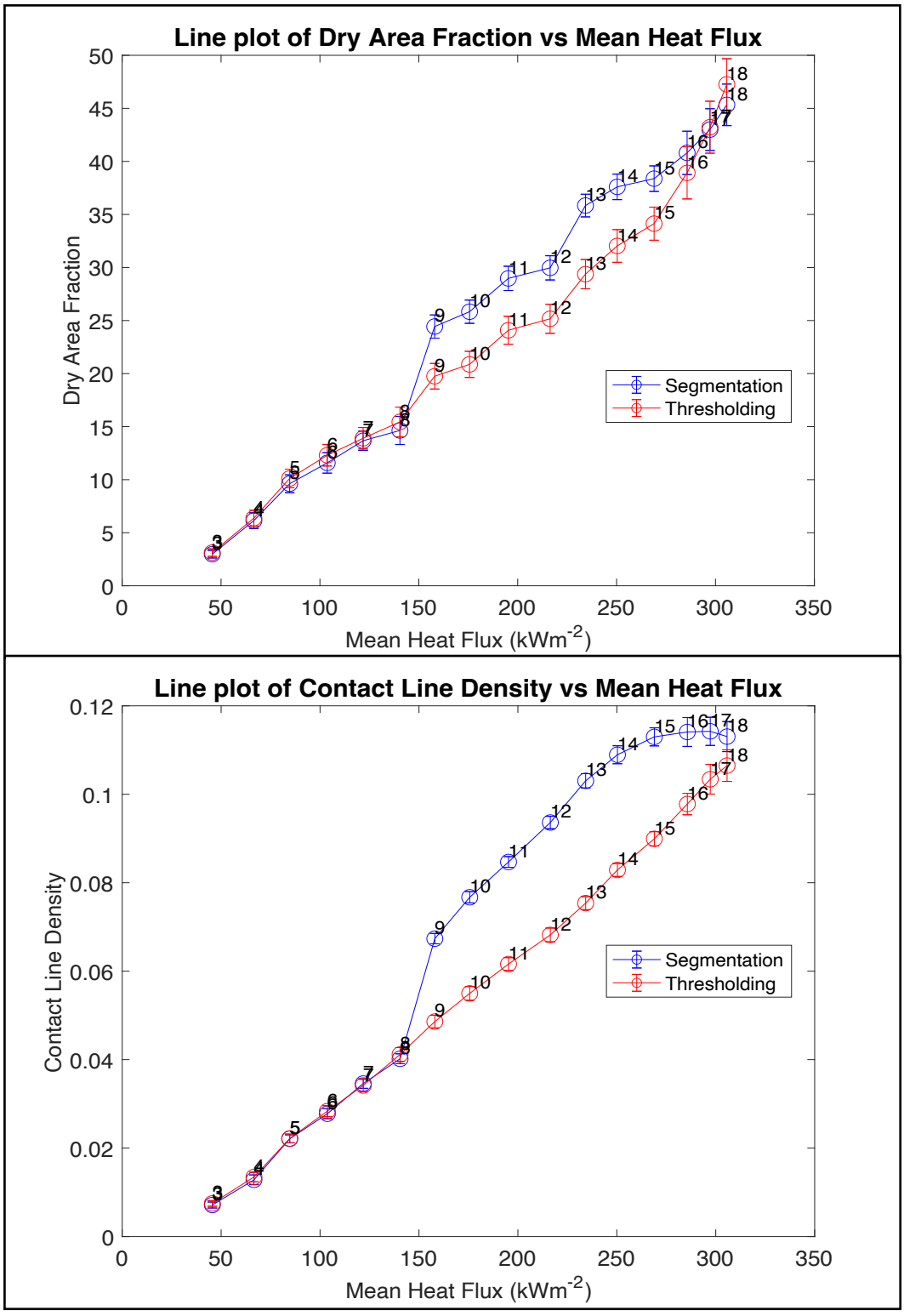

Figure 4.16 Variation of Dry Area Fraction and Contact Line Density with Increasing Mean Heat Flux: A Comparative Analysis of U-Net CNN Segmentation and Thresholding Methods

4.1.2 Data Categorization

Figure 4.17 and Table 4.5 provide a comprehensive visual and quantitative analysis of the behavior of liquid nitrogen under various heat flux conditions, processed through U-Net CNN models and thresholding. In Figure 4.17, we see a series of images depicting the state of liquid nitrogen as captured by the camera and then processed using U-Net CNN and thresholding techniques. This visualization divides videos 3-18 into 5 major categories based on the similar bubble topology. Based on these categories, 5 specialized U-Net CNN models are created for the entire HSV data as illustrated in Table 4.5. The creation of these diverse models for different heat flux ranges are necessary because the characteristics of the bubbles change with heat flux, requiring tailored approaches for capturing as much bubble pixels as needed. The raw camera images, displayed in grayscale, reveal a transition from scattered bright spots indicating low vapor-covered surface at lower heat flux (1) to densely packed patterns at higher heat flux (5), suggesting a more vigorous boiling state.

As the heat flux increases, we observe a clear increase in bubble formation and density. The U-Net CNN processed images present these transformations with stark contrast, emphasizing the distinction between the liquid (dark) and vapor (bright) states of nitrogen. With rising heat flux, the bubbles, which represent the vapor phase, increase, suggesting an increase in the boiling intensity. The bottom row images, processed with thresholding, show vapor-covered area in yellow and the liquid background in blue.

It is generally observed that the U-Net CNN is better at detecting small bubbles in the camera image than the adaptive thresholding technique. It is important to detect these small bubbles, especially at higher heat flux levels, to precisely quantify contact line density and dry area fraction which are key to correctly predict the boiling heat transfer coefficient. This observation is more pronounced at higher heat flux levels and subsequent visualizations will seek to further uncover these differences especially from videos 8-9. This visualization method makes the changes of the boiling process from gentle to vigorous starkly apparent. Table 4.5 complements these visualizations with precise heat flux ranges, associating each HSV with a specialized U-Net CNN model and referencing specific applicable videos.

A concise explanation as to how the thresholding technique works and why it seems to be less effective at capturing small bubbles compared to U-Net CNN is provided. The

thresholding technique is a simple, yet effective image processing method that converts grayscale images into binary by applying a specific threshold value. Any pixel intensity above the threshold is turned to one color (e.g., white), and anything below is turned to another color (e.g., black). This creates a binary image that highlights areas of interest, like the bubbles in the liquid nitrogen experiments, against the background. However, thresholding might be less effective at capturing small bubbles because it applies a varying intensity cutoff across the entire image which may not pick up smaller bubbles especially when the image contrast does not clearly differentiate the bubble from the background. This can cause it to miss subtleties, such as very small bubbles that do not contrast sharply with the background. If these bubbles are close in intensity to the liquid nitrogen background, they might be incorrectly classified as part of the background and thus not detected. In contrast, a U-Net CNN is a more advanced, machine learning-based approach that learns from the data how to identify features of interest, such as bubbles. It can recognize patterns and textures, adapting to variations in bubble size, shape, and intensity. This enables the U-Net CNN to detect smaller and less distinct bubbles that may be overlooked by thresholding, making it a more robust tool for detailed image analysis in complex visual datasets like ours.

Table 4.5 Classification of the Liquid Nitrogen HSV Dataset at Various Heat Fluxes According to U-Net Models

S/N	Heat flux (kW/m^2)	U-Net model	Videos
(1)	**45.6-66.6**	**Img_3**	3,4
(2)	**84.7-103.7**	**Img_5**	5,6
(3)	**121.8-140.5**	**Img_8**	7-9
(4)	**158-216.4**	**Img_12**	10-12
(5)	**234.3-305.7**	**Img_16**	13-18

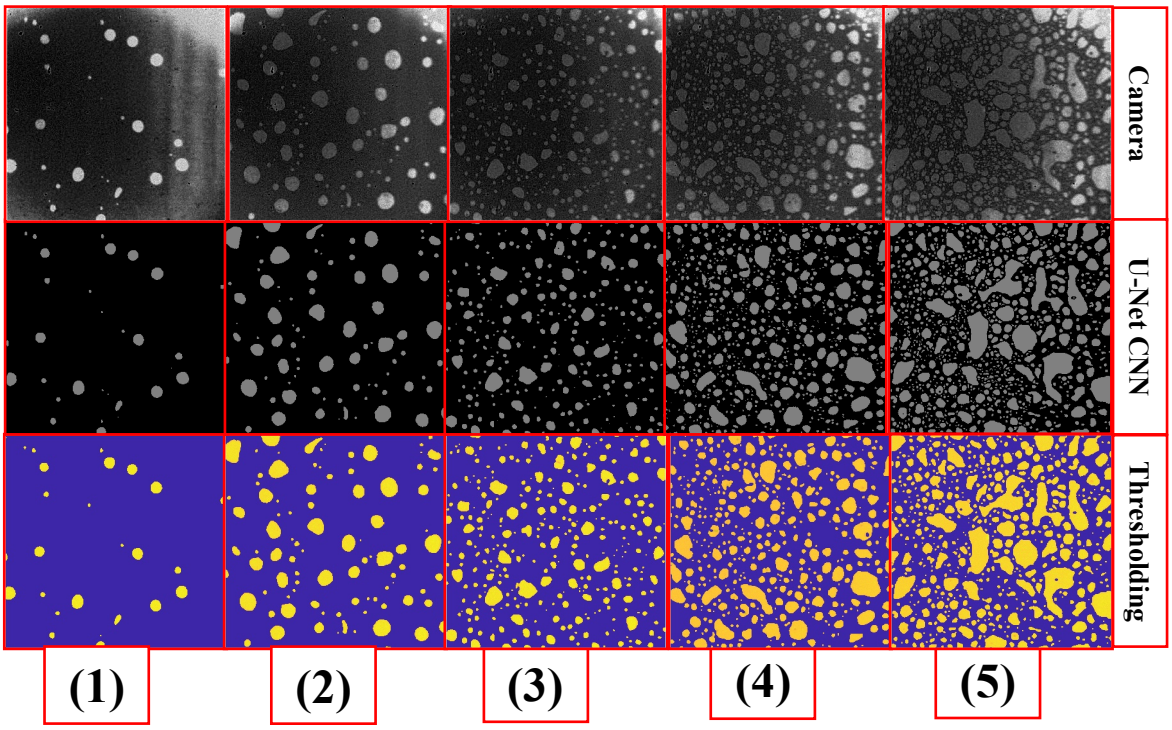

Figure 4.17 Visualization of Sample HSV Data Represented in the Classification Table

4.1.3 Data Analysis

Figure 4.18 shows 3D histogram analyses of the distribution of bubble sizes at several heat fluxes obtained using two distinct processing methods, i.e., the Segmentation via U-Net CNN and the Thresholding technique. For the Segmentation (U-Net CNN) method, we can observe a robust dataset with a wide distribution of bubble sizes across various heat flux values. The histogram shows that at lower heat flux levels, smaller bubble sizes dominate, as indicated by the peak in the lower bubble size region. As the heat flux increases, there is a noticeable shift toward larger bubble sizes. The color gradient suggests a diverse count of bubble sizes, with mid-range sizes being the most prevalent. The U-Net CNN's ability to accurately detect bubbles of varying sizes contributes to the detailed texture of this histogram. On the other hand, the Thresholding technique presents a similar trend with an emphasis on larger bubbles as the heat flux increases. However, the counts for smaller bubble sizes appear reduced compared to the U-Net CNN, possibly indicating the earlier discussed limitation of the thresholding technique in detecting smaller bubbles. Both histograms peak at the higher end

of the heat flux scale, which could correlate to a vigorous boiling phase where large bubbles are more common. The 3D representation of the histograms allows us to see the relation between bubble size and heat flux in a more tangible way, making it easier to perceive trends and variances in the data.

What stands out in these histograms is the relationship between the heat applied and the bubble dynamics within the liquid nitrogen. Smaller bubbles are abundant at lower heat levels but give way to larger ones as the heat flux rises. The U-Net CNN seems to capture a finer granularity of this transition. The progression from a higher count of small to large bubbles could have implications for cooling efficiency and safety in systems that utilize liquid nitrogen. It is a precursor of a transition from nucleate to film boiling, which has different heat transfer characteristics [30]. Identifying this transition is important for the design and control of cooling systems in various industrial processes.

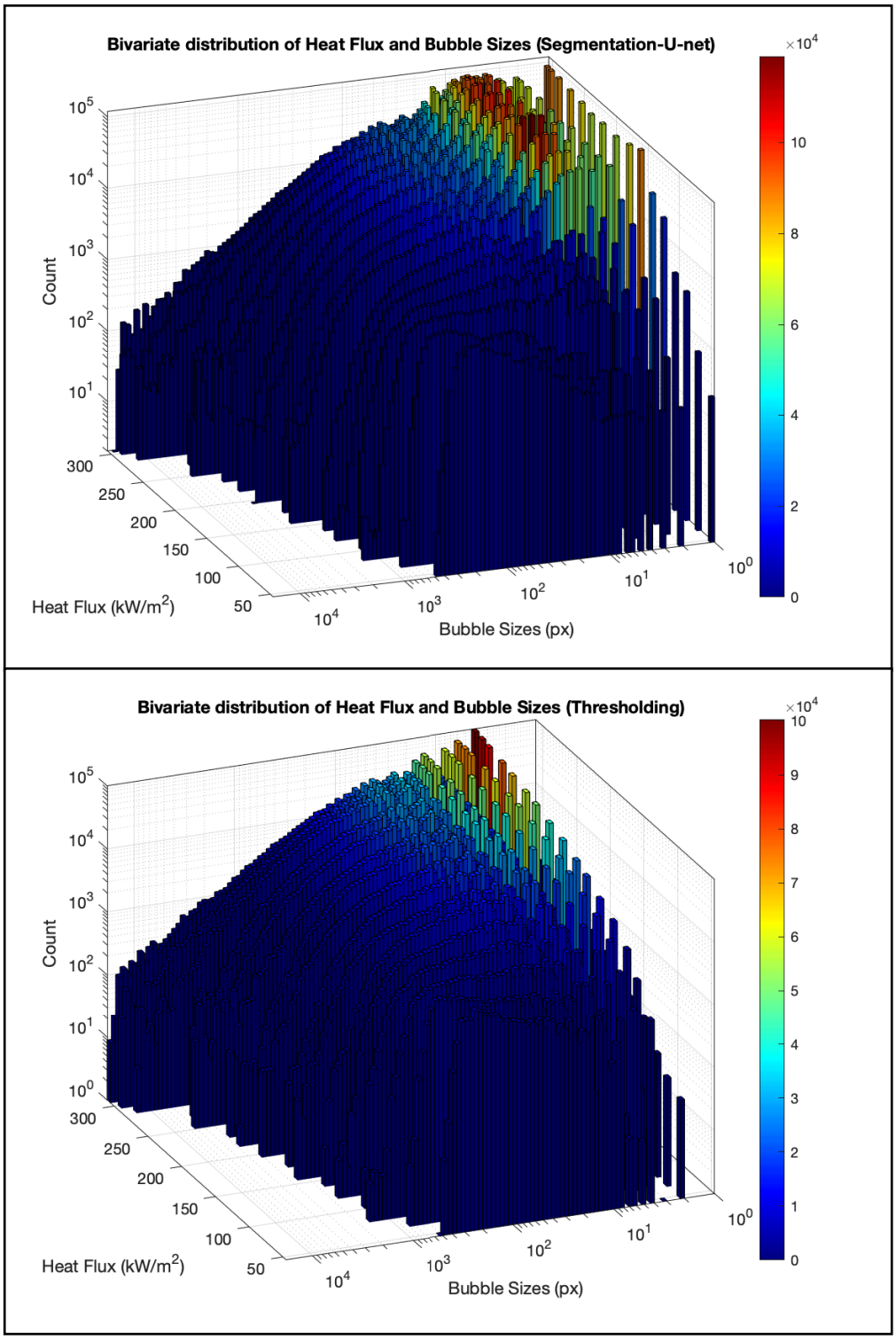

Figure 4.18 3D Histogram of Heat Flux vs. Bubble Sizes Distribution Using Segmentation (U-Net CNN) and Thresholding Technique

4.1.3 Perimeter Visualization

To further understand the reason for the rapid change in the dry area fraction and contact line density as the heat flux increases from video 8-9, Figure 4.19 provides a side-by-side comparison of different bubble detection techniques on raw camera images from two selected video frames from videos 9 and 8. The figure aims to illustrate the effectiveness of U-Net, Thresholding, and a combination of both methods in identifying bubbles in a boiling liquid nitrogen environment.

The top row shows the raw camera images, giving us the unprocessed visual data. These grayscale images capture the bubbles in various sizes and intensities but do not differentiate between bubble boundaries and the liquid background, making it challenging to quantify the boiling characteristics accurately. The second row depicts the results of the U-Net processing, where the detected bubble edges are outlined in red. U-Net demonstrates its precision in identifying bubble contours, even for those that are close to each other or vary significantly in size and shape. This ability to distinguish overlapping and adjacent bubbles is essential for an accurate count and size distribution analysis, which directly feeds into understanding the heat transfer properties of the boiling process. In the third row, we observe the outcomes of the Thresholding technique, with bubble detection highlighted in green. Thresholding offers a stark contrast between bubbles and the background, which can be helpful in quickly identifying areas of high bubble concentration. However, it may not delineate the exact boundaries of each bubble as effectively as U-Net, especially when bubbles are clustered together or when there is a subtle difference in grayscale intensity between the bubble and the background. The fourth row combines U-Net and Thresholding, aiming to leverage the strengths of both. This approach uses the robust boundary detection of U-Net and the clear contrast provided by Thresholding to enhance bubble identification. The combination method appears to capture most of the bubbles identified by both individual methods, with the outlines in yellow suggesting a consensus between the two. This may present a more comprehensive picture of bubble distribution, potentially improving the accuracy of subsequent quantitative analyses.

Comparing video 9 and video 8, we can qualitatively assess the consistency and reliability of each technique across different frames. It seems that the U-Net model provides a

consistent level of detail in both frames, whereas the Thresholding shows some variation, potentially missing smaller bubbles in denser areas. Specifically, in the fourth row where the U-Net + Thresholding is considered, it is observed that there is a prevalence of red (segmented pixels) in video 9 which show that the U-Net picks more smaller bubbles than the thresholding method. This explains why there is an observed rapid change in the contact line density and the dry area fraction as observed in Figure 4.16. This comparative analysis is significant because the chosen detection technique can substantially impact the interpretation of boiling dynamics and the design of related systems. The visualization of the combined U-Net and Thresholding offers a balanced visualization, capturing both the fine details and providing a clear overall picture of bubble activity. Future result would investigate the quantitative differences in bubble size distributions resulting from these techniques to identify the optimal approach for various practical applications.

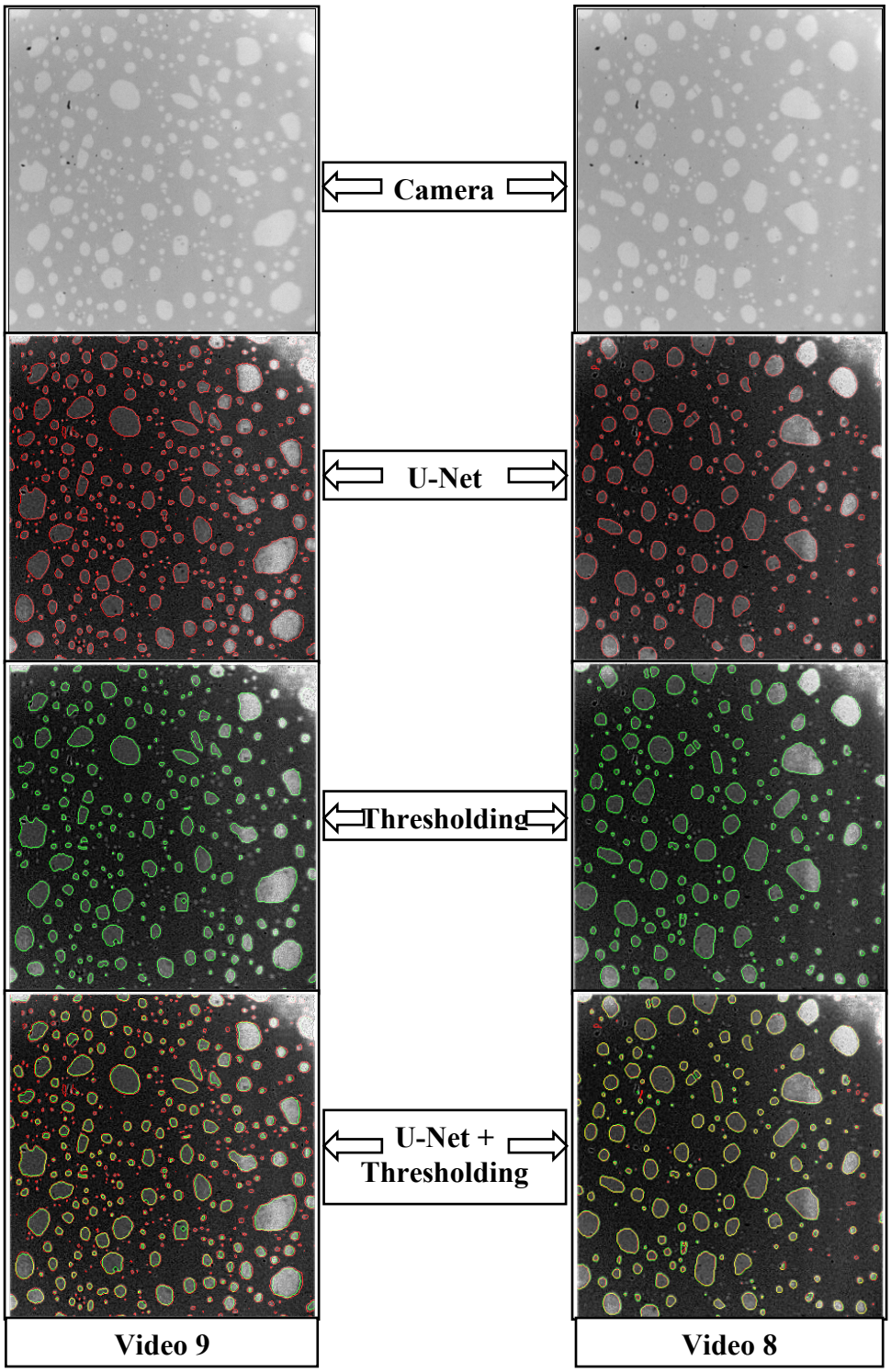

Figure 4.19 Comparative Analysis of Bubble Detection Techniques in Selected Video Frames: Raw Camera Images and Post-Processed Results Using U-Net, Thresholding, and Combined Methods

4.1.4 Bubble Size Distribution

Figure 4.20 showcases a compelling visualization of bubble size distribution in selected frames from videos 8 and 9, contrasting the raw camera output with the results obtained after applying segmentation and thresholding methods.

The first column of the figure displays the raw camera images from video 9 and video 8. These grayscale images provide the untreated visual data, capturing a range of bubbles in various shades of gray, which represent different sizes but do not offer a quantifiable distinction between them. In the middle column, the results of the segmentation method are shown, where the color map is representative of the bubble size group. Smaller bubbles are shaded blue, medium bubbles green, larger ones yellow, and the largest in orange. This color-coding allows for a quick visual assessment of the bubble size distribution. In both frames from videos 9 and 8, the segmentation method illustrates a variety of bubble sizes with a clear predominance of medium to large bubbles, which could indicate vigorous boiling activity. The segmentation appears to delineate each bubble individually, regardless of the proximity to others, highlighting the method's precision in capturing the full spectrum of bubble sizes. The third column presents the results of the thresholding method, which also uses color-coding to differentiate bubble sizes. However, compared to the segmentation output, the thresholding seems to emphasize larger bubbles more prominently, which suggests that while it can identify bubbles effectively, it might overlook smaller ones or merge close-proximity bubbles into larger segments.

Comparing video 9 to video 8, we can infer the consistency and capability of each technique across different frames, which is critical for ensuring reliable analyses across a series of experiments. The segmentation method, with its detailed size categorization, could be essential for precise applications where understanding the full range of bubble dynamics is necessary for optimizing thermal processes. Thresholding, offering a more general view, could be suited for applications where the primary interest is in larger bubbles or where computational resources are limited. Generally, both methods can be combined such that the annotated samples used to finetune the U-Net CNN models can be obtained from the thresholding technique. Thereafter, the first results from the thresholding can be improved upon by humans to manually add smaller features missed by the technique. Subsequently, the

finalized annotated samples can be used to finetune the U-Net CNN model for improved segmentation accuracy. The visualization of bubble size distribution through these methods enhances the qualitative understanding of boiling patterns and can guide quantitative analysis. Future results will seek to combine these methods to other use cases.

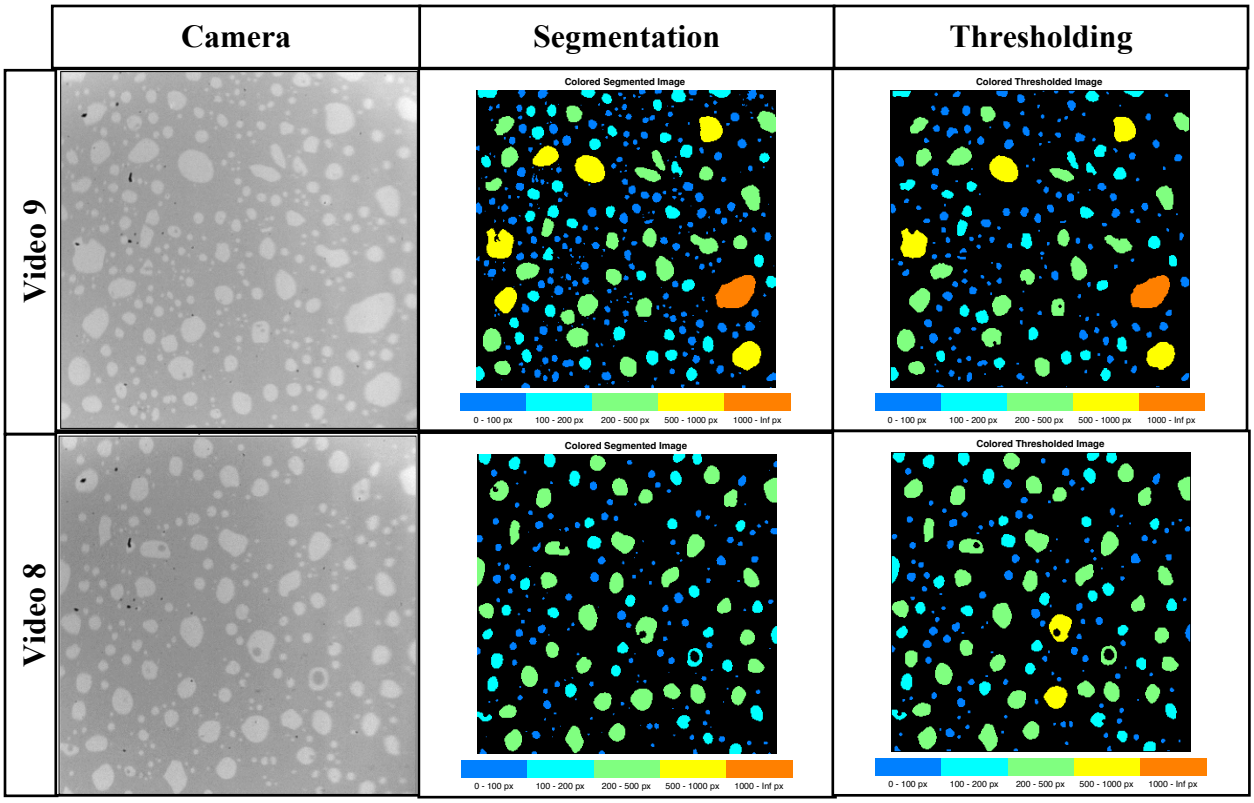

Figure 4.20 Visualization of Colored Bubble Size Distribution in Video 8 & 9 Frames: Raw Camera Output vs. Post-Processing with Segmentation and Thresholding Methods

4.1.4 User Perspective on Ground Truth

The ground truth used to finetune the U-Net CNN and validate the segmentation mask is important as it provides the benchmark for the comparison. Ground truth standardization is an essential step in the segmentation pipeline. To achieve this, we sent the same frames from liquid nitrogen samples to five independent users with boiling image domain expertise. The users annotated the images, separating the bubbles from the background fluid according to their judgment. After that, the masks obtained from this analysis were compared in terms of their dry area fraction and contact line density.

Figure 4.21 compares how different users and image processing techniques measure dry area fraction and contact line density in the same selected frames from videos 8 and 9. This comparison is crucial to understand how subjective human analysis affects the selection of the ground-truth used to evaluate the performance of the computational methods in the context of image processing tasks. The bar chart is divided into two sections, one for each target frame from the two videos. Each section has a set of bars representing the values obtained by the five different users (User 1 to User 5) and two computational methods (Segmentation and Thresholding, the latter done by Chavagnat et al. [28,29]) for the dry area fraction and contact line density measurements. It is noticeable that the values obtained by the five users show a low degree of variation. This spread illustrates the inherent subjectivity and potential inconsistencies in human interpretation, which can arise from individual perceptual differences or varying levels of expertise. However, there is little effect of the user perspective on the contact line density and dry area fraction as all the bars for users 1-5 average around 0.17 for the dry area and 0.05 for the contact line density.

On the other hand, the segmentation method seems to produce a higher value consistently across both videos for dry area fraction. This could imply that segmentation is more sensitive in detecting smaller areas of dryness that the basic thresholding methods might miss. The thresholding method, while objective, may yield lower values compared to segmentation, suggesting it might be less sensitive or it could be more conservative in its estimation, possibly overlooking subtle variations in the image. These results further support the previous findings earlier discussed.

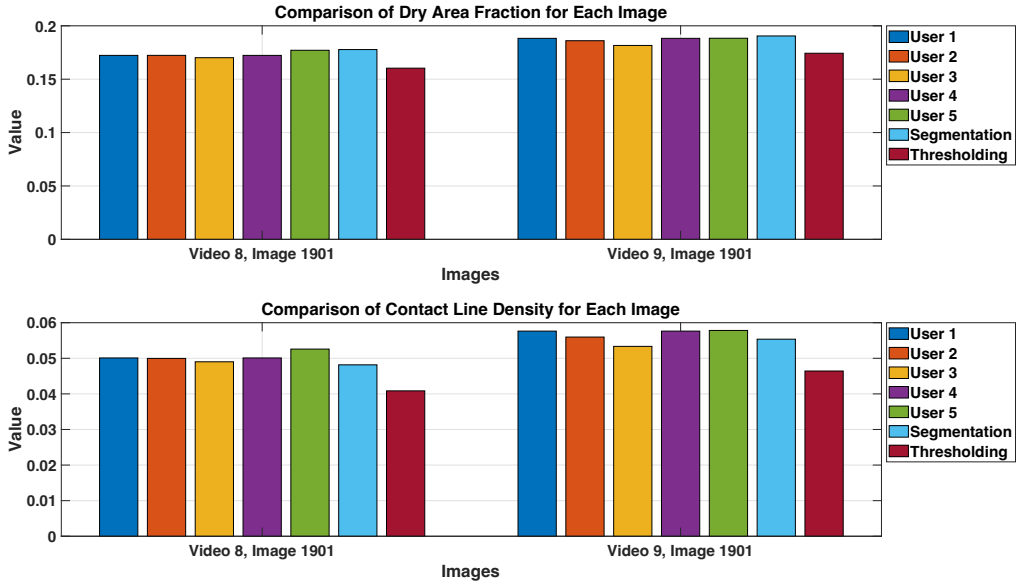

Figure 4.21 Comparison of Dry Area Fraction and Contact Line Density Across Different Analysts and Image Processing Techniques for Target Frames in Videos 8&9.

The percentage difference in dry area fraction and contact line density between the image processing techniques and the ground-truth closes to the camera image is depicted in Figure 4.22. For the selected samples, it is observed that the error by the thresholding method reaches -20% on the contact line and -10% on the dry area for the selected frames. This indicates that thresholding misses certain bubbles which makes it underestimate the contact line and dry area fraction. It is also observed that the segmentation provides a much lower error of less than 2% for the dry area fraction and less than 8% for the contact line density.

To further compare the mean value and standard deviation of the user annotations to the values measured by the algorithms and show that segmentation is within the error bar, we examine results from the contact line in Video 9, Image 1901 which shows the highest discrepancy with the thresholding. The mean of user measurements for the contact line in is 0.05649, with a standard deviation of 0.00171. The segmentation result for the same case is 0.05537, which falls within one standard deviation from the mean of the user measurements. This indicates that the segmentation algorithm performs well and aligns closely with human observers, demonstrating that the segmentation results are within the acceptable range of variation among user annotations. These results quantify the errors in the segmentation and

thresholding methods. Future results will seek to quantify the uncertainties in the actual pixelization in calculating the dry area and the contact line density.

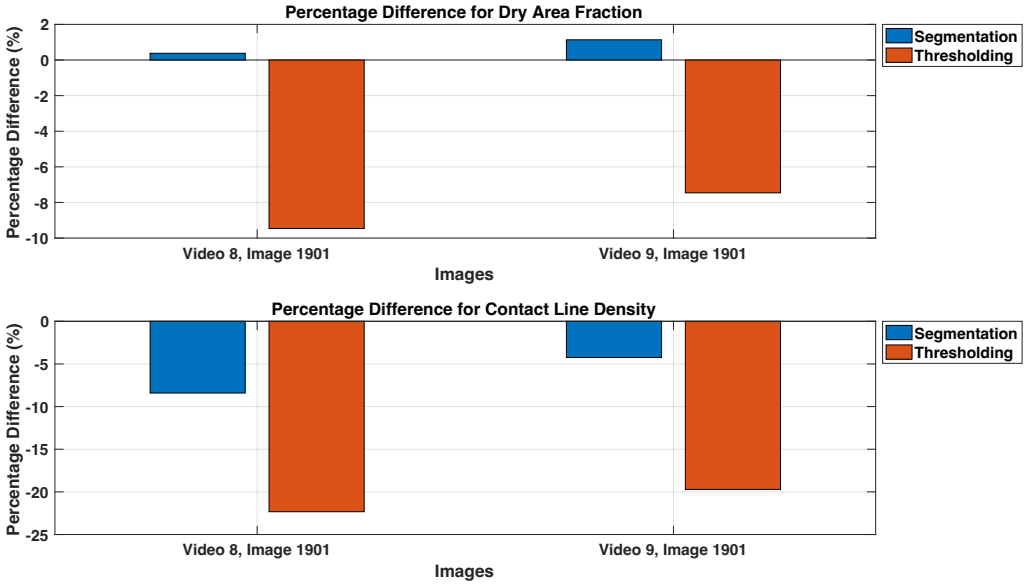

Figure 4.22 Quantitative Comparison of Dry Area Fraction and Contact Line Density Variances: Segmentation vs. Thresholding Techniques Across Images from Videos 8 and 9

4.2 Other Fluids

This section presents the results obtained from estimating the boiling and machine learning metrics of the HSV phase detection images from boiling liquid nitrogen, argon, and FC-72 fluids at constant heat flux conditions using the segmentation method based on U-Net CNN and the binarization method based on thresholding technique. The section starts by showing the perimeter visualization for the different fluids using each method. Thereafter, the results of the quantification of the boiling metrics like the contact line density and the dry area fraction are presented followed by the conventional machine learning metrics ranging from the accuracy to the intersection over union (IoU). Finally, the HSV analysis where the models are deployed to mass-segment numerous frames from the phase detection images are presented

using statistical plots like the probability density function (PDF) and the cumulative distribution function (CDF) plots.

4.2.1 Perimeter Visuals

Figure 4.23 displays the comparative outcomes of the perimeter visualization using U-Net and binarization algorithms against the original camera images for three different fluids: argon, nitrogen, and FC-72. The binarization algorithm was developed by Marco at the MIT Red Lab and it is a variant of the thresholding algorithm involving edge detection and post-processing steps. The perimeters identified by the U-Net algorithm are marked in red, and those identified by the thresholding algorithm are in green. A close examination reveals a resemblance between the bubble patterns in argon and nitrogen, which informed the decision to enhance the U-Net model with mixed data from these two fluids. In contrast, the distinct bubble pattern in FC-72 necessitated the development of a tailored U-Net model for its precise segmentation. As explained in Chapter 3, five annotated images were used to fine-tune the U-Net model. The performance of both the U-Net and binarization methods appears robust for argon and nitrogen, as evidenced by the congruence between the identified perimeters and the raw imagery. This is attributed to the lower incidence of small bubbles in these images, aligning with prior findings where small bubbles were less prevalent. Moreover, such observations are consistent with past studies indicating that threshold-based algorithms rival the performance of U-Net in scenarios with fewer small bubbles. However, the FC-72 images present a different scenario, with a higher presence of small bubbles leading to an increased rate of false positives, particularly noticeable in the top left corner of the thresholding results in Figure 4.8. This disparity may have significant implications for subsequent analyses, including the measurement of contact line density and dry area fraction, which will be further examined in following sections.

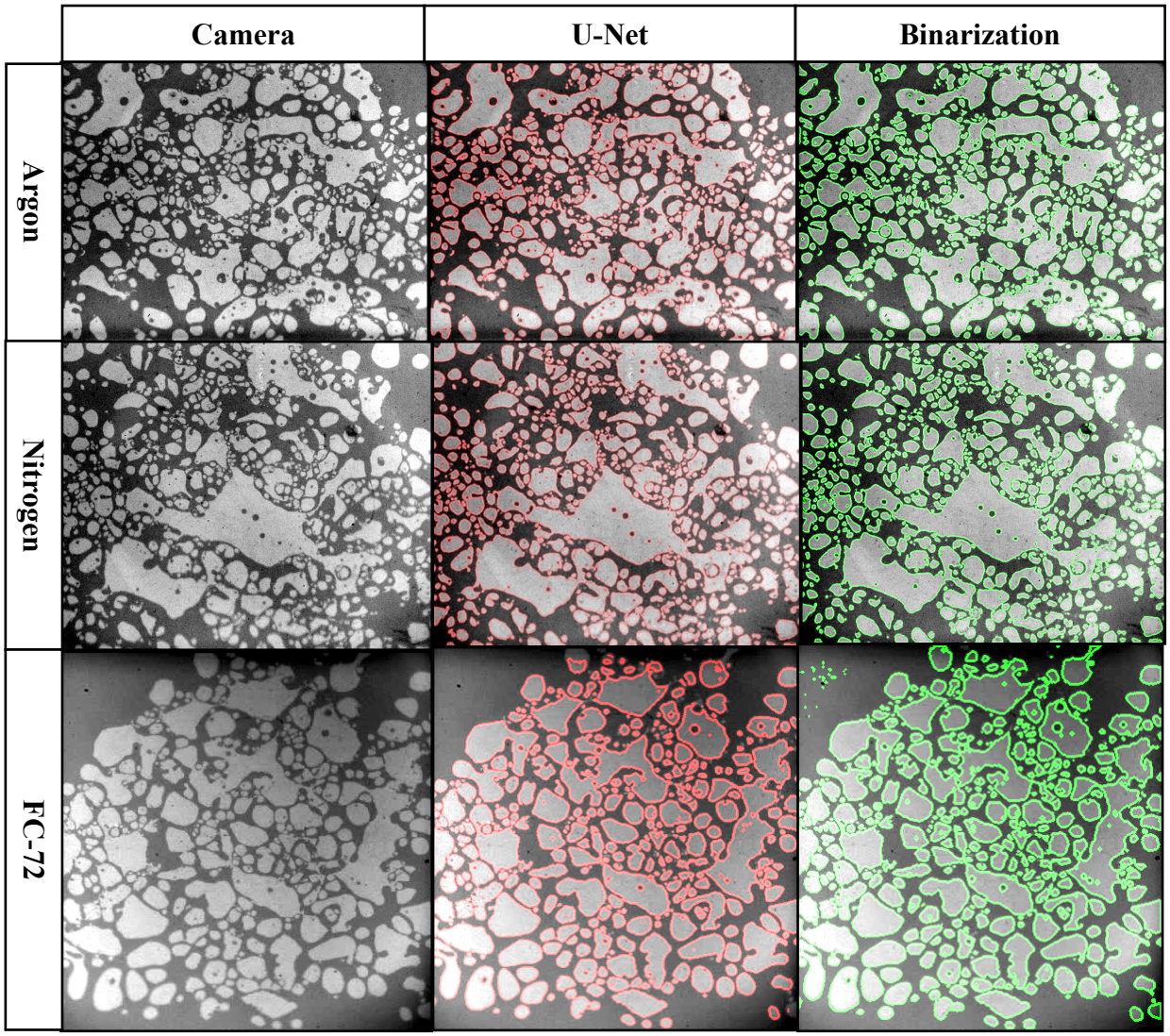

Figure 4.23 Perimeter Visualization in Nitrogen, Argon, and FC-72: Raw Camera Images and Results from U-Net and Binarization Processing

4.2.2 Boiling Metrics

Following the perimeter visualization, the evaluation progressed to quantify key boiling metrics such as the dry area fraction and contact line density. These metrics were calculated for the segmented (U-Net), binarized (adaptive thresholding algorithms), and ground-truth images across six randomly selected samples from the liquid argon (120 kW/m^2), nitrogen (120 kW/m^2), and FC-72 (170 kW/m^2) HSV datasets, representing the full spectrum of the data distribution. To refine the U-Net model, the initial half of these samples were utilized for training and validation, while the latter half served to test the model's ability to generalize to

previously unseen images from the varied fluids. Given the model fine-tuning did not require extensive data and considering the high cost of generating annotated samples, the U-Net CNN model emerged as the most suitable approach for our analysis.

Figure 4.24 details the results of these boiling metric calculations. It is noted that the metrics for argon and nitrogen exhibit similarities in both the dry area fraction and contact line density, which aligns with the analogous bubble distributions noted in the raw camera images. Moreover, the congruence of metrics derived from segmented, binarized, and ground-truth images for these two fluids underscores the efficacy of the segmentation and binarization algorithms when applied to raw camera data. Conversely, in the case of FC-72, there is a notable divergence; while the metrics from the ground-truth and segmented images bear resemblance, the binarized algorithm's results significantly deviate, particularly concerning the elevated contact line density. This deviation is likely a consequence of the greater incidence of false positives associated with the binarization algorithm, which tends to over-respond to the abundance of smaller bubbles present in the FC-72 distribution.

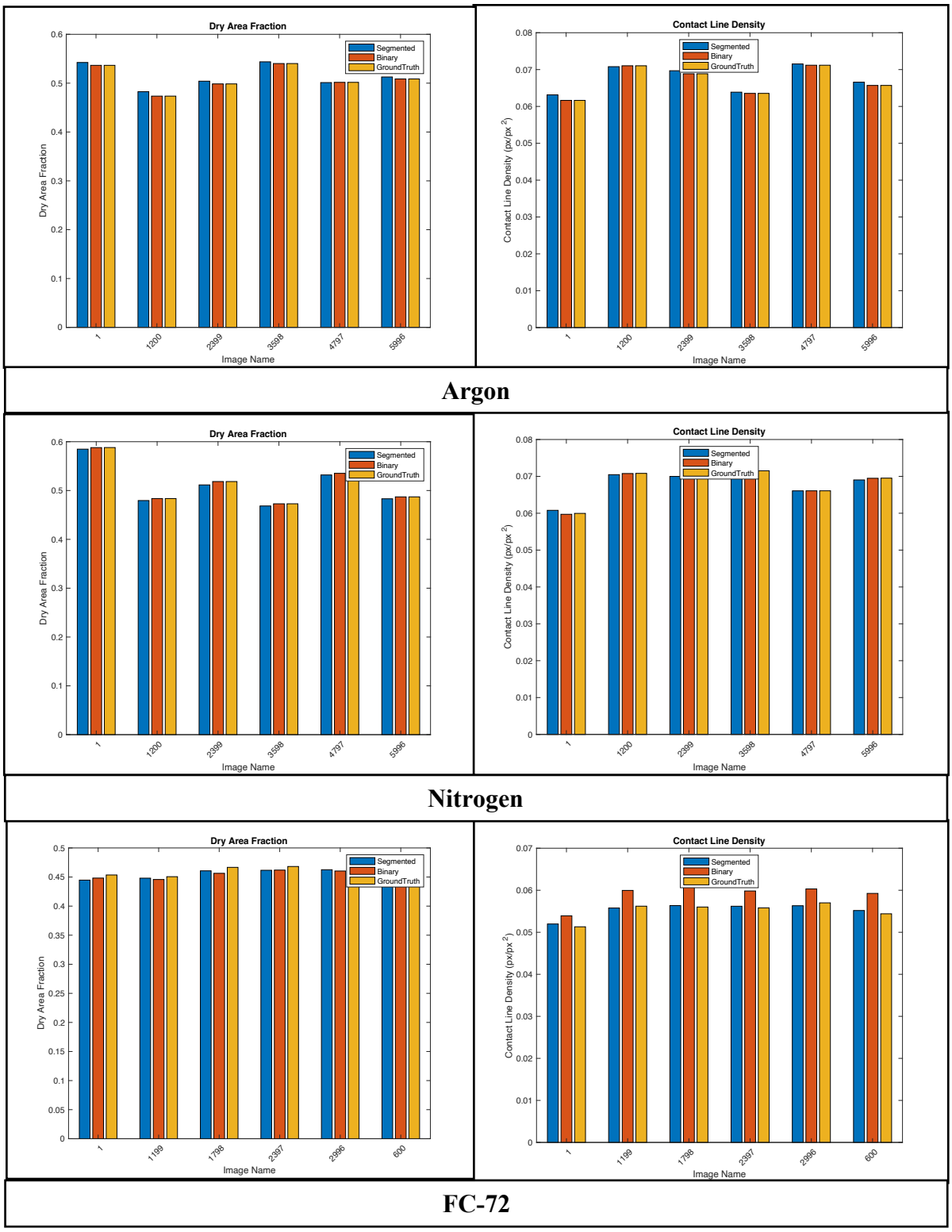

Figure 4.24 Comparative Boiling Metrics of Dry Area Fraction and Contact Line Density in Argon, Nitrogen, and FC-72 Environments: Segmented vs. Ground Truth Analysis

4.2.3 Machine Learning Metrics

After calculating the boiling metrics and establishing the superior performance of the U-Net CNN segmentation, the next step involves quantifying the typical image segmentation performance metrics to further ascertain the quality of the U-Net segmentation. The typical segmentation performance metrics considered range from the accuracy to the intersection over union (IoU), and the Mathew's correlation coefficient (MCC).

The graphs in Figure 4.25 showcase the individual and average values for accuracy, precision, recall, F1-score, IoU, and MCC across images of argon, nitrogen, and FC-72. For argon and nitrogen, the performance metrics exhibit a generally high level of accuracy, precision, and recall, with a notably consistent F1-score, which suggests a balanced segmentation performance between precision and recall. The mean IoU and MCC metrics, while slightly more variable, still maintain high values, indicating a strong overlap between the segmented images and the ground truth. The FC-72 data shows greater variability across the metrics, which might be due to the complexity of bubble segmentation in this fluid as indicated by the presence of smaller bubbles and the subsequent higher false positive rates and negative rates identified previously. Despite the fluctuations, the overall high scores across all metrics indicate that the U-Net CNN segmentation performs robustly, even in more challenging scenarios. On average, across all images and fluids, the scatter plots reveal that the U-Net CNN model maintains a consistently high performance, particularly in terms of accuracy and F1-score. This underpins the model's effectiveness not just in accurately identifying true positives but also in balancing the precision and recall, crucial for reliable segmentation in varied imaging conditions.

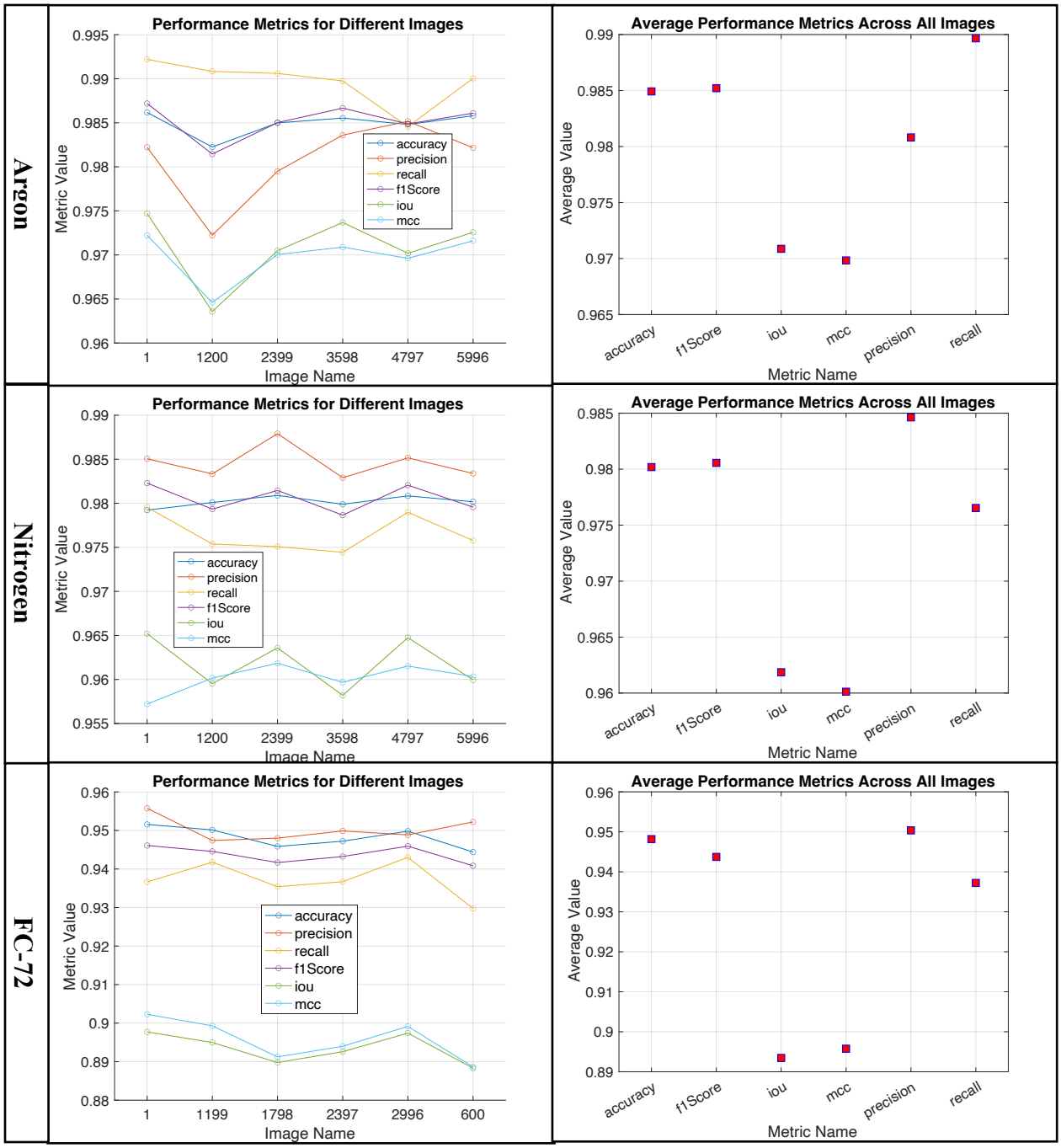

Figure 4.25 Evaluation of Image Segmentation Performance Metrics Across Different Fluids: Detailed and Aggregate Analysis

4.2.4 Statistical Analysis

Upon confirming the satisfactory performance of the U-Net CNN models with the test, training, and validation datasets, these models were applied to process the complete HSV

datasets for argon, nitrogen, and FC-72 fluids. The segmentation outcomes are represented through statistical methods including probability density functions (PDF), cumulative distribution functions (CDF), and box plots, as illustrated in Figure 4.26.

The analysis of PDFs, CDFs, and box plots reveals a degree of consistency between the argon and nitrogen fluids concerning dry area fraction and contact line density metrics. For the nitrogen dataset, the metrics derived from segmentation and binarization algorithms are notably close, with dry area fractions ranging from 0.46 to 0.48 and contact line densities from 0.06 to 0.07. The differences become more apparent in the probability density and cumulative distribution yet remain within a narrow band. In contrast, the argon dataset shows slightly wider variances, with segmented dry area fractions spanning 0.48 to 0.53 and binarization results ranging from 0.51 to 0.56. Observations from the box plots suggest a modest degree of agreement between the mean values of segmented and binarized dry areas, as well as contact line densities, with discrepancies within ±5%.

However, for the FC-72 data, despite some concurrence in the range of values on the x-axis of the PDF and CDF plots, differences in probability densities and cumulative probabilities are evident, particularly for contact line density. This observation aligns with earlier results indicating a tendency for the binarization method to generate a higher number of false positives. The box plots further substantiate this, displaying similar median values but divergent minimum and maximum values for both the contact line and dry area fractions.

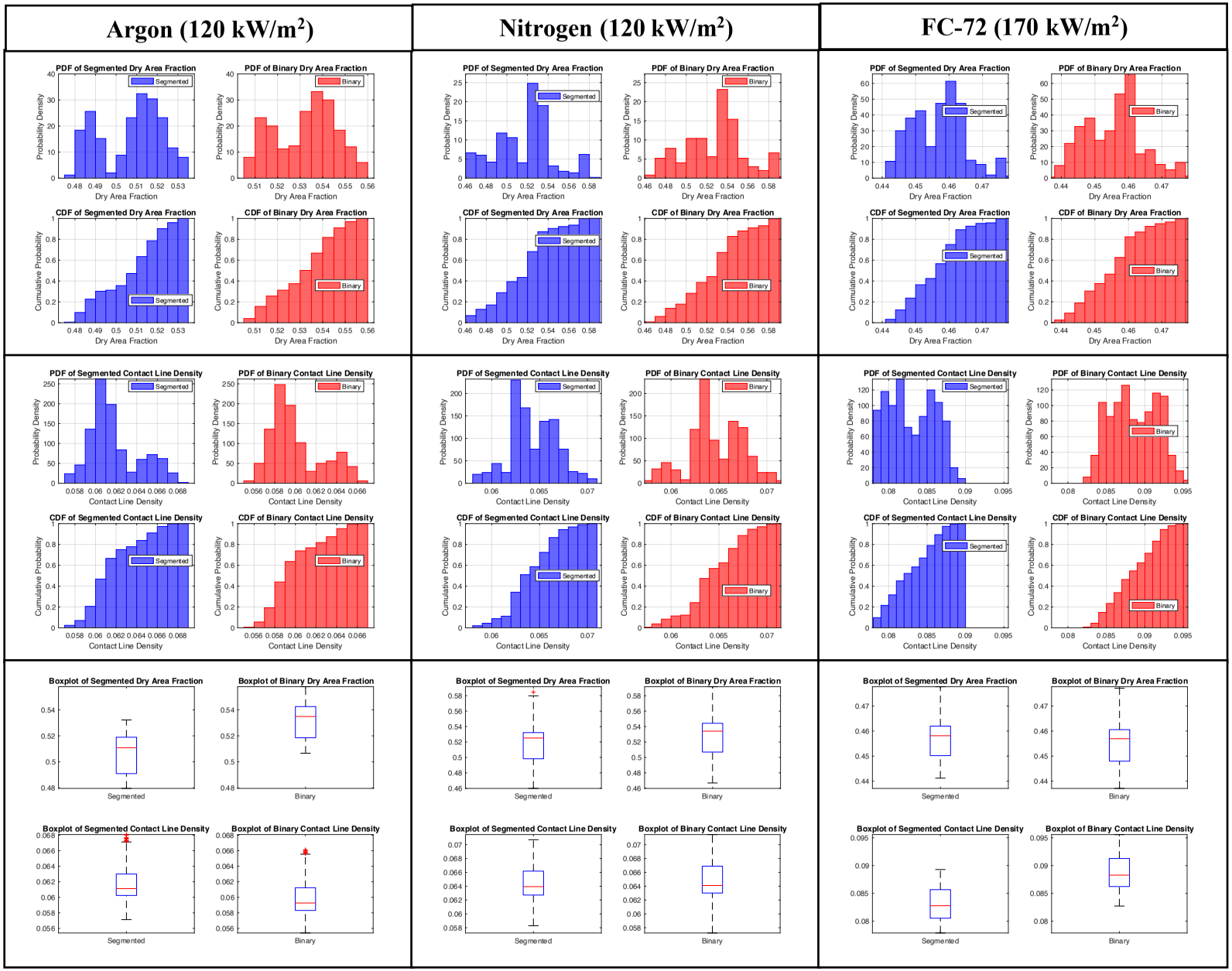

Figure 4.26 Statistical Analysis of Dry Area Fraction and Contact Line Density: Probability and Cumulative Distributions with U-Net Segmentation and Binary Methods

4.3 High Pressure Water

This section explains how we used U-Net CNNs to segment videos of high-pressure flow boiling of water. We looked at two different sets of conditions. In Case 1, the operating conditions were 10 bar pressure and 3000 kW/m^2 heat flux. For Case 2, the conditions were a pressure of 40 bar and a heat flux of 3400 kW/m^2. Both cases were obtained from the same imaging setup; however, the cropping of the images are different due to the nature of the images. The cropping is done to extract only the clear parts of the images not covered by noise. We can see from the camera images, in Figure 4.27, that the two cases have different numbers and sizes of bubbles, with Case 2 showing more bubbles due to its higher pressure and heat flux conditions.

After preparing the data, we used U-Net CNN models that were originally made for liquid nitrogen to segment the high-pressure water videos. The results are shown in Figure 4.28. The model, which was trained on different data, did not segment the high-pressure water videos perfectly. It was better at identifying smaller bubbles than larger ones. For larger bubbles, the model sometimes missed the center, creating a hole in the middle of bubbles. This issue, along with some incorrect bubble identifications (false positives), suggests the model's training didn't include enough high-pressure water boiling features.

Despite these issues, the initial segmentation results are useful. They provide a starting point to create training data for improving the model. We do this by taking the bubble outlines from the initial segmentation and manually correcting them on the images. We use five samples of the annotated images to finetune the U-Net model. This shows how we can use the model trained on different data as a starting point to get good results on new types of data eventually.

After we improved the U-Net CNN model, we compared its perimeter results with the original images that experts had carefully checked (ground-truth). These comparisons are shown in Figure 4.28. The updated U-Net model does a good job of finding and outlining the bubbles in the videos, almost as well as the expert-prepared images. We also put the outlines from the U-Net model and the expert images together in one picture, using a yellow line to show where they overlap (where the model's green and the experts' red outlines mix).

Even though the U-Net model works well on these images, when we look closely at the combined picture, we notice some small differences. A few very tiny bubbles marked by the experts are missing in the U-Net's outlines. Next, we'll measure how well the U-Net model, and the expert images match up, looking at different aspects of boiling across several video frames.

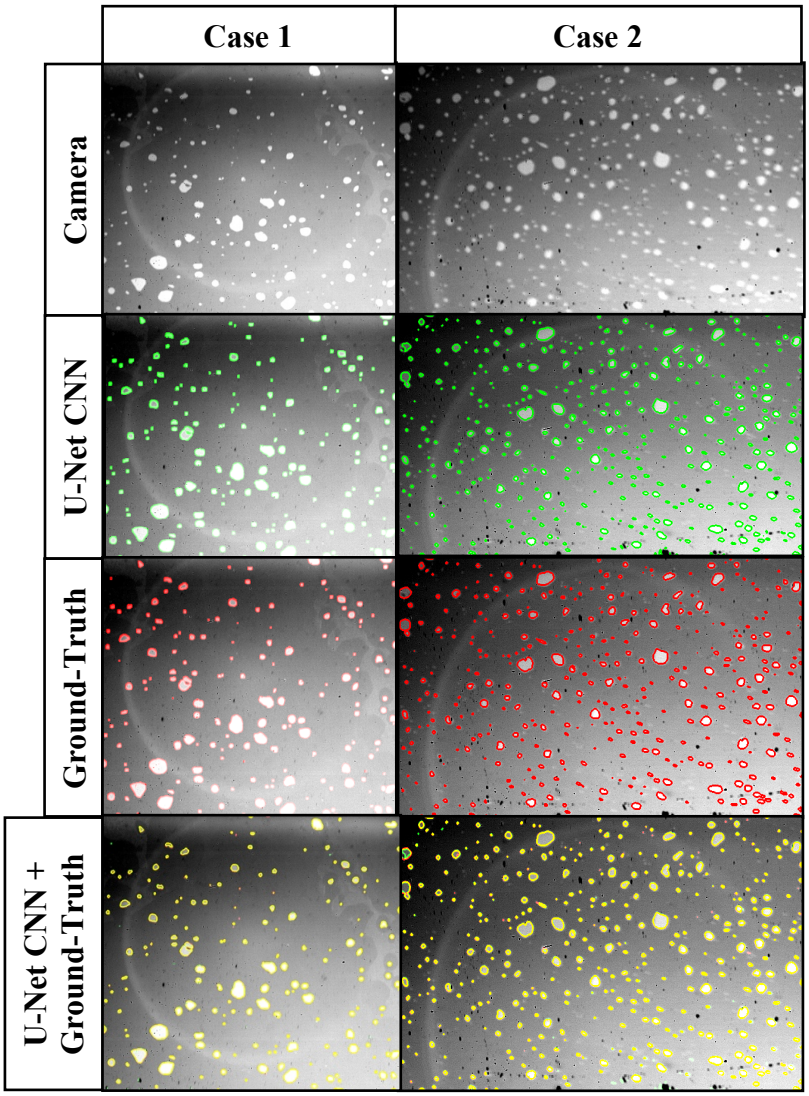

Figure 4.27 Bubble Edges Visualization: Raw Camera Capture, Ground-Truth, Segmentation and Combined Overlay

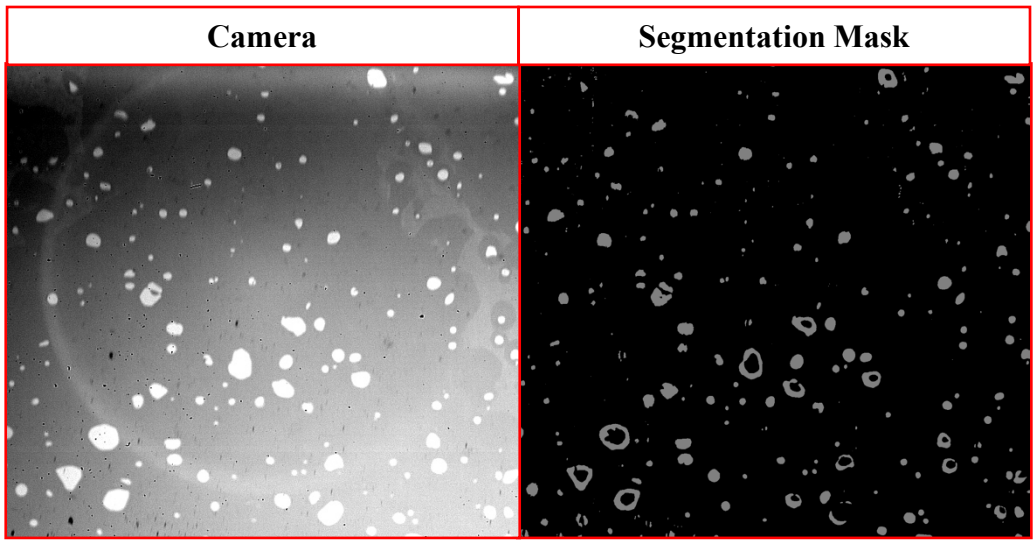

Figure 4.28 Comparison Between High-Pressure Water Camera Image and Segmentation Mask Obtained from Previous U-Net CNN Trained on Liquid Nitrogen Data

Figure 4.29 shows how the contact line density and dry area fraction differ across various frames in the two high-pressure water experiments (Cases 1 and 2). We also provide plots that measure the errors by showing the absolute difference (segmentation - ground truth) and the percentage difference ((segmentation - ground truth) / ground truth) * 100) between the U-Net's segmentation and the expert-checked ground truth.

For this comparison, the first five frames of the video were used to train and check the U-Net model, and the last five frames were used to test it. This ensures that the model is learning the general pattern of bubble distribution, not just memorizing specific frames. We noticed differences in the dry area fraction and contact line density between Cases 1 and 2, which highlights the variability in the experimental conditions.

When comparing the segmentation from the U-Net model to the ground-truth images across both cases, the results are quite similar. However, when we look closer at the plots, the data from the ground-truth images are slightly higher than the segmentation results. This difference likely comes from the segmentation model missing a few bubble pixels, which is a common challenge since no model is perfectly accurate.

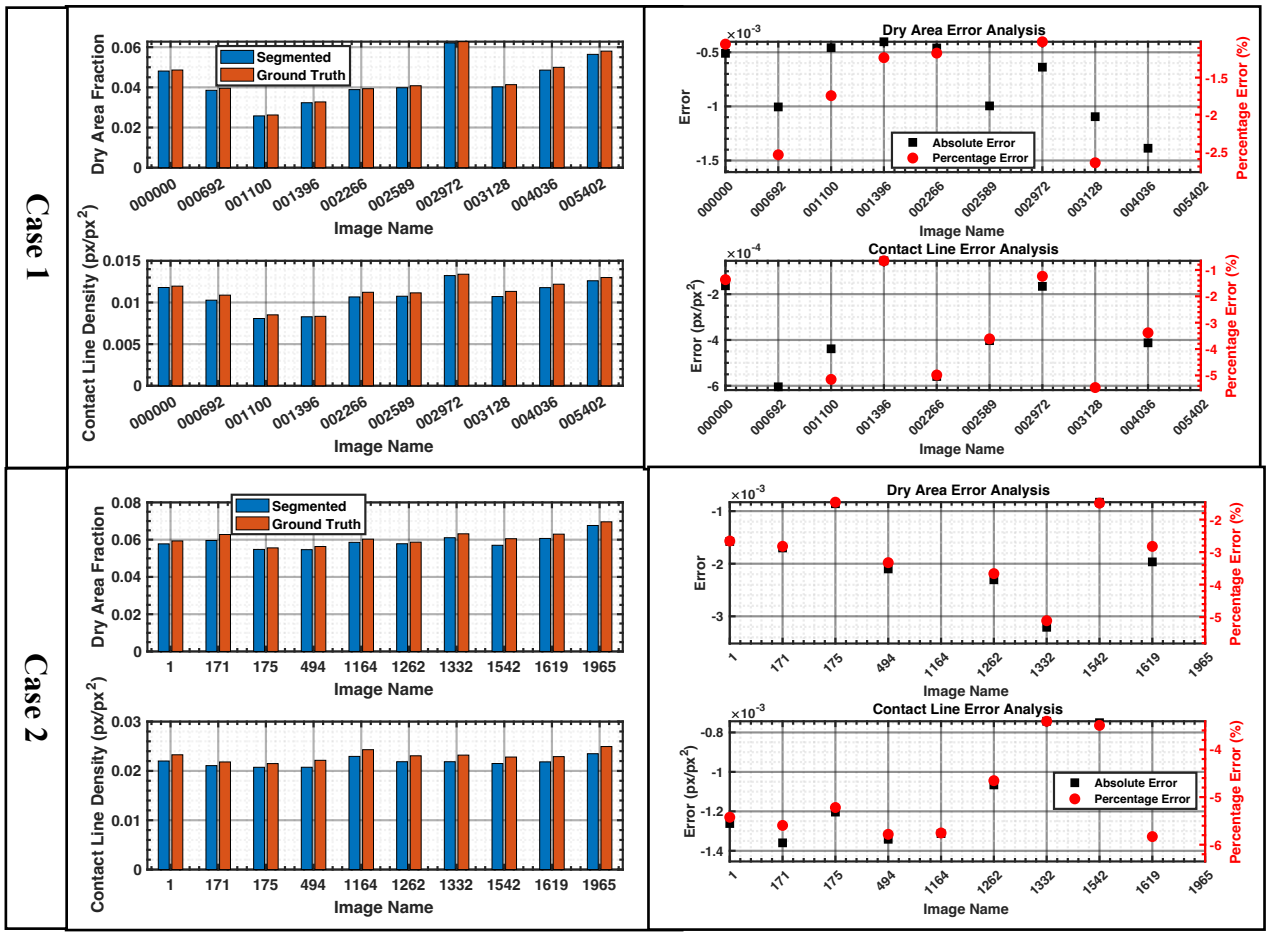

Figure 4.29 Boiling Dynamics Performance Metrics and Error Quantification for Diverse Frames in the High-Pressure Water Videos.

The error quantification plots reveal how the absolute and percentage errors evolve across the video frames for Cases 1 and 2. Notably, all errors recorded are negative, indicating missed pixels during the segmentation process. Across all frames, the dry area errors are generally in the range of 10^{-3}, suggesting a close match between the segmentation outputs and the ground truth. The smallest observed absolute error is 10^{-4} px/px^2 in the contact line measurements for both cases.

However, when looking at the percentage errors, the maximum errors recorded are between 5-6% on the contact line in certain frames for both cases. Figure 4.30 further details these errors through statistical analysis, including the mean, maximum, minimum, and standard deviations. The plot shows the standard deviation with a black line at the center of each bar, with the ends of the line marking the minimum and maximum error values. The green

bars represent the magnitude of the absolute/percentage relative errors on either the contact line or the dry area.

For the dry area fraction, the average percentage errors are 2% for Case 1 and 3.5% for Case 2. Case 1 displays a wider spread of errors (higher standard deviation), indicating more variability in errors across frames. Conversely, the average percentage error for contact line density is 3.5% for Case 1, which also has a higher variability in errors. Case 2 shows a slightly higher mean error of 5% but with less variability, as indicated by a lower standard deviation.

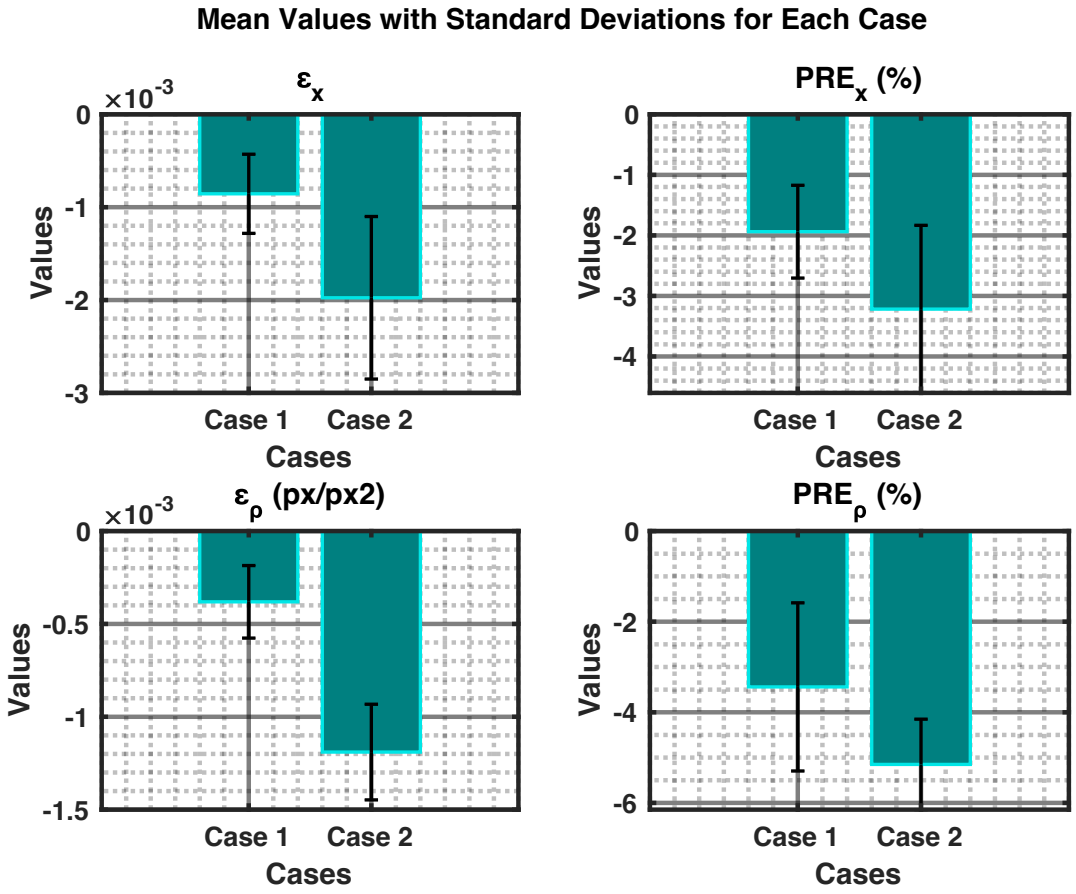

Figure 4.30 Statistical Analysis of the Absolute Error (ε) and Percentage Relative Error (PRE) on the Dry Area Fraction (x) and Contact Line Density (ρ) for Various Cases.

In this final part of our analysis, we shift focus from boiling performance metrics to standard image classification metrics such as accuracy, specificity, precision, F1 score, MCC,

recall, and the IoU. The comparative results for Cases 1 and 2 are detailed in **Error! Reference source not found.**.

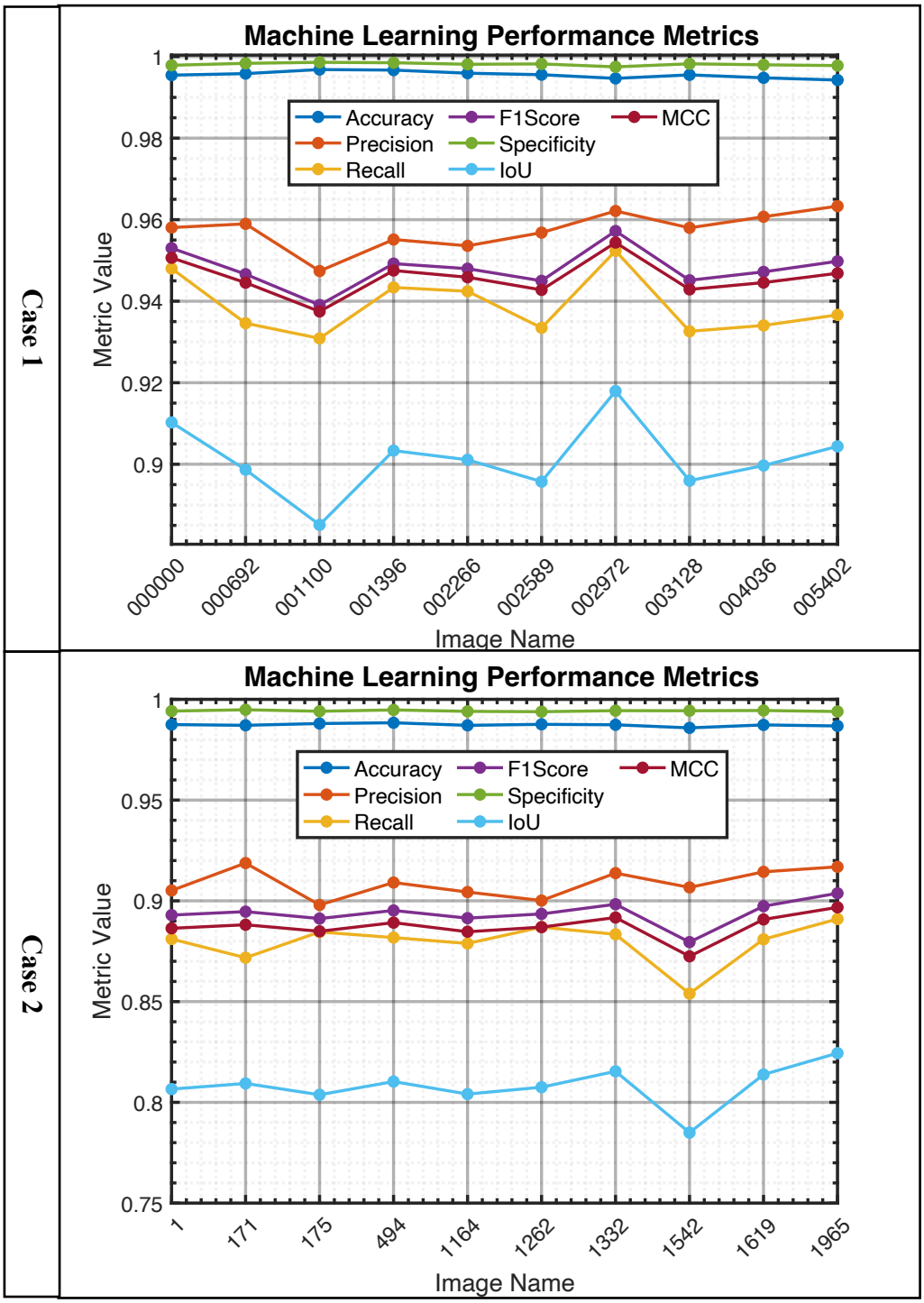

Figure 4.31 Machine Learning Performance Metrics for the Various High-Pressure Water Cases

The analysis reveals exceptionally high specificity and accuracy rates, exceeding 99% for both cases across multiple frames. This high performance indicates that our segmentation model is very effective at correctly identifying true negatives (areas without bubbles) and true positives (areas with bubbles), thus making accurate predictions in most cases.

However, when we examine other metrics like precision, F1 score, MCC, and recall, we notice a slight dip in performance. For Case 1, these metrics hover around 95%, while for Case 2, they range between 87-90%. The precision metric, which evaluates the model's ability to identify only relevant objects as positives, along with recall, which assesses the model's success in identifying all actual positives, slightly decrease. This discrepancy can be attributed to a few factors:

1. **Variability in Experimental Conditions**: Case 2's more challenging conditions might have introduced more complexity in the segmentation task, affecting these metrics.
2. **Model Sensitivity**: The segmentation model may be slightly less sensitive to identifying all true positives in the more complex scenarios of Case 2, affecting recall and consequently precision and F1 scores.

The IoU metric, known for its comprehensive evaluation of segmentation accuracy by considering both true positive and false positive rates, shows the lowest values among the metrics: 90% for Case 1 and 80% for Case 2. These lower IoU values, compared to other metrics, are expected because IoU provides a more stringent assessment by simultaneously considering the area of overlap and the area of union between the predicted and actual segmentations. The lower IoU for Case 2 can be specifically attributed to the increased experimental complexity, leading to more segmentation challenges and hence a slightly reduced overlap accuracy.

Although the segmentation model demonstrates exceptional specificity and accuracy, we observe a modest decline in precision, F1 score, Matthew's Correlation Coefficient (MCC), recall, and notably the Intersection over Union (IoU) for Case 2. This reduction emphasizes how the complexity of experimental conditions can present additional challenges for segmentation accuracy. Consequently, the forthcoming section of this thesis will delve into

the issue of discretization error, which arises during the pixelation of bubbles. This is a crucial step in computing performance metrics such as contact line density and dry area fraction from the experimental data.

Chapter 5

Uncertainty Quantification

This section examines how uncertainties in discretizing binarized bubbles may impact the measurement of boiling parameters, such as the dry area fraction and contact line densities, during post-processing. To address this, we conducted numerical experiments to explore the influence of grid resolution and bubble size (represented by the bubble's radius) on the measurement of bubble perimeter and area. These parameters are crucial for calculating the dry area fraction (the ratio of the area covered by bubbles to the total area) and contact line density (the ratio of the total bubbles' perimeter to the total area).

As a reference point, we consider a theoretical circular bubble. We calculate its perimeter and area as functions of the bubble's radius. These theoretical values are then compared with the discretized values of perimeter and area, which depend on both the bubble's radius and the grid cell size. To quantify the discrepancies, we introduce two error metrics: the Percentage Relative Error (PRE) and the Mean Error (ME), defined mathematically by Equations (5.1) and (5.2) respectively:

$$PRE = \frac{\psi_{theo} - \bar{\psi}_{disc}}{\psi_{theo}} \times 100 \tag{5.1}$$

$$ME = (\psi_{theo} - \bar{\psi}_{disc}) \tag{5.2}$$

Here, the subscript "disc" denotes discretized values, and "theo" refers to theoretical values, i.e., $2\pi R$ for the perimeter and $2\pi R^2$ for the area, where R is the bubble radius. The symbol ψ represents the computed values, which is unique, where $\bar{\psi}$ denotes the mean value measured in the numerical experiment.

The initial phase of this study involved deriving key parameters such as the bubble's radius, perimeter, and area from a representative experiment showcasing a range of bubble sizes. For this purpose, we chose a specific frame from the liquid argon experimental data, collected through HSV at a resolution of 12.6 μ/px during saturated pool boiling experiments. These experiments were conducted under conditions of 1 bar pressure, a heat flux of 120

kW/m^2, and a wall superheat of 9.5 K. The images were processed to differentiate between the liquid background and the bubbles (0 representing the liquid and 1 for the bubbles) using U-Net CNN models. The processed, or segmented, image is illustrated in Figure 5.32. Following segmentation, we computed and then plotted the bubbles area, perimeter, and radius distributions. The radius is calculated as the radius of the circle with the same area. This calculated radius values are then used to define the radii range in conducting the error analysis (developing the error surface plots). These were reported through both logarithmic and linear representations to offer a comprehensive view.

The histogram plotting the perimeter on a linear scale reveals a higher probability density for smaller perimeters, with a notable decrease for larger sizes. This pattern suggests a predominance of smaller bubbles, alongside a swift decrease in larger bubble occurrences. In contrast, when displayed on a logarithmic scale, the tail of the distribution is elongated, unveiling the existence of larger perimeters that seem less significant on the linear scale. This logarithmic representation facilitates a clearer view of the distribution's shape. However, it still highlights a skew towards smaller perimeters over a wide range.

Similarly, for bubble areas, the linear scale histogram shows a pronounced density for smaller areas, diminishing as the area increases. The logarithmic scale once again brings to light the larger areas, indicating that, despite the dominance of smaller bubbles, larger bubbles are also notably present. This distribution pattern on both scales suggests a general trend of bubbles occupying smaller areas, with a gradual decrease in frequency as the area increases.

Regarding the radius, the linear scale histogram illustrates a distribution that leans towards lower radii, confirming that smaller bubbles are more frequently observed. The decreasing probability density for larger radii points to a scarcity of large bubbles. However, the logarithmic scale portrays a more evenly spread distribution across various bubble sizes, hinting at a diverse array of bubble dynamics. This diversity could reflect different phenomena affecting bubble formation and stability, like coalescence or fragmentation. The observed prevalence of smaller bubbles might be attributed to high nucleation rates or the splitting of larger bubbles, while the occasional larger bubbles could result from processes like coalescence or slower growth dynamics.

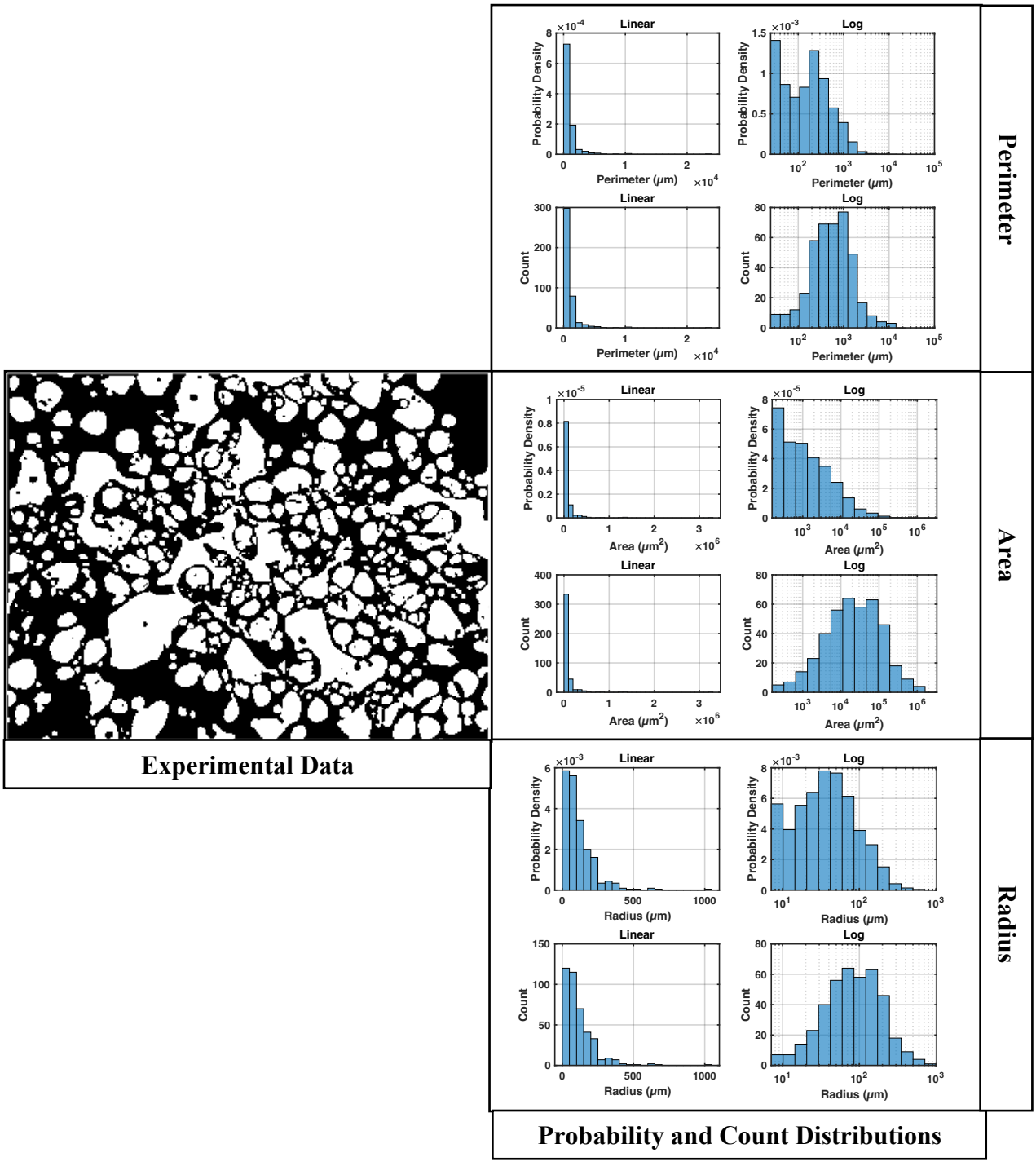

Figure 5.32 Probability and Count Distributions of the Perimeter, Area, and Radius Distributions of a Segmented Experimental Data (Liquid argon @ 1 bar, 120 kW/m^2, 9.5 K)

Following the determination of bubble parameters from the experimental data, we conducted a discretization error analysis. This analysis was based on a domain of 0.001m (L) with varying grid cell sizes (N) from 5-50 microns and bubble radii (R) from 0-200 microns. This radii range selected aligns with the observation in Figure 5.32 where a higher bubble count and probability density is observed in this range. In the simulation, we randomly placed a bubble within the domain L and computed the discretized area and perimeter values for each N and R pairing.

Figure 5.33 illustrates the convergence behavior of the simulation through the PRE of both the perimeter and area as a function of iteration count. The convergence test is conducted at four different iteration milestones: 5,000 (5K), 10,000 (10K), 15,000 (15K), and 20,000 (20K) iterations.

Observing the plots, we notice that the perimeter PRE (in black) and area PRE (in red) exhibit distinct patterns as iterations progress:

1. **5K Iterations:** The perimeter PRE fluctuates within a tight range, suggesting relative stability. In contrast, the area PRE displays more significant fluctuations. This disparity implies that while the estimation of the perimeter has reached a quasi-stable state by 5,000 iterations, the area calculation is subject to higher variability at this stage.
2. **10K Iterations:** With doubled iteration count, both the perimeter and area PREs demonstrate reduced fluctuations. This reduction in variability is indicative of increasing stability in the simulation's numerical solution as it converges towards the true values.
3. **15K Iterations:** As iterations increase further, the fluctuations in both perimeter and area PRE continue to decrease. The convergence appears to be improving, as evidenced by the tighter oscillation amplitude, especially for the area PRE, which is now closer to zero percent error.
4. **20K Iterations:** At the final milestone, the simulation shows further stabilization with even smaller oscillations in PRE for both the perimeter and area. The area PRE, in particular, seems to have reached a level of minimal variability, oscillating very close to zero, indicating strong convergence.

Overall, the results suggest that as the number of iterations increases, the simulation becomes more stable, evidenced by the decreasing amplitude of the PRE for both the perimeter and area. This trend is consistent with the expected behavior of a converging numerical solution, where increased iterations generally lead to reduced errors as the solution approaches the theoretical model. It's noteworthy that the perimeter converges more rapidly than the area, which could be attributed to the inherent differences in sensitivity to discretization between linear (perimeter) and areal measurements. Therefore, 20 K iterations are selected for the simulation resulting in a total run time of 987.74 seconds (16.46 minutes).

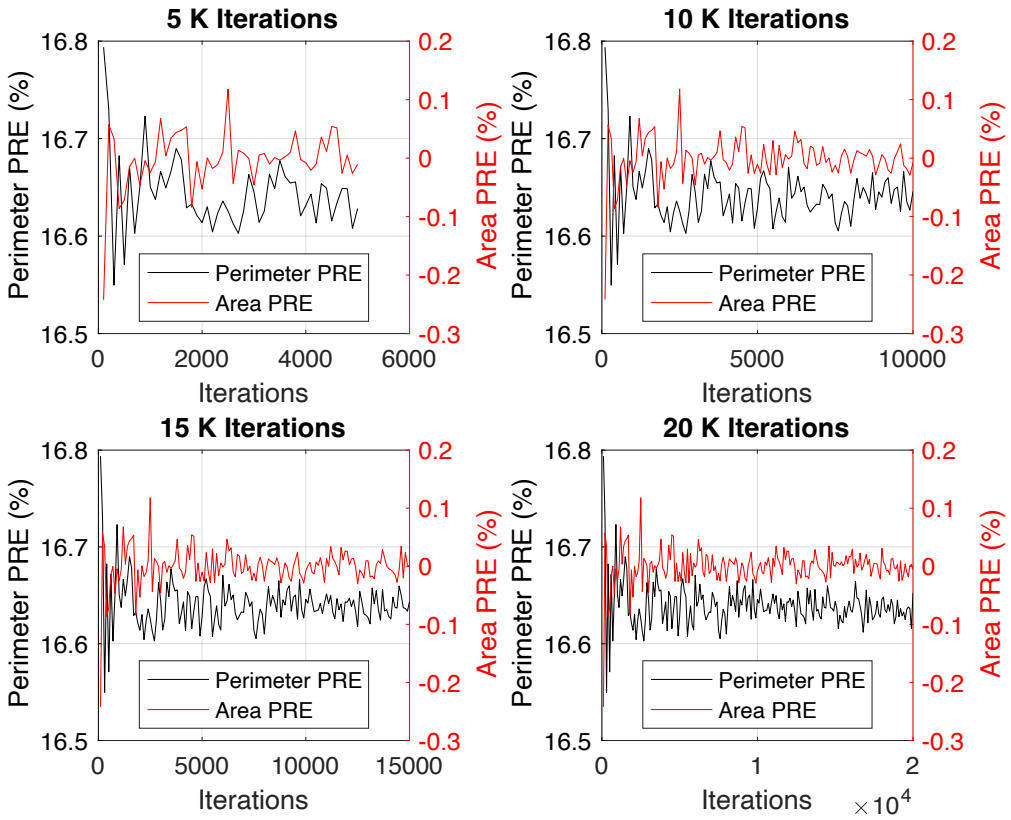

Figure 5.33 Convergence Test Results

The visual investigation of the three-dimensional effects of the bubble radii and the grid cell size on the ME and PRE for the perimeter and area measurements are reported under dilation conditions of the bubble's boundary. Thereafter, the effects of dilation and erosion on

the uncertainty estimation are quantified. This analysis provides information on the effects of the bubble radii and the grid cell size on the error metrics.

Figure 5.34 depicts the mean error and percentage error plots for bubble perimeter and area as functions of bubble radius and grid cell size. The plots reveal key trends in measurement accuracy, which are indicative of the challenges associated with digital image analysis, particularly in the context of bubble characterization. In the ME plot for the perimeter, we observe a distinctive valley-shaped trend. The error is distributed symmetrically around a central point, with negative errors (overestimation of perimeter) at lower grid cell sizes transitioning to positive errors (underestimation of perimeter) at larger grid cell sizes. Interestingly, the error magnitude increases with both decreasing and increasing bubble radius, suggesting an optimal range of bubble sizes for which the perimeter estimation is most accurate. This behavior can be attributed to the digital discretization of the bubble edges: finer grids resolve the edge more accurately, leading to smaller errors, whereas coarser grids tend to either omit boundary pixels or include additional pixels, resulting in under- or overestimation.

Furthermore, the ME plot for the area shows a complex landscape. The errors vary drastically with grid cell size and bubble radius, indicating non-linear and non-monotonic relationships. The transition from negative to positive error may be more abrupt for area measurements compared to perimeter measurements due to the squared nature of area calculation, which amplifies the effect of each miscounted pixel.

The magnitude of errors for the area is notably lower than for the perimeter, which is evident from the different scales of the ME used in the plots. This discrepancy could arise because the perimeter is more sensitive to grid resolution given that it is a linear measure directly affected by the grid boundary, whereas area is a bulk measure and may be less affected by the periphery pixels. Both plots exhibit a decrease in error magnitude as the bubble radius increases, up to a certain point, beyond which the error begins to increase again. This trend suggests that there is an intermediate bubble size where the measurement method achieves optimal accuracy. For very small or very large bubbles, the ME increases, highlighting the limitations of the grid-based measurement approach for objects that are much smaller or larger than the grid resolution.

Furthermore, the PRE plots for the perimeter and area which provide insightful observations into the fidelity of discretized measurements against theoretical expectations as a function of bubble radius and grid cell size. In the PRE plot for the perimeter, the plot reveals a divergence of errors: negative PRE values at smaller bubble radii transitioning to positive PRE values at larger radii. Given the definition of the PRE, negative values indicate an overestimation of the perimeter, while positive values indicate underestimation. The negative PRE for finer grid sizes suggests that the discretization process is adding excess perimeter length for smaller bubbles, possibly due to the inclusion of diagonal pixels that are not part of the actual perimeter. As the grid becomes coarser, the perimeter is underestimated, likely because the increased cell size fails to capture the curvature of the bubbles, leading to a simplified, stepped approximation of the boundary.

For larger bubbles, the positive PRE values across grid cell sizes could be attributed to the increasing influence of curvature. A larger bubble has a perimeter that is less affected by the inclusion of individual diagonal pixels, and the curvature is underestimated by the stair-stepping effect [1], resulting in a shorter perimeter measurement than the actual smooth curve. The transition from overestimation to underestimation with increasing bubble size suggests a non-linear relationship between the measurement error and the object's size relative to the pixel resolution.

The PRE plot for the area shows a different trend. The errors are generally smaller in magnitude, which is expected since area measurements are less sensitive to the pixelation effect along the object's boundary compared to perimeter measurements. Negative PRE values across most of the plot indicate a consistent overestimation of the area for all grid sizes and bubble radii, except for a few instances where it dips into positive values at larger bubble radii and coarser grid sizes. This might occur because of the area calculation being more resilient to the loss of edge pixels, with overestimation prevailing due to the inclusion of partial pixels.

[1] When a curved edge, such as the perimeter of a bubble, is mapped onto a grid with a resolution that is too low to capture the curve smoothly, the result is a jagged or stepped boundary that resembles a staircase, hence the term "stair-stepping". This effect leads to inaccuracies in the measurement of the perimeter because the pixelated boundary can either extend beyond the true boundary (overestimation) or fall short of it (underestimation), depending on the grid cell size relative to the curvature of the object.

Furthermore, the area plot does not exhibit the same clear transition from negative to positive PRE with increasing bubble size as seen in the perimeter plot. This could imply that the method of area calculation is less affected by the grid size relative to the bubble size, maintaining a consistent pattern of overestimation. However, the slight increase in positive PRE at larger bubble sizes and coarser grids might suggest a threshold where the pixelation effect becomes significant enough to lead to underestimation of the area.

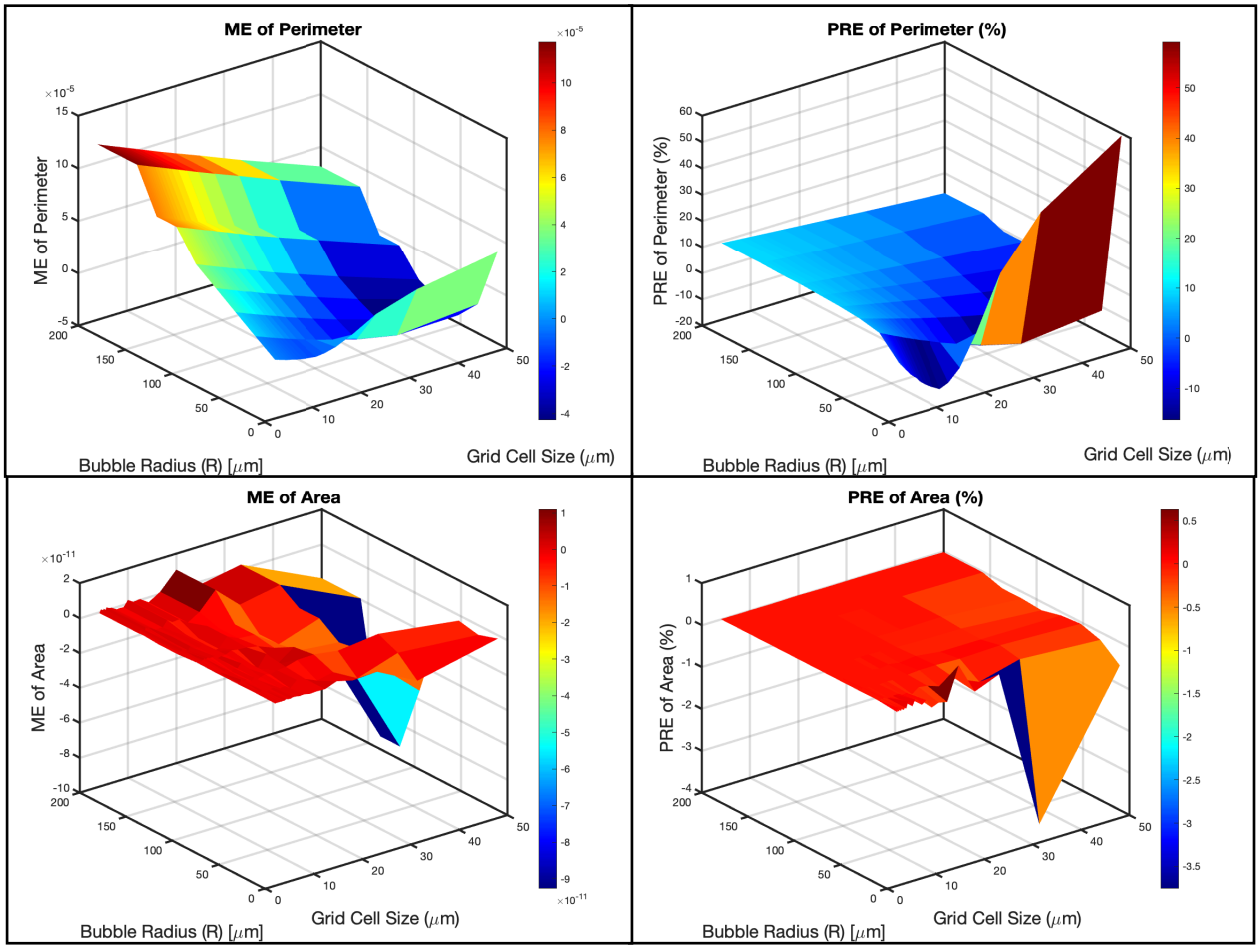

Figure 5.34 Mean Error and Percentage Relative Error of Perimeter and Area Variations with Bubble Radius and Grid cell size

After obtaining the error metrics, the final step is to apply these results to quantify the uncertainties in the experimental HSV data. From the experimental data in Figure 5.32, the calculated dry area fraction and contact line density are 0.48283 and 0.005363 1/μm Using

the resolution size of 12.6 μm obtained from the experiment, we read off the corresponding errors (PRE and ME) in the contact line density (from the perimeter) and dry area fraction (from the area) measurements at the corresponding bubble radii values from **Error! Reference source not found.** and Figure 5.34, respectively. The bubble radii values used to read off these errors are obtained from the experimental data and are sorted in terms of their occurring frequency. This is done so that the most frequent bubbles exert more impact on the uncertainty quantification. The summary of the results obtained is presented in the uncertainty table illustrated in Table 5.6. Thereafter, the weighted average formula expressed in Eq. (5.3) is used to quantify the uncertainty.

$$W = \frac{\sum_{i=1}^{k}(v_i \cdot w_i)}{\sum_{i=1}^{k}(w_i)} \tag{5.3}$$

where v_i is a value from the set (in this case, PRE or ME for contact line density or dry area fraction in Table 5.6), w_i is the weight corresponding to v_i (in this case, the frequency of the radius bin), k is the total number of values.

Table 5.6 Uncertainty Table

S/N	Frequency	Area PRE (%)	Area ME $\times 10^{-12}$	Perimeter PRE (%)	Perimeter ME $\times 10^{-5}$
1	184	-0.5	-1.6	-16.3	-1.0
2	110	0.2	5.6	-1.6	-0.3
3	59	0.03	2.4	2.8	0.9
4	31	0.01	1.8	4.8	2.2
5	11	-0.01	-2.2	5.9	3.5
6	7	0.003	1.6	7.1	6.1
7	3	0.003	1.6	8.0	6.1
8	2	0.006	8.1	8.0	10.1

Therefore, the weighted average values for the PRE and ME for both the area and the perimeter, weighted by frequency, are calculated under erosion and dilation conditions. In the erosion condition, the bubble's boundary is eroded by 1 pixel on all sides. Figure 5.*35*

pictorially explains the difference between erosion and dilation on the bubble's boundary. The uncertainty results are presented in Table 5.7.

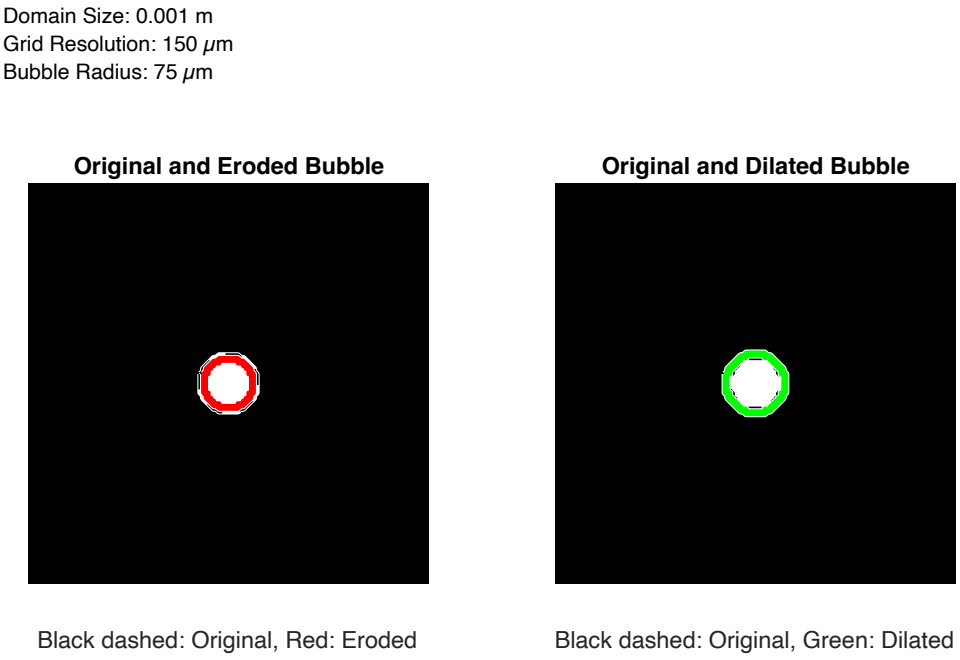

Figure 5.35 Difference Between Erosion and Dilation

Table 5.7 Effects of Dilation on the Uncertainty Quantification

Case Type	Weighted Avg PRE Area (%)	Weighted Avg PRE Perimeter (%)	Weighted Avg ME Area (μm²)	Weighted Avg ME Perimeter (μm)
Erosion	-0.4	13.8	-1.2e-12	1.2e-4
Dilation	-0.4	6.6	-1.2e-12	7.1e-5

The comparative analysis of uncertainties under erosion and dilation conditions, as presented in Table 5.2, provides valuable insights into the differential effects of these two techniques on uncertainty quantification in dry area and contact line measurements. The results indicate that while the weighted average PRE in area remains constant between erosion and dilation, there is a noticeable reduction in the PRE for perimeter and ME for perimeter when

dilation is applied instead of erosion. A possible explanation for these observations is that dilation tends to smooth out the object boundaries, thus reducing edge features that can lead to perimeter overestimation in erosion. This smoothing effect helps in maintaining a closer representation of the original boundary, which is crucial for accurate perimeter estimation. The reduced PRE perimeter in dilation suggests a more accurate capture of boundary lines without the loss of critical boundary details that often occurs in erosion due to pixel removal.

Subsequently, the same analysis have been extended to other use cases encompassing fluids and operating conditions for liquid nitrogen, argon, FC-72 and high pressure water and the results of this analysis are summarized in Table 5.8.

Table 5.8 Uncertainty Quantification for Each Fluid

Fluid	**Weighted Avg PRE Area (%)**	**Weighted Avg PRE Perimeter (%)**	**Weighted Avg ME Area (μm²)**	**Weighted Avg ME Perimeter (μm)**
FC72	-0.05	-6.8	-5.7e-13	2.5e-06
LAr	-0.05	-6.5	-4.8e-13	1.2e-06
LN2	-0.06	-8.4	-3.2e-13	-2.4e-06
Water	-0.03	-1.0	-1.1e-12	1.9e-05

Table 5.8 presents the uncertainty quantification for various fluids (FC72, LAr, LN2, and Water) in terms of weighted average values for PRE (Percentage Relative Error) area percentage, perimeter percentage, area in μm², and perimeter in μm. For the PRE area percentage, the values range from -0.03% for Water to -0.06% for LN2. These negative values indicate that the measured areas are slightly smaller than the true values. The PRE perimeter percentage shows a larger range, from -1% for Water to -8.4% for LN2, suggesting that the perimeter measurements have higher uncertainty compared to the area measurements. The weighted average ME (Mean Error) for area in μm² ranges from -1.1e-12 for Water to -5.7e-13 for FC72. These values represent the absolute errors in the area measurements and are relatively small, indicating that the area measurements are precise. Similarly, the weighted average ME for perimeter in μm ranges from 1.9e-05 for Water to -2.4e-06 for LN2, showing

that the absolute errors in perimeter measurements are also small. It is further observed that the PRE perimeter percentage values are significantly larger than the PRE area percentage values for all fluids. This suggests that the perimeter measurements have higher relative uncertainty compared to the area measurements. This could be because perimeter measurements are more sensitive to the resolution and accuracy of the measurement technique.

When comparing the uncertainties across different fluids, LN2 appears to have the highest PRE perimeter percentage at -8.4%, while Water has the lowest at -1 %. This indicates that the perimeter measurements for LN2 have the highest relative uncertainty among the fluids studied. The PRE area percentage values are more consistent across the fluids, with LN2 having the highest uncertainty at -0.06% and Water having the lowest at -0.03%.

These uncertainties in fluid property measurements can have implications for the accuracy of heat flux reconstruction methods that rely on these properties. The propagation of these uncertainties through the heat flux calculation process should be carefully evaluated to understand their impact on the results. Additionally, the relative importance of these uncertainties can be related to sources of uncertainty, such as those arising from the segmentation process. It is noticed that the pixelization errors are comparable to the segmentation errors. For instance, for FC-72, the mean segmentation error is about 6.5% which approximately agrees with the 6.8% from the pixelization uncertainty quantification. These can be identified as the most critical factors affecting the overall accuracy of the heat flux reconstruction.

Chapter 6

Conclusions

In this thesis, we have successfully developed and applied a robust methodology for segmenting and analyzing high-speed video (HSV) data of boiling phenomena using U-Net Convolutional Neural Networks (CNNs). Under different experimental conditions, the proposed approach has been validated across various fluids, including liquid nitrogen, argon, FC-72, and high-pressure water.

The comparative analysis of the U-Net CNN segmentation and adaptive thresholding techniques has demonstrated the superior performance of the U-Net model in accurately identifying and delineating bubbles, particularly in challenging scenarios involving smaller bubbles and complex bubble topologies. The U-Net model has shown consistently high accuracy, precision, and recall across different fluids and heat flux conditions.

Furthermore, we have conducted a comprehensive uncertainty quantification analysis to assess the impact of discretization errors arising from the pixelation of bubbles on the calculated boiling metrics, such as contact line density and dry area fraction. The weighted average PREs and MEs for these metrics have been determined under both erosion and dilation conditions, providing valuable insights into the robustness and reliability of the measurements.

The uncertainty analysis has revealed that the contact line density measurements exhibit higher relative uncertainty compared to the dry area fraction measurements across all fluids studied. Additionally, the comparative analysis of uncertainties under erosion and dilation conditions has highlighted the potential benefits of using dilation techniques to reduce perimeter overestimation and maintain accurate boundary representation.

Overall, the proposed U-Net CNN-based segmentation approach, coupled with the comprehensive uncertainty quantification analysis, provides a powerful tool for the accurate and reliable characterization of boiling phenomena from HSV data. This methodology can

significantly contribute to the advancement of boiling heat transfer research and the development of improved heat transfer models and correlations.

Recommendations for Future Work:

1. Address the limitations of CNNs in generalizing to other HSV data: The current study has highlighted the need for creating specialized U-Net models for different fluids and operating conditions due to the limited generalizability of the trained models. To overcome this limitation and enable autonomous experimentation, future research should focus on developing more sophisticated image segmentation models, such as foundation models, that are less sensitive to domain shifts. These models should be capable of adapting to new HSV datasets with minimal fine-tuning, thus reducing the need for specialized models for each fluid and operating condition.
2. Investigate advanced uncertainty quantification techniques: While the current study has focused on the impact of discretization errors, it has only addressed isolated bubbles scenarios. Future work could explore more advanced uncertainty quantification techniques, such as Monte Carlo simulations or Bayesian inference, to provide a more comprehensive assessment of the uncertainties associated with the boiling metrics and their propagation through the heat flux reconstruction process.
3. Develop real-time segmentation and analysis: To enable the real-time monitoring and control of boiling processes, it would be beneficial to develop efficient algorithms for real-time segmentation and analysis of HSV data using the trained image segmentation models. This could involve optimizing the model architecture, implementing parallel processing techniques, and integrating the segmentation pipeline with data acquisition systems.
4. Investigate the impact of uncertainties on heat flux reconstruction: Future studies could focus on evaluating the propagation of uncertainties in fluid property measurements through the heat flux reconstruction process. This would provide valuable insights into the sensitivity of heat flux calculations to various sources of uncertainty and help identify the most critical factors affecting the overall accuracy of the reconstruction.
5. Extend the methodology to other multiphase flow phenomena: The proposed image segmentation approach could be adapted and applied to other multiphase flow

phenomena, such as droplet formation, spray characterization, or bubble dynamics in microchannels. This would broaden the applicability of the methodology and contribute to the advancement of multiphase flow research in various fields.

By addressing these recommendations, future research can build upon the findings of this thesis and further enhance the understanding, characterization, and modeling of boiling phenomena using advanced image segmentation and uncertainty quantification techniques. The development of more generalizable and robust image segmentation models, such as foundation models, will be crucial in enabling autonomous experimentation and reducing the need for specialized models for each fluid and operating condition.

Code Availability

The codes used in this thesis as well as tutorials are available at this repository link: https://github.com/chikap421/cvboil

Bibliography

[1] A. Richenderfer, A. Kossolapov, J.H. Seong, G. Saccone, E. Demarly, R. Kommajosyula, E. Baglietto, J. Buongiorno, M. Bucci, Investigation of subcooled flow boiling and CHF using high-resolution diagnostics, Exp. Therm. Fluid Sci. 99 (2018) 35–58. https://doi.org/10.1016/j.expthermflusci.2018.07.017.

[2] C. Wang, G. Su, O. Akinsulire, L. Zhang, M.M. Rahman, M. Bucci, Investigation of critical heat flux enhancement on nanoengineered surfaces in pressurized subcooled flow boiling using infrared thermometry, Heat Transf. Eng. 45 (2024) 417–432. https://doi.org/10.1080/01457632.2023.2191441.

[3] M. Bucci, A. Richenderfer, G.-Y. Su, T. McKrell, J. Buongiorno, A mechanistic IR calibration technique for boiling heat transfer investigations, Int. J. Multiph. Flow 83 (2016) 115–127. https://doi.org/10.1016/j.ijmultiphaseflow.2016.03.007.

[4] C.(王驰) Wang, M.M. Rahman, M. Bucci, Decrypting the mechanisms of wicking and evaporation heat transfer on micro-pillars during the pool boiling of water using high-resolution infrared thermometry, Phys. Fluids 35 (2023) 037112. https://doi.org/10.1063/5.0135110.

[5] A. Kossolapov, B. Phillips, M. Bucci, Can LED lights replace lasers for detailed investigations of boiling phenomena?, Int. J. Multiph. Flow 135 (2021) 103522. https://doi.org/10.1016/j.ijmultiphaseflow.2020.103522.
[6] A. Kossolapov, M.T. Hughes, B. Phillips, M. Bucci, Bubble departure and sliding in high-pressure flow boiling of water, (2024). https://doi.org/10.48550/arXiv.2311.12749.
[7] J. Soibam, V. Scheiff, I. Aslanidou, K. Kyprianidis, R. Bel Fdhila, Application of deep learning for segmentation of bubble dynamics in subcooled boiling, Int. J. Multiph. Flow 169 (2023) 104589. https://doi.org/10.1016/j.ijmultiphaseflow.2023.104589.
[8] I. Malakhov, A. Seredkin, A. Chernyavskiy, V. Serdyukov, R. Mullyadzanov, A. Surtaev, Deep learning segmentation to analyze bubble dynamics and heat transfer during boiling at various pressures, Int. J. Multiph. Flow 162 (2023) 104402. https://doi.org/10.1016/j.ijmultiphaseflow.2023.104402.
[9] Z. Wenyin, J. Ningde, L. Xia, N. Zhiqiang, Bubble Image Segmentation of Gas/Liquid Two-Phase Flow Based on Improved Canny Operator, in: 2008 Int. Conf. Comput. Sci. Softw. Eng., 2008: pp. 799–801. https://doi.org/10.1109/CSSE.2008.1396.
[10] C. Paz, M. Conde, J. Porteiro, M. Concheiro, On the Application of Image Processing Methods for Bubble Recognition to the Study of Subcooled Flow Boiling of Water in Rectangular Channels, Sensors 17 (2017) 1448. https://doi.org/10.3390/s17061448.
[11] Y. Jin, K. Shirvan, Study of the film boiling heat transfer and two-phase flow interface behavior using image processing, Int. J. Heat Mass Transf. 177 (2021) 121517. https://doi.org/10.1016/j.ijheatmasstransfer.2021.121517.
[12] H. Zhou, X. Niu, An image processing algorithm for the measurement of multiphase bubbly flow using predictor-corrector method, Int. J. Multiph. Flow 128 (2020) 103277. https://doi.org/10.1016/j.ijmultiphaseflow.2020.103277.
[13] W. Li, J. Li, K. Zhou, H. Zhu, Z. Zhang, J. Du, Visualization of Flow Boiling Experiments on Micro/Nanoscale Structured Surfaces in Microchannel, J. Heat Transf. 143 (2021). https://doi.org/10.1115/1.4049843.
[14] R.F.L. Cerqueira, E.E. Paladino, Development of a deep learning-based image processing technique for bubble pattern recognition and shape reconstruction in dense bubbly flows, Chem. Eng. Sci. 230 (2021) 116163. https://doi.org/10.1016/j.ces.2020.116163.
[15] T. Haas, C. Schubert, M. Eickhoff, H. Pfeifer, BubCNN: Bubble detection using Faster RCNN and shape regression network, Chem. Eng. Sci. 216 (2020) 115467. https://doi.org/10.1016/j.ces.2019.115467.
[16] I. Poletaev, M.P. Tokarev, K.S. Pervunin, Bubble patterns recognition using neural networks: Application to the analysis of a two-phase bubbly jet, Int. J. Multiph. Flow 126 (2020) 103194. https://doi.org/10.1016/j.ijmultiphaseflow.2019.103194.
[17] Y. Kim, H. Park, Deep learning-based automated and universal bubble detection and mask extraction in complex two-phase flows, Sci. Rep. 11 (2021) 8940. https://doi.org/10.1038/s41598-021-88334-0.
[18] J.H. Seong, M. Ravichandran, G. Su, B. Phillips, M. Bucci, Automated bubble analysis of high-speed subcooled flow boiling images using U-net transfer learning and global optical flow, Int. J. Multiph. Flow 159 (2023) 104336. https://doi.org/10.1016/j.ijmultiphaseflow.2022.104336.

[19] M. Ravichandran, A. Kossolapov, G.M. Aguiar, B. Phillips, M. Bucci, Autonomous and online detection of dry areas on a boiling surface using deep learning and infrared thermometry, Exp. Therm. Fluid Sci. 145 (2023) 110879. https://doi.org/10.1016/j.expthermflusci.2023.110879.
[20] Y. Suh, S. Chang, P. Simadiris, T.B. Inouye, M.J. Hoque, S. Khodakarami, C. Kharangate, N. Miljkovic, Y. Won, VISION-iT: A Framework for Digitizing Bubbles and Droplets, Energy AI 15 (2024) 100309. https://doi.org/10.1016/j.egyai.2023.100309.
[21] B. Chen, M.C. Ekwonu, S. Zhang, Deep learning-assisted segmentation of bubble image shadowgraph, J. Vis. 25 (2022) 1125–1136. https://doi.org/10.1007/s12650-022-00849-4.
[22] M. Ahmed, A. Habib, M.M. Nawal, M.M.H. Saikot, M.A.H. Chowdhury, M.A. Hoque, A.K.M. Asaduzzaman, H. Pálsson, P. Björnsson, Deep learning-based approach to R-134a bubble detection and analysis for geothermal applications, Case Stud. Therm. Eng. 49 (2023) 103377. https://doi.org/10.1016/j.csite.2023.103377.
[23] K. He, G. Gkioxari, P. Dollár, R. Girshick, Mask R-CNN, (2018). https://doi.org/10.48550/arXiv.1703.06870.
[24] T. Falk, D. Mai, R. Bensch, Ö. Çiçek, A. Abdulkadir, Y. Marrakchi, A. Böhm, J. Deubner, Z. Jäckel, K. Seiwald, A. Dovzhenko, O. Tietz, C. Dal Bosco, S. Walsh, D. Saltukoglu, T.L. Tay, M. Prinz, K. Palme, M. Simons, I. Diester, T. Brox, O. Ronneberger, U-Net: deep learning for cell counting, detection, and morphometry, Nat. Methods 16 (2019) 67–70. https://doi.org/10.1038/s41592-018-0261-2.
[25] Digpriya, S. Saini, J. Banerjee, Analysis of interfacial behavior in two-phase flow using image processing, IOP Conf. Ser. Mater. Sci. Eng. 1146 (2021) 012002. https://doi.org/10.1088/1757-899X/1146/1/012002.
[26] O. Ronneberger, P. Fischer, T. Brox, U-Net: Convolutional Networks for Biomedical Image Segmentation, in: N. Navab, J. Hornegger, W.M. Wells, A.F. Frangi (Eds.), Med. Image Comput. Comput.-Assist. Interv. – MICCAI 2015, Springer International Publishing, Cham, 2015: pp. 234–241. https://doi.org/10.1007/978-3-319-24574-4_28.
[27] C. Maduabuchi, chikap421/cvboil, (2024). https://github.com/chikap421/cvboil (accessed May 12, 2024).
[28] A. Kossolapov, F. Chavagnat, R. Nop, N. Dorville, B. Phillips, J. Buongiorno, M. Bucci, The boiling crisis of water under exponentially escalating heat inputs in subcooled flow boiling at atmospheric pressure, Int. J. Heat Mass Transf. 160 (2020) 120137. https://doi.org/10.1016/j.ijheatmasstransfer.2020.120137.
[29] F. Chavagnat, R. Nop, N. Dorville, B. Phillips, M. Bucci, Single-phase heat transfer regimes in forced flow conditions under exponential heat inputs, Int. J. Heat Mass Transf. 174 (2021) 121294. https://doi.org/10.1016/j.ijheatmasstransfer.2021.121294.
[30] L. Zhang, C. Wang, G. Su, A. Kossolapov, G. Matana Aguiar, J.H. Seong, F. Chavagnat, B. Phillips, M.M. Rahman, M. Bucci, A unifying criterion of the boiling crisis, Nat. Commun. 14 (2023) 2321. https://doi.org/10.1038/s41467-023-37899-7.